Parton Dynamics Inferred from High-Mass Drell-Yan Dimuons Induced by 120 GeV p+D Interactions

by

Bryan J. Ramson

A dissertation submitted in partial fulfillment
of the requirements for the degree of
Doctor of Philosophy
(Applied Physics)
in The University of Michigan
2018

Doctoral Committee:

Associate Professor Christine Aidala, Chair
Professor Dante Amidei
Professor Timothy Chupp
Professor Wolfgang Lorenzon
Professor Homer Neal
Associate Professor Thomas Schwarz

Bryan J. Ramson

bjrams@umich.edu

ORCID iD:0000-0002-0925-3405

For all the people, everywhere

TABLE OF CONTENTS

LIST OF FIGURES

Figure

LIST OF TABLES

LIST OF ABBREVIATIONS

AC Accelerator Complex

ADC Analog-to-Digital Converter

BCDMS Bologna-CERN-Dubna-Munich-Saclay

BIM Beam Intensity Monitor

BNL Brookhaven National Laboratory

CERN European Organization for Nuclear Research

CMS Compact Muon Solenoid

DAQ Data Acquisition System

DIS Deep-Inelastic Scattering

DUNE Deep Underground Neutrino Experiment

E615 Fermilab Experiment 615

E772 Fermilab Experiment 772

E866 Fermilab Experiment 866/NuSea

E906 Fermilab Experiment 906/SeaQuest

E1039 Fermilab Experiment 1039/SeaQuest

EMC European Muon Collaboration

EPICS Experimental Physics and Industrial Control System

FF Fragmentation Function

FMag Focusing Magnet

FNAL Fermi National Accelerator Laboratory/Fermilab

FPGA Field Programmable Gate Array

GSR Gottfried Sum Rule

HERA Hadron Electron Ring Accelerator

KMag Analysis Magnet

Linac Linear Accelerator

LHC Large Hadron Collider

LHCb Large Hadron Collider-beauty

LQFA Light Quark Flavor Asymmetry

MI Main Injector

MicroBooNE Large Liquid Argon Detector for Neutrino Physics

MINERvA Main Injector Experiment for $\nu - A$

MINOS Main Injector Neutrino Oscillations Search

MIT Massachusetts Institute of Technology

MWDC Multiwire Drift Chamber

NA10 CERN North Area 10

NA51 CERN North Area 51

NIM Nuclear Instrumentation Module

NMC New Muon Collaboration

NOvA NuMI Off-Axis ν_e Acceptance Experiment

PCDT Proportional Counter Drift Tubes

PDF Parton Distribution Function

PLC Programmable Logic Controller

PMT Photomultiplier Tube

pQCD perturbative Quantum Chromodynamics

QCD Quantum Chromodynamics

QED Quantum Electrodynamics

QIE Charge Integrator and Encoder

RFQ Radiofrequency Quadrupole

SEM Secondary Emissions Monitor

SIDIS Semi-Inclusive Deep-Inelastic Scattering

SLAC SLAC National Accelerator Laboratory

SSA Single-Spin Production Asymmetry

ABSTRACT

Fermilab Experiment 906/SeaQuest (E906/SeaQuest) is the latest in a well established tradition of studying leptoproduction from the annihilation of a quark and anti-quark, known as the Drell-Yan process. The broad goal of E906/SeaQuest is measuring various properties of nucleon structure in order to learn more about quarks and Quantum Chromodynamics (QCD), the mathematical description of the strong force. The present work investigated violations of the Lam-Tung relation between virtual photon polarization and quark and lepton angular momentum. The violation of Lam-Tung can be explained as the signature of quark-nucleon spin-orbit coupling through the use of the Transverse-Momentum-Dependent (TMD) framework, which assumes that the initial transverse momentum of quarks is smaller than the hard scattering scale, but also non-negligible.

An analysis of the angular moments in Drell-Yan collected by E906/SeaQuest was performed with four different configurations in order to estimate the systematic errors attributed to each correction. After correction for background and error propagation, the final extraction of the azimuthal moment excluding contributions from the trigger was $\nu = 0.151 \pm 0.88(stat.) \pm 0.346(syst.)$ at an average transverse momentum of 0.87 ± 0.50 GeV/c and an average dimuon mass of 5.48 ± 0.70 GeV. In the future, the magnitude of the systematic errors on the extraction could potentially be reduced by improving the quality of the trigger efficiency calculation, improving the intensity dependent event reconstruction efficiency, considering the changes in acceptance due to a beam shift relative to the E906/SeaQuest spectrometer, and improving the modeling of background.

CHAPTER I

Introduction

1.1 The Standard Model

Within the context of our current understanding, the universe does little to enforce differences between commonly referenced classes of objects, at least on subatomic scales. For example, at relativistic speeds, the barrier between matter and energy becomes as porous as the ease with which one performs a Lorentz boost and little discernible difference exists in observations of quantum objects when treated as particles with sufficiently resolved spatial dimensions or probability density matter fields [2, 3]. It is clear that additional descriptors are needed in order to usefully describe subatomic interactions between relevant constituents. The concept of "spin" or the intrinsic behavior of objects when involved in any interaction transferring angular momentum, is not the only relevant characteristic at this scale (many more supplementary descriptors of very small and very fast objects will be used) but it is of special importance in describing the interactions discussed in this dissertation. It is also a suitable subject on which to initiate a string of relevant definitions.

Interestingly, the universe is very attentive to how different bosons, particles with integer spin ($\frac{S_z}{\hbar} = 0, \pm1, \pm2, \pm3,...$), are from fermions, particles with half-integer spin ($\frac{S_z}{\hbar} = \pm\frac{1}{2}, \pm\frac{3}{2}, \pm\frac{5}{2},...$). In aggregate, the behavior of ensembles dominated by each type are described by two distinct models, with fermions subject to *Fermi-Dirac*

statistics and bosons observing *Bose-Einstein* statistics [4]. While both speak in the language of wave functions (which are in complete opposition to *Maxwell-Boltzmann* statistics, the model describing classical ensembles), the dividing behavior centers on the treatment of the wave functions under exchange of particles in each ensemble [5]:

$$\begin{aligned} \textit{Bose-Einstein} \qquad & \Psi_\alpha \Psi_\beta - \Psi_\beta \Psi_\alpha = 0, \\ \textit{Fermi-Dirac} \qquad & \Psi_\alpha \Psi_\beta + \Psi_\beta \Psi_\alpha = 0. \end{aligned} \tag{1.1}$$

Coincidentally, the distinction between fermions and bosons suggests a simple framework for understanding the Standard Model. At the current state of the art, "everyday" matter, or the kind observed outside of the quantum and highly relativistic regimes, is understood to be built from three of the twelve elementary fermions: up and down flavoured quarks are bound together in nucleons (protons and neutrons) which in turn capture negatively charged electrons to form atoms. The strong nuclear force mediates interactions among color charged objects using gluons and is responsible for "binding" the quarks to each other in the atomic nucleus. Photons moderate the electromagnetic force, which allows the postively charged nucleus to "capture" negatively charged electrons, determining all of chemistry. Representing two of the fundamental forces of nature, both gluons and photons are bosons, but more importantly all "force carrier" particles are vector or gauge bosons, indicating they all inherently carry a spin of one and relate to some elementary gauge structure which encodes the preservation of some fundamental universal symmetry. A chart neatly arranging all of the fermionic matter fields with the bosonic force fields is shown in Figure 1.1 [6].

Interactions in the Standard Model can be represented by clever algebraic negotiations of quantized free-form matter fields intended to preserve universal gauge symmetries as much as physically possible. The entire chart in Figure 1.1 can be restated in one highly condensed equation describing three of the four fundamental

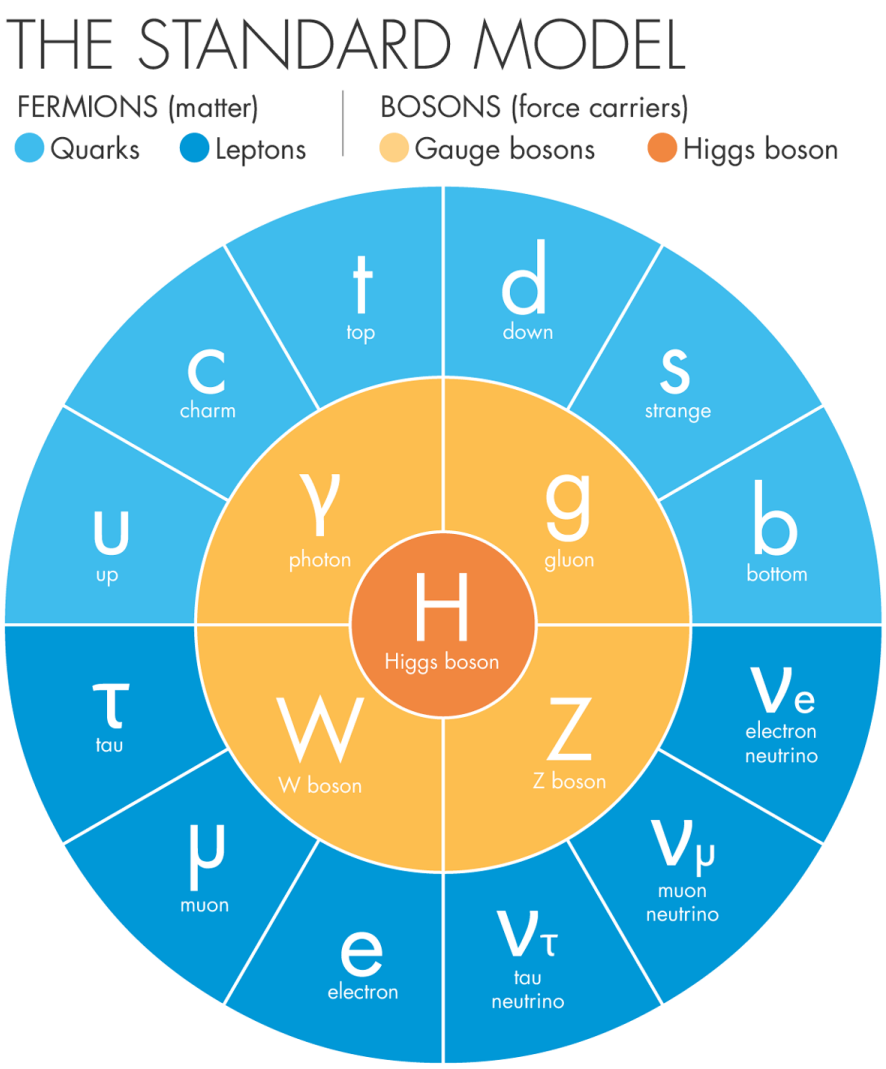

Figure 1.1: **The Standard Model.** The two inner circles index all currently known bosons in the standard model. The innermost circle is the scalar boson, which indicates the existence of a field that grants mass to all other elementary particles (except for neutrinos). The Higgs/scalar boson arises from the symmetry breaking of electroweak theory and does not communicate a fundamental force. The innermost ring details the four bosons of the three unified forces, half of which are massive (Z^0 and $W^{\pm}$) and the other half (γ and g) are not. The outermost circle describes all fermion matter fields, with the top half consisting of the three generations of quarks and the bottom half, the three generations of leptons. This beautiful diagram was borrowed from Lucy Reading-Ikkanda in Natalie Wolchover's article for Quanta Magazine.

forces (gravity has not yet been integrated into the standard model) and the mechanism by which elementary particles gain rest mass:

$$\mathcal{L}_{SM} = -\frac{1}{4}E^{\alpha}_{\mu\nu}E^{\alpha\mu\nu} + \bar{\psi}i\not{D}\psi + (D_\mu\phi)^\dagger(D^\mu\phi) - \lambda(\phi^\dagger\phi - \frac{1}{2}\nu^2) - \phi^\dagger\bar{\psi}_i Y_{ij}\psi_j + h.c., \quad (1.2)$$

where many sums and indices have been omitted for brevity [7, 8, 9, 10].

The first term is a field kinetic energy sum for all three bosonic force fields. Taken together, the three fields represent the underlying $\mathrm{SU}(3)_C \times \mathrm{SU}(2)_L \times \mathrm{U}(1)_Y$ group structure of the Yang-Mills (non-abelian gauge) theory. The generic field strength tensor $E^{\alpha}_{\mu\nu}$ is a sum of the derivatives of the four-potentials for each generic quantized gauge potential field:

$$\begin{gathered} E^{\alpha}_{\mu\nu} = \frac{1}{g}[D_\mu, D_\nu] = \partial_\mu A^{\alpha}_{\nu} - \partial_\nu A^{\alpha}_{\mu} \pm ig[A^{\alpha}_{\mu}, A^{\alpha}_{\nu}], \\ D_\mu = \partial_\mu + igC^{\alpha}A^{\alpha}_{\mu}, \end{gathered} \quad (1.3)$$

where quantization of the gauge potential field is implied by the commutation relation but can be explicitly represented by considering the Feynman path-integral of the generic classical action for the field and corresponding Noether current [11, 12, 13]:

$$\begin{aligned} S &= \int [E^{\alpha\mu\nu}E^{\alpha}_{\mu\nu} + J^{\alpha}A^{\alpha}_{\mu}]d^4x, \\ Z &= \int dE e^{iS(E)}, \end{aligned} \quad (1.4)$$

In the above equations, the structure of the commutator (which can also be absorbed into the covariant derivative as an explicit coefficient, C^{α}) depends on the underlying *local* gauge structure of the field in question. In the full expansion of the standard model Lagrangian, the generic field strength tensor $E^{\alpha}_{\mu\nu}$ is replaced by $G^{\alpha}_{\mu\nu}$ for the massless gluons which serve as non-abelian generators for Quantum Chromodynamics (QCD), the mathematical representative of the strong nuclear force. The fields

denoted by $W^{\beta}_{\mu\nu}$ are the massive $W^{\pm}$ and Z^0 bosons which act as the non-abelian generators for weak isospin, mediate flavor interactions and represent the weak nuclear force. The massless B-boson is represented by $B_{\mu\nu}$ and acts as the abelian generator of weak hypercharge. Under electroweak symmetry breaking, the weak isospin generators mix with the weak hypercharge generators to form photons, the boson mediating Quantum Electrodynamic (QED) interactions.

The second term is the kinetic energy contributed from a sum of all fermionic matter fields, where ψ is every possible flavor of quark in every generation (up, down, charm, strange, top [truth], and bottom [beauty]) and every possible lepton and neutrino in every generation (electron, electron-neutrino, muon, muon-neutrino, tau, and tau-neutrino). The *local* gauge symmetry of the fields is maintained while interacting through a covariant derivative:

$$\not{D} = \gamma^{\mu} D_{\mu} = \gamma^{\mu}[\partial_{\mu} + ig_3 C^{\alpha} A^{\alpha}_{\mu} + ig_2 c^{\beta} W^{\beta}_{\mu} + ig_1 Y_i B_{\mu}], \tag{1.5}$$

where γ^{μ} are the gamma matrices, $g_{1,2,3}$ are the electroweak and strong coupling constants; and Y_i, c^{α}, and C^{α} are the electroweak and strong gauge structure group generators. The remaining explicit terms detail the kinetic energy from the scalar/Higgs field, the scale of electroweak symmetry breaking, and the scalar field interactions with fermions as well as the appropriate massive Yukawa (scalar field to fermion field) couplings.

1.2 Quantum Chromodynamics

The standard model precisely defines the interactions of all three unified fundamental gauge symmetries, but without electroweak symmetry breaking, fails to explain the mass of the $W^{\pm}$ and Z^0 bosons. With symmetry breaking, the underlying group structure of the gauge theory changes significantly, $SU(3)_C \times SU(2)_L \times U(1)_Y \rightarrow$

$SU(3)_C \times U(1)_{em}$ leaving only massless photons and gluons. Comparing and contrasting how these two forces interact with matter is an excellent way to illustrate the idiosyncrasies of QCD and the particulars of nuclear physics.

The QED and QCD Lagrangians resemble each other, indicating that they can be considered together:

$$\begin{aligned}
\mathcal{L}_{QED} =& \bar{\psi}_e(i\not{D} - m_e)\psi_e - \frac{1}{4}F_{\mu\nu}F^{\mu\nu}, \qquad \not{D} = \gamma^\mu D_\mu = \gamma^\mu(\partial_\mu - i\alpha_e A_\mu), \\
\mathcal{L}_{QCD} =& \sum_q \bar{\psi}_q(i\not{D} - m_q)\psi_q - \frac{1}{4}G^\alpha_{\mu\nu}G^{\alpha\mu\nu}, \qquad \not{D} = \gamma^\mu D_\mu = \gamma^\mu(\partial_\mu - i\alpha_s T^\alpha A^\alpha_\mu)
\end{aligned} \tag{1.6}$$

but the underlying group structure gives the two fields highly disparate behavior. The major differences start with the sheer number of generators or possible field sources but quickly move into important distinctions affecting the fundamental structure of each group. The unitary group of order one, U(1), also known as the "trivial" group, has one generator which can be represented as a one dimensional complex matrix, $\theta(x)$, or a complex phase shift of the wave function in space and time, $e^{i\hat{N}\theta} = \hat{N}[\cos(\theta) + i\sin(\theta)]$, where $\hat{N}$ is the number operator for an ensemble of electrons (i.e. cumulative charge). The U(1) group is also abelian, meaning successive gauge transformations in this group are commutative. In contrast, the non-abelian special unitary group of order three, SU(3), has eight linearly independent generators for the eight possible gluon color charge flows. These generators act on a conserved charge-like basis vector in three colors: red, green, and blue:

$$r = \begin{pmatrix} 1 \\ 0 \\ 0 \end{pmatrix}; \qquad g = \begin{pmatrix} 0 \\ 1 \\ 0 \end{pmatrix}; \qquad b = \begin{pmatrix} 0 \\ 0 \\ 1 \end{pmatrix}. \tag{1.7}$$

The QCD gauge transformation is applied to a wave function as a phase vector and

is of the form $e^{ig\theta^\alpha C^\alpha}$ where $\theta^\alpha = \theta^\alpha(x)$ is the vector detailing the magnitude of color flow and C^α are the Gell-Mann matrices, which are 3×3 representations of the SU(3) group structure [14].

The differences in fundamental structure significantly affect how the two forces interact with matter. The strong force can be represented as a $SU(2) \times U(1)$ global symmetry with physical color charge modeled as a two dimensional vector in color isospin and hypercharge space as shown in Figure 1.2 [15]. When single quark and

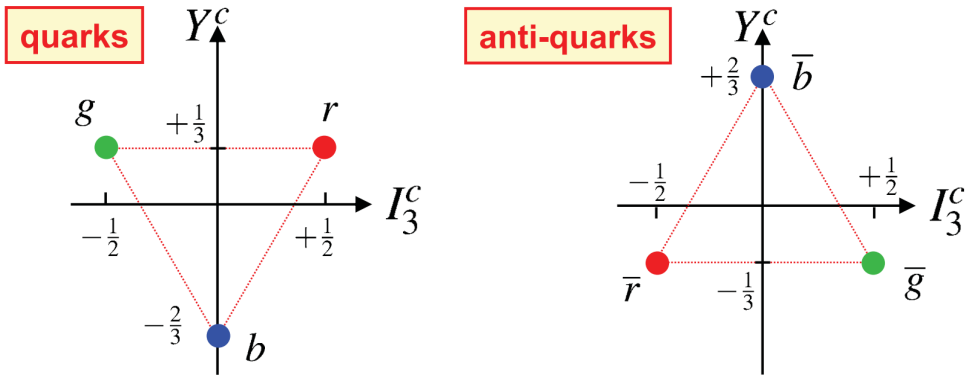

Figure 1.2: **Visual representation of color isospin and hypercharge space.** Both graphs have color hypercharge on the y-axis and the magnitude of the color isospin vector on the x-axis. The graph on the left is the possible color charge for single quarks and the graph on the right is the possible color charge for anti-quarks. Each diagram is an element in $SU(3)$ space.

single anti-quark wave functions are combined, as in mesons, many possible color states exist (as shown in Figure 1.2) but only the singlet state, $\psi^{q\bar{q}} = \frac{1}{\sqrt{3}}(r\bar{r} + g\bar{g} + b\bar{b})$ maintains symmetry under rotations in color space. This same argument applies to combinations of three single quarks, with the singlet state defined as: $\psi^{qqq} = \frac{1}{\sqrt{6}}(rgb - rbg + gbr - grb + brg - bgr)$ for baryons. Recently, predicted tetraquark mesons ($\psi^{q\bar{q}q\bar{q}}$) and pentaquark baryon ($\psi^{qqqq\bar{q}}$) bound states have been observed at the European Organization for Nuclear Research (CERN)[1] Large Hadron Collider-

[1]The European laboratory was originally named the Conseil Européen pour la Recherche Nucléaire (CERN) after the council which established the organization. That name was changed to the Organisation Européenne pour la Recherche Nucléaire after the laboratory was built. https://home.cern/about

'beauty' (LHCb) experiment [16, 17, 18, 19]. From these arguments *confinement* has a precise definition for matter:

Confinement: Only color singlet states exist as free particles in nature.

The necessity of color singlets in nature is further emphasized by the behavior of the gluons. Due to the abelian structure of the U(1) group, the photon has no self charge, does not self-interact, and its unitary structure grants QED an infinite range with limited field strength. The relatively simple behavior is reflected in the

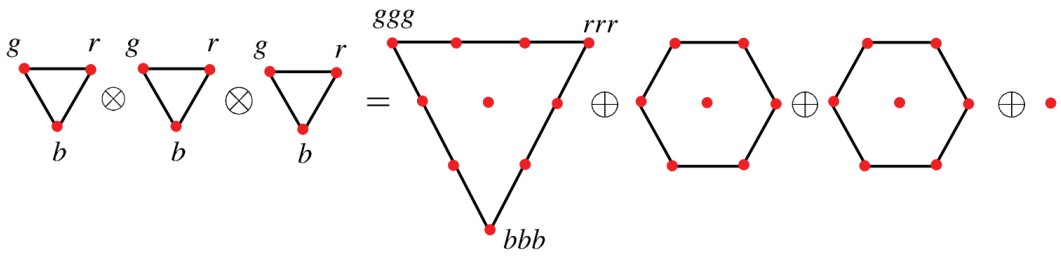

Figure 1.3: **Visual representation of 3 quark bound states in color isospin and hypercharge space.** Each graph has its own individual color isospin and hypercharge axes. On the left side of the equation are three quarks each with an element from SU(3). On the right are possible color configurations, with the rightmost graph representing the antisymmetric quark singlet. All graphs have color hypercharge on the y-axis and the magnitude of the color isospin vector on the x-axis. This represents the equation $3 \otimes 3 \otimes 3 = 10 \oplus 8 \oplus 8 \oplus 1$.

electromagnetic coupling constant, $\alpha_e = \frac{e^2}{4\pi\hbar c} \approx \frac{1}{137}$, which slowly varies with scale due to charge screening or the tendency for field sources to polarize the vacuum in such a way that virtual particles act as a weakening dielectric medium for probes [20]. The non-abelianess of the SU(3) group implies that the gluons have self-charge, allowing gluon self-interaction, and supporting an almost constant field strength over a limited range of $\sim 10^{-15}$ meters. This phenomenon is expressed in the coupling constant of the nuclear strong force, $\alpha_s = \left(\frac{g_s}{4\pi}\right)^2 \approx 1$ at low energies which indicates the presence of color anti-screening [21]. In further contrast to photons, gluon charge

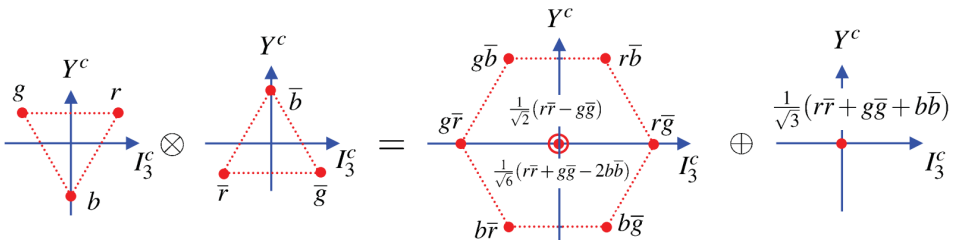

Figure 1.4: **Visual representation of $q\bar{q}$ pair or elementary g currents in color isospin and hypercharge space.** Each graph has its own individual color isospin and hypercharge axes. On the left side of the equation are a quark and anti-quark or a single gluon with a combined color and anti-color charge. The right side of the equation are the allowed color combinations according to the SU(3) group. For mesons the only allowed state is the antisymmetric singlet which implies mesons are always in a superposition of color and no color octets exist in nature. No free gluons exist precluding the existence of an anti-symmetric superposition of states for a single gluon, but the eight possible gluon charges are represented in the octet. This is a visible representation of the equation: $3 \otimes \bar{3} = 8 \oplus 1$.

must contain both color and anti-color, and the component of the wave function which concerns color has the exact same structure as mesons, but because color flows are allowed in the nuclear medium, the singlet state, which is necessary for mesons to exist in nature, is forbidden in the linearly independent generators of the group defining SU(3). If the strong nuclear force preserved a U(3) symmetry over rotations in color space an additional matrix with nonzero trace would be added to the group of Gell-Mann matrices, and this extra matrix would represent the gluon singlet, allowing colorless long range interactions.

1.3 High-Energy Nuclear Physics and Perturbative QCD

Overcoming confinement to observe nucleon structure is one of the defining features of the field of high energy nuclear physics. Another of its defining features was the complementarity of experiment and theory in working towards the development of the field, as theoretical techniques were developed specifically to interpret

experiment. Modern nuclear physics of the style that would eventually split into high energy particle physics and high energy nuclear physics, began with the electron-proton deep-inelastic scattering (DIS) experiments performed at the SLAC National Accelerator Laboratory (SLAC[2]) in collaboration with the Massachusetts Institute of Technology (MIT). For their participation in the SLAC-MIT DIS experiments, Jerome Friedman, Henry Kendall, and Richard Taylor shared the 1990 Nobel prize in physics [22, 23, 24]. Direct motivation for the SLAC-MIT DIS experiments came about from the relatively recent discovery of QED and its predictions concerning nucleon structure, which when combined with then current measurements of elastic scattering off of nuclei, suggested distributed electric charge in the nucleus [25, 26]. A Feynman diagram of DIS is shown in Figure 1.5.

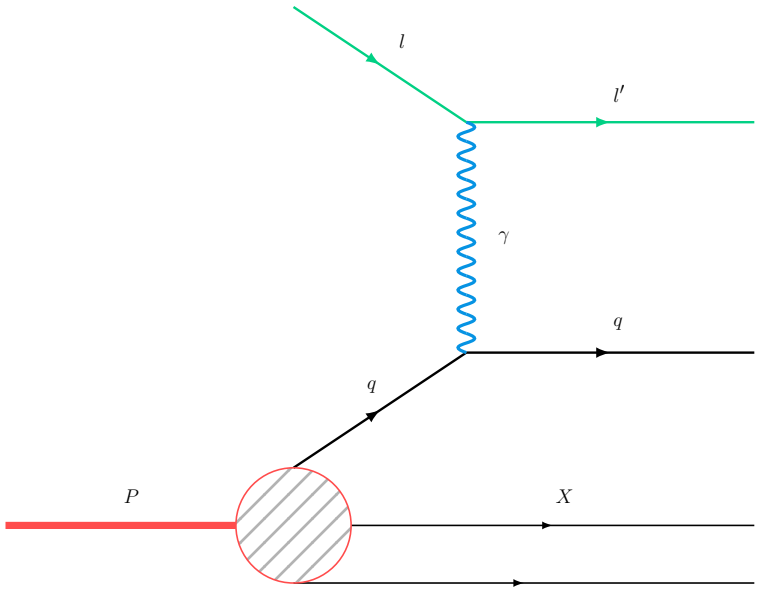

Figure 1.5: **Feynman diagram describing lepton-nucleon Deep Inelastic Scattering.** All lines are Fourier transforms of world lines. Straight lines with arrows represent the momenta of elementary particles, the arrowless line is the momentum of the composite nucleon, and wavy lines represent the momentum of force carrier bosons. In this process, a lepton emits a photon which strikes a quark from a nucleon. In this case the inelastic scattering breaks apart the composite object.

[2]Originally called the Stanford Linear Accelerator Center (SLAC), the name was changed to the SLAC National Accelerator Center in 2008.

Before SLAC, cosmic ray observations of subatomic decay particles had given way to accelerator experiments, like the 22 MeV betatron at Illinois in the fifties and Brookhaven National Laboratory's (BNL) Alternating Gradient Synchrotron (AGS) in the early and mid sixties. Many accelerated based experiments produced new observations of elementary particles and hinted at deeper underlying elementary structures [27, 28, 29, 22, 30]. Specifically, the observation of new mesons and baryons (which were supposed to be 'elementary' particles) rendered obsolete older models like Heisenberg's SU(2) isospin interpretation of nucleons [31]. In response, Murray Gell-Mann and George Zweig independently proposed a broken SU(3) dependent light quark (or 'ace' as proposed by Zweig) flavor symmetry, dubbed the 'eight-fold way' by Gell-Mann (and as distinctly 'not the eight-fold way' by Zweig) to provide some framework in which to understand the underlying structure of hadrons [14, 16, 32]. This framework provided an explanation of hadron mass hierarchies that seemed plausible at the time (despite its incorrectness with regard to the standard model) and ultimately introduced the idea that 'strangeness', and by extension, quark flavor, played a fundamental role in 'static' hadronic structure.

The crude introduction of quark flavor solved one problem by introducing another: some baryons, like protons and neutrons had quarks which were assumed to have an intrinsic spin of $\frac{1}{2}$ but in order for baryons to obey the Pauli exclusion principle, some other degree of freedom must also be present. Gell-Mann and Zweig attempted to solve the problem by fitting static structure to higher order group structures, but initial electron-proton DIS data from SLAC provided the answer. After a precursory look at DIS data, Richard Feynman introduced the idea of "partons" to explain the change in constituent nucleon particles in scattering experiments and James Bjorken along with Emmanuel Paschos formulated a treatment of the dynamics using sum rules and the asymptotic limit or "infinite momentum transfer" frame [33, 34, 35, 36]. Both the quark and parton interpretations were necessary to finalize QCD as a

description of the strong force, but the characteristic scaling of DIS indicated hadronic dynamics were significantly more difficult to intepret. The DIS cross section is:

$$\frac{d\sigma}{dE'd\Omega} = \frac{\alpha_s^2}{4E^2 \sin^4 \frac{\theta}{2}} \left[W_2(\nu, q^2) \cos^2 \frac{\theta}{2} + 2W_1(\nu, q^2) \sin^2 \frac{\theta}{2} \right], \tag{1.8}$$

where α_s is the strong coupling constant, E and E' are the initial and final electron energies, θ is the angle from initial electron direction in the laboratory frame, W_1 and W_2 are hadronic amplitudes introduced by the square of the hadronic and leptonic tensors , $\nu = \frac{p \cdot q}{M}$ (where M is the mass of the proton), and q^2 is the invariant energy transfer of the exchanged photon squared [36]. Scaling with respect to q^2 is a crude indication that as the resolving power of the photon increases, partons behave less like objects with distributed charge and more like point particles. This property defined the creation of nucleon structure functions which above a certain q^2 were only dependent on the dimensionless Bjorken scaling variable, $x = \frac{q^2}{2M\nu}$ [20]:

$$\begin{aligned} MW_1(\nu, q^2) \rightarrow & F_1(x) = \frac{1}{2x} F_2(x), \\ \nu W_2(\nu, q^2) \rightarrow & F_2(x) = \sum_i e_i^2 x f_i(x). \end{aligned} \tag{1.9}$$

Here, e_i^2 is the electric charge of i$^{\text{th}}$ flavored quark and $f_i(x)$ are the unitless flavor indexed *parton distribution functions* (PDFs). It should be noted that the Bjorken scaling variable, x, can be interpreted as the parton momentum fraction in the $q^2 \rightarrow \infty$ or infinite momentum transfer frame [37]. While Bjorken predicted the existence of the fourth "charm" quark before its discovery (due to an erroneous SU(4) global symmetry), the infininte momentum transfer frame, which has since been incorporated in more recent formal descriptions of the light front frame, was not the missing link for uniting the parton and quark pictures [38]. However, the treatment of the parton scattering problem enabled by the infinite momentum transfer frame was critical for understanding the particulars of parton dynamics and officially suggested that any

theory dealing with the strong force and nuclear physics would need to grapple with the appearance of point-like particles in an otherwise diffuse structure.

In 1973, David Politzer, independently from David Gross and Franck Wilczek who worked as a pair, met that challenge by simultaneously introducing an SU(3) "color" dependent gauge theory and the idea of *aymptotic freedom* for which they all were awarded a Nobel Prize in 2004 [39, 40].

> **Asymptotic Freedom**: For certain non-Abelian gauge theories the energy scale of interaction is inversely related to interaction strength.

Asymptotic freedom allowed for the perturbative modeling of strong nuclear interactions through empirical parameterization of confinement above a certain energy scale in experimental calculations. This process, known as factorization, forms the basis of perturbative QCD (pQCD) and effectively partitions strong interactions at high energies into two distinct parts: one perturbatively calculated "hard" interaction which occurs over a short time interval and length scale and an empirically measured "soft" contribution occurring over a long time interval and length scale [41]. The energy scale above which pQCD is valid is referred to as Λ_{QCD} and acts as an infrared cutoff in the equation:

$$\alpha_s(q^2) = \left(\frac{g(q^2)}{4\pi}\right)^2 \approx \frac{1}{\beta \ln \frac{q^2}{\Lambda^2_{QCD}}}, \tag{1.10}$$

with $\Lambda^2_{QCD} \approx 213MeV$ and $\beta \approx \frac{9\alpha^2}{2\pi}$ [41, 42, 43]. The ideas of confinement and asymptotic freedom with relation to the running of the coupling constant for both QED and QCD are shown in Figure 1.6 [44].

In interpretating the parton picture used to describe DIS at SLAC, Bjorken had already created mathematical objects which were suitable for description of the long-term initial state: PDFs. Factorization implied the *universality* of PDFs, elevating them from mere descriptions of scattering between electrons and protons, to empirical, process-independent descriptions of nucleon structure with a precise theoretical

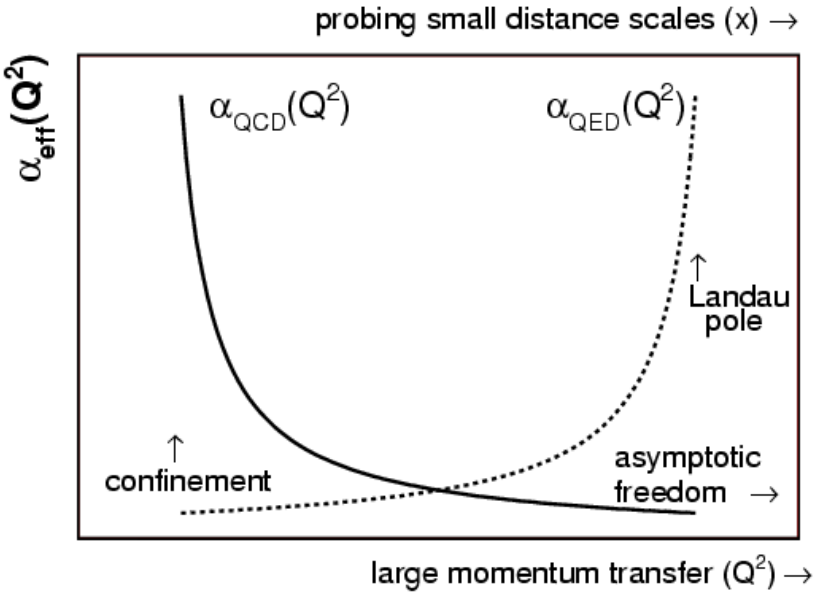

Figure 1.6: **Confinement, Asymptotic Freedom, and the running coupling constant for QCD compared to QED.** On the x-axis is increasing momentum transfer, q^2 and on the y-axis is the effective "strength" of coupling for the field theory. At low momentum transfers (and large length scales) QCD enters the region of confinement which is characterized by color singlets and bound states while QED is relatively weakly interacting. As momentum transfer in an interaction increases (and length scales decrease) $\alpha_s \to 0$ but QED approaches a Landau pole or a region of "infinite" coupling.

definition. The simplest schematic description of the factorization theorem for DIS is:

$$\begin{aligned} \sigma^{lN \to lX} &= f(x) \otimes \hat{\sigma} \\ \frac{d\sigma^{lN \to lX}}{dq^2 dx dy} &= \sum_i f_{i/N}(x) \frac{d\hat{\sigma}}{dq^2 dy}, \end{aligned} \tag{1.11}$$

where y is the rapidity of the process, N is the nucleon of the constituent quark, and $\hat{\sigma}$ is the perturbatively calculated hard scattering component. After the most recent round of formalization incorporating the most important aspects of the infinite

momentum frame into the light front frame, a quark PDF can be formally defined as:

$$f_{j/N}(x) = \int \frac{d\chi}{2\pi} e^{-ixn\cdot P\chi} \langle P_N|\bar{\psi}_j(\chi n)\frac{n\cdot\gamma}{2}\psi_j(0)|P_N\rangle\,, \tag{1.12}$$

where $f_{j/N}(x)$ is the initial state number density of parton "j" in nucleon "N" normalized to unity, $\int_0^1 f_i(x)dx = 1$, χ is a dummy momentum fraction integration variable, n a future pointing, light-like vector $n^\mu = (n^+, n^-, n_\perp) = (0, 1, 0, 0)$, P_N is the momentum of the nucleon, with $|P_N\rangle$ representing the state of the nucleon with momentum P_N, and γ is one of the gamma matrices [41]. In terms of actual experimental calculations, equations 1.8 and 1.9 can be combined using the factorization theorem to produce:

$$\frac{d\sigma}{dq^2dxdy} = \sum_i e_i^2 f_{i/N}(x)\frac{8\pi\alpha^2}{q^{\frac{5}{2}}} sx\Big[1 + (1-y)^2\Big], \tag{1.13}$$

where s is the s-channel Mandelstam variable ($s = (p_1 + p_2)^2$).

It was only after DIS was well understood as a way to probe nucleon structure through factorized treatment of the strong nuclear force that the quark picture and parton picture united. Now, the two terms are virtually interchangeable (colloquially true but both terms have different denotations) and DIS comprises the lionshare of nucleon structure measurements, most recently culminating with the final HERA extractions of PDFs from the H1 and Zeus experiments (shown in Figure 1.7) [45]. More sophisticated semi-inclusive treatments of DIS (SIDIS) where a produced hadron is measured as well as the interacting electron have used factorization to characterize the behavior of partons as they recombine into color neutral singlets outside of the nucleon in a process called hadronization:

$$\begin{aligned} \sigma^{lN\to lhX} &= f(x)\otimes\hat{\sigma}\otimes D(z), \\ \frac{d\sigma^{lN\to lhX}}{dq^2dxdydz} &= \sum_{i,j} f_{i/N}(x)\frac{d\hat{\sigma}}{dq^2dy}D_{h/j}(z), \end{aligned} \tag{1.14}$$

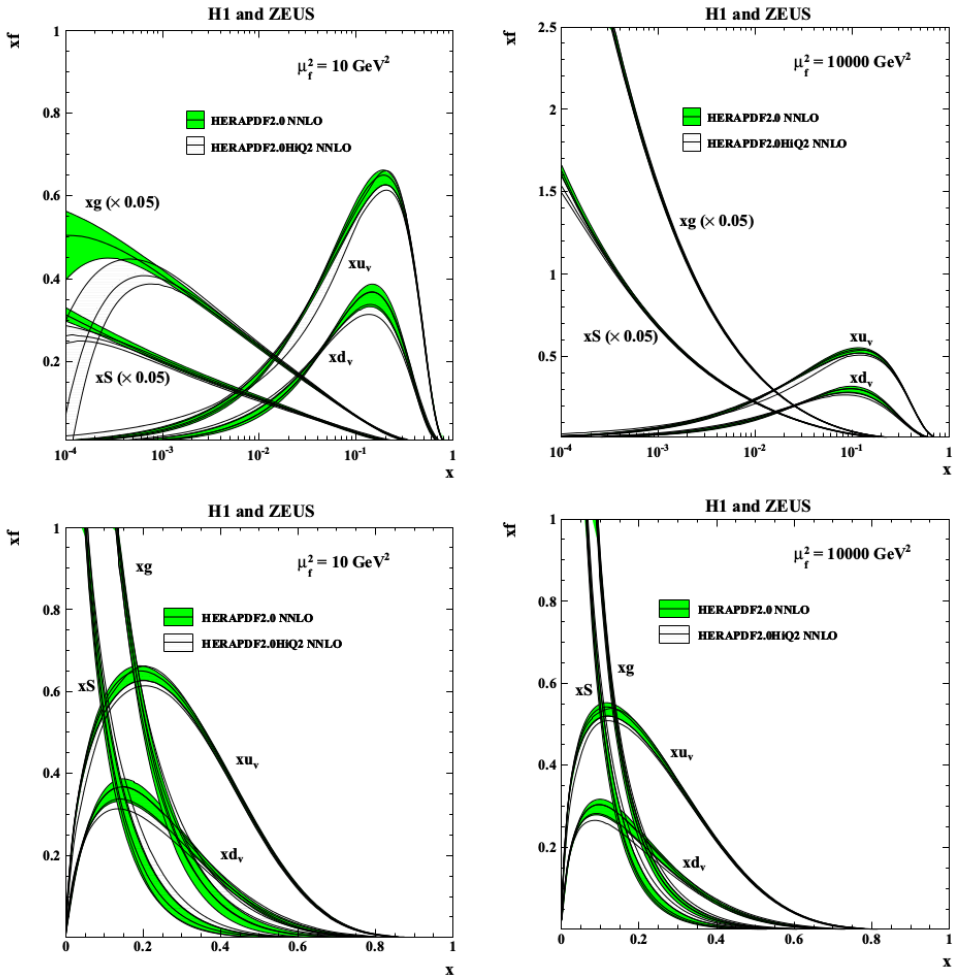

Figure 1.7: **(Next-to-Next-to Leading Order) NNLO PDFs extracted from DIS measurements recorded by H1 and Zeus at the DESY HERA accelerator.** These fits from H1 and Zeus PDF data show the expected probability (y-axis) of observing a quark of indicated flavor at a given momentum fraction (x-axis). Up and down flavored quarks are represented by u and d symbols. The lower case g is for gluon contributions and S is the light flavor nucleon sea defined in this graph as S=$(\frac{\bar{u}+\bar{d}}{2})$. On the left are PDFs calculations with a photon energy transfer of 10 GeV^2. On the right are calculations with a photon energy transfer of 10000 GeV^2. The top pair of graphs are log scale down to $x = 0.0001$ and the bottom pair are linear scale between 0 and 1. The green curves are results of the HERAPDF2.0 calculating program and the white curves are from the HERAPDFHIQ2.0 program.

where here, $D_{h/j}(z)$ is a *fragmentation function* (FF) or the number density of a hadron with flavor, h, produced from the fragmentation of a quark with j$^{\text{th}}$ flavor. A

formal definition of the FF is:

$$D_{h/j}(z) = C \sum_X \int \frac{d\xi}{2\pi} e^{ik^+\xi^+} \gamma^+ \langle 0|\psi_j(\xi^+)|p;X\rangle \ \langle p;X|\bar{\psi}_j(0)|0\rangle \,, \tag{1.15}$$

where C is a normalization constant involving averages over all colors, all spins, and the total momentum of the jet, X, $\frac{\text{Tr[Color]Tr[Dirac]}}{2N_{c,j}} \times \int \frac{d^3\mathbf{P}_X}{16\pi^3 P_X^0}$, k^+ is the backward facing quark momentum in the light front frame, and ξ^- is the dummy forward hadron momentum in the light front frame.

1.3.1 Nucleon Structure

An analysis of the PDF extractions from H1 and Zeus in Figure 1.7 warrants a detailed conversation about nucleon structure. The term "nucleon" comes from initial forays into nuclear physics by Heisenberg, where the proton and neutron were assumed to be abstract quantum spin states of a more fundamental particle, with pions as the bosonic internucleon communicators of the strong force [31]. As detailed earlier, the term parton technically refers to any constituent particle of a nucleon. The experiments at SLAC and corresponding theoretical advances in nucleon structure advanced the static and dynamic pictures of the nucleon, but data from HERA (and many other DIS experiments before it) have shown that understanding the nucleon is considerably more than confinement and color singlets. The theoretical, phenomenological, and experimental structures for which the Nobel Prizes were awarded to Kendall, Friedman, and Taylor in 1990 and Gross, Wilczek, and Politzer in 2004 were accurate with regards to the sum total of QCD and nuclear physics but in practice those discoveries really only present an initial point by which to understand the *valence quark* structure of the nucleon.

> **Valence Quark:** Of or pertaining to the "primary" quark singlet in a meson or baryon.

Discussion about the nature of the PDF involves an intimate conversation about quantum indeterminacy as PDFs are probabilistic measurements of momentum without corresponding position measurements, but another ambiguity exists in determining whether the struck quark in the DIS interaction is a valence quark or a member of the nucleon *quark sea*.

> **Quark Sea:** Of or pertaining to quarks that are not of the primary quark singlet in a meson or baryon. In color bound states virtual quark pairs are always spontaneously created and annihilated. It is impossible to reliably distinguish quarks in the valence singlet from those in the nucleon sea. Anti-quarks (and second or third generation *heavy* flavor pairs in mesons or baryons without a second or third generation valence flavor quark) are always sea quarks.

In Figure 1.7 the valence and sea structure can be immediately identified by observation. At both q^2 values the light quark PDF shapes as well as the location of and variance around the peaks confirm the flavor ratio of the color singlet and indicate that at any given time, the singlet carries greater than half of total proton momentum with the other fraction contributed by the gluons and light quark sea. Moving toward higher momentum fractions where observation indicates one or two of the quarks carry significantly more than half of total nucleon momentum, contributions from the gluons and light quark sea diminish significantly. At lower momentum fractions gluons and seaquarks dominate; however the momentum fraction at which they tend to dominate is inversely correlated with q^2.

Nucleon structure becomes more complicated if second and third generation quarks are considered as in Figure 1.8. As q^2 increases, the length scale of the interaction decreases allowing for the resolution of shorter lived heavy flavor $q\bar{q}$ pairs, some of which have more total energy than the nucleons in which they reside. The appearance of heavy quarks does not necessarily indicate more sophisticated nucleon structure than

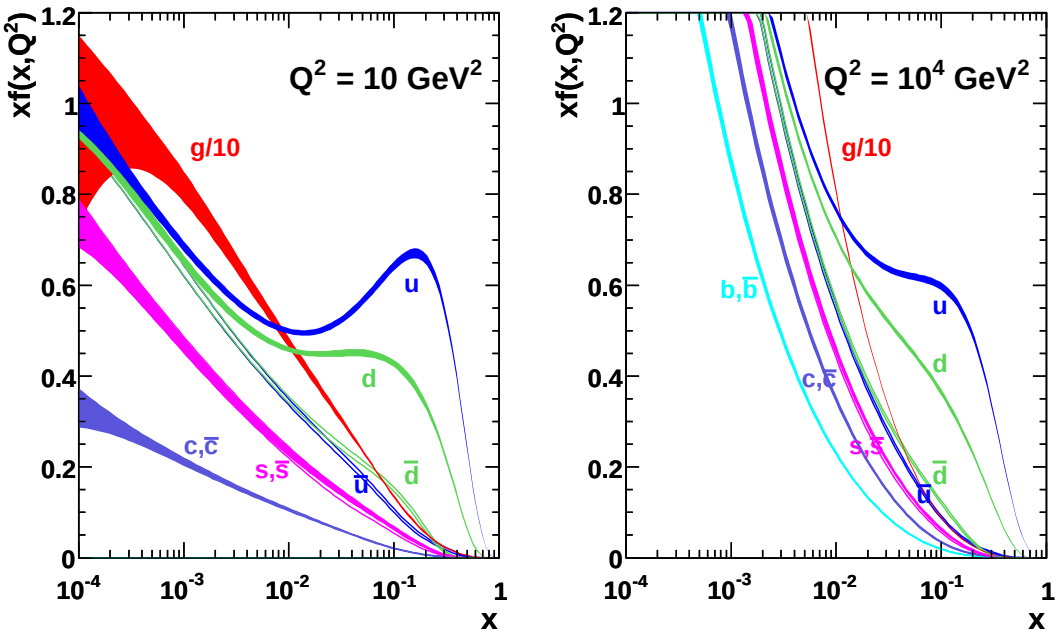

Figure 1.8: **NNLO PDFs calculated from world data by MSTW 2008.** These fits from global PDF data show the expected probability (y-axis) of observing a quark of indicated flavor at a given momentum fraction (x-axis). Up, down, strange, charm, and beauty flavored (anti-) quarks are represented by u($\bar{u}$), d($\bar{d}$), s($\bar{s}$), c($\bar{c}$), and b($\bar{b}$).

otherwise suggested, but differences between experimentally observed cross sections and those predicted by perturbative calculations imply that the quark sea may have non-perturbatively generated "intrinsic" or long term heavy components as well as contributions from "disconnected" sea-only processes [46, 47, 48, 49].

1.4 The Light-Quark Flavor Asymmetry and Drell-Yan Process

The revolutionary program at SLAC was an ideal laboratory in which to initially observe the particular idiosyncrasies of quark dynamics, and the particulars of static hadron flavor structure, but large swaths of unexplained territory exists concerning the strong nuclear force. In addition to the primary DIS program which set the

stage for the discovery of asymptotic freedom as well as the color and flavor structure of hadrons, phenomenological efforts to explain nucleon structure involved the same class of descriptors used by Bjorken called sum rules, one of which, the Gottfried Sum Rule (GSR), was an attempt to constrain valence quark flavor using prepublication data [50, 51]:

$$I_G = \int_0^1 \frac{dx}{x}\Big[F_2^{lp}(x,q^2) - F_2^{ln}(x,q^2)\Big]. \tag{1.16}$$

The purpose of the GSR was to verify the expected number densities of the valence singlet and measure the contribution of the nucleon sea to total nucleon charge by comparing lepton-proton with lepton-neutron interactions. At high energies, ($q^2 >> \Lambda_{QCD}$) the structure functions lose their q^2 dependence and can be treated as PDFs (as defined in equation 1.9):

$$\begin{gathered} I_G = \sum_i \int_0^1 e_i^2\Big[f_i^p(x) + \bar{f}_i^p(x) - f_i^n(x) - \bar{f}_i^n(x)\Big], \\ I_G = \int_0^1 \Big[u^p(x) - \bar{u}^p(x) + d^p(x) - \bar{d}^p(x) - u^n(x) + \bar{u}^n(x) - d^n(x) + \bar{d}^n(x)\Big]. \end{gathered} \tag{1.17}$$

Assuming global isospin symmetry for nucleons:

$$\begin{gathered} u^p(x) = d^n(x) \quad u^n(x) = d^p(x) \quad \bar{u}^p(x) = \bar{d}^n(x) \quad \bar{u}^n(x) = \bar{d}^p(x), \\ I_G = \frac{1}{3}\int_0^1 [u_v(x) - d_v(x)] + \frac{2}{3}\int_0^1 [u_s(x) - d_s(x)], \end{gathered} \tag{1.18}$$

where $f_{iv}(x) = f_i(x) - \bar{f}_i(x)$. The structure of the proton valence singlet allows for the evaluation of the following integral: $\int_0^1 [u_v(x) - d_v(x)] = 1$ which implies that the final form of the GSR is:

$$I_G = \frac{1}{3} + \frac{2}{3}\int_0^1 [u_s(x) - d_s(x)]. \tag{1.19}$$

The integral in the second term of the above equation should vanish if the quark sea in the proton is flavor symmetric. Instead, experimental data from multiple experiments show a clear violation of the GSR, indicating a fundamental misunderstanding of nucleon structure.

The first to partially measure I_G was a SLAC experiment with a maximum q^2 of 20 GeV^2 which recorded a value of $I_G^{SLAC}|_{0.02}^{0.82} = 0.200 \pm .04$, a 3σ difference from the expected calculation [52]. Later experiments confirmed the SLAC measurement using different leptons and baryon species and at higher energies. The European Muon Collaboration (EMC) at CERN, used DIS in muon-deuterium (D) and muon-iron (Fe) interactions to probe the differences in nucleon structure as a function of nucleus size. The maximum q^2 of the EMC experiment was 90 GeV^2 and it measured $I_G^{EMC}|_{0.02}^{0.8} = 0.197 \pm 0.011(\text{stat.}) \pm 0.083(\text{syst.}) \implies I_G^{EMC}|_{0.0}^{1.0} = 0.235^{+0.110}_{-0.099}$ [53]. The next two DIS experiments with GSR measurements were the Bologna-CERN-Dubna-Munich-Saclay (BCDMS) Collaboration and the New Muon Collaboration (NMC) which, like the EMC, used muon interactions on proton (H) and D targets and occurred at CERN after the EMC in the late eighties and early nineties. The respective maximum q^2 and GSR values retrieved from these two experiments were $I_G^{BCDMS}|_{0.06}^{0.8} = 0.197 \pm 0.006(stat.) \pm 0.036(syst.)$ at a $q^2 = 20$ GeV^2 and $I_G^{NMC}|_{0.004}^{0.8} = 0.221 \pm 0.008(stat.) \pm 0.019(syst.) \implies I_G^{NMC}|_{0.0}^{1.0} = 0.235 \pm 0.026$ at a $q^2 = 4$ GeV^2 [54, 55, 56, 57].

The nature of the measurements made by the EMC, BCDMS Collaboration, and NMC led to an ambiguity in interpretation of the results. To completely evaluate the GSR requires measurement of the full parton momentum fraction range and while partons with high momentum fractions contribute a vanishingly small amount to the total GSR integral it is difficult to estimate the total contribution from small-x partons [58]. This means that DIS measurements of the GSR have two possible interpretations: either the isospin symmetry of only the nucleon sea is broken (i.e. the

sea is not symmetric) or the small-x behavior of the nucleon is highly nonperturbative.

To decide which interpretation was correct, another class of experiments was introduced which used the Drell-Yan process to directly measure the ratio of light quark flavors in the nucleon. While it was not the first Drell-Yan experiment (earlier pion and proton induced Drell-Yan experiments had taken place at both CERN and Fermi National Accelerator Laboratory (FNAL/Fermilab)) the fifty-first experiment to occur at the North Area (NA51) of CERN was the first to directly observe the light quark flavor asymmetry (LQFA). The Drell-Yan process is the production of an $l\bar{l}$ pair from the annihilation of a $q\bar{q}$ pair as shown in Figure 1.9 [59, 60]. Among nucleons,

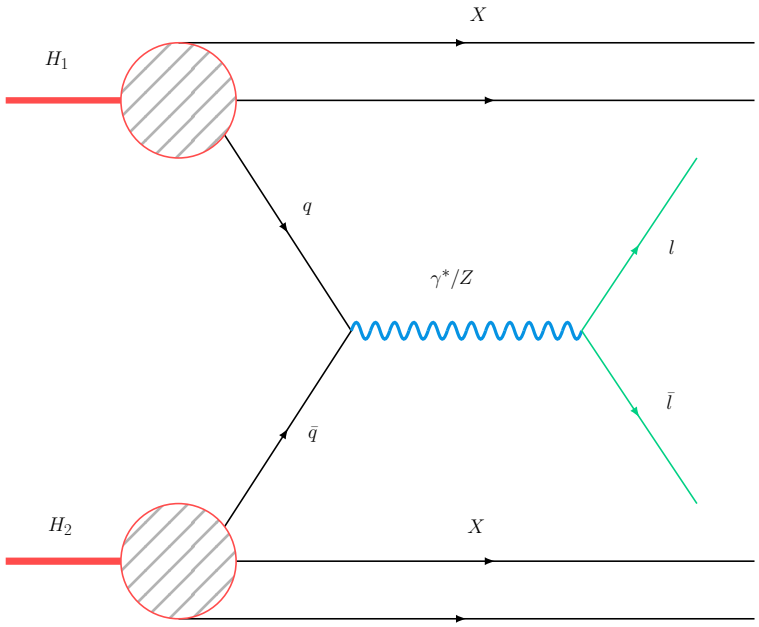

Figure 1.9: **Feynman diagram of the Drell-Yan Process.** DIS and Drell-Yan are topologically equivalent processes, indicating all lines are Fourier transforms of world lines and line definitions are equivalent to those in Figure 1.5. In this process, a $q\bar{q}$ pair from different nucleons annihilate to form a virtual boson which decays to a $l\bar{l}$ pair. The virtual boson in the Drell-Yan process could either be a highly offshell Z^0 boson or photon. The remnants of both nucleons are represented by X.

the annihilated anti-quark must come from the nucleon sea and measurement of both leptons should give some information about the produced virtual photon, the mass of

which determines the scale of the interaction. The factorized Drell-Yan cross section is:

$$\begin{aligned} \sigma^{NN\to l\bar{l}X} &= f(x)\otimes\bar{f}(x)\otimes\hat{\sigma}, \\ \frac{\sigma^{NN\to l\bar{l}X}}{dx_1dx_2} &= \sum_{i,j} f_{i/N}(x_1)\bar{f}_{j/N}(x_2)\frac{\hat{\sigma}}{dx_1dx_2}, \end{aligned} \tag{1.20}$$

and the process cross section is:

$$\frac{d\sigma}{dx_1dx_2} = \frac{4\pi\alpha_s^2}{9x_1x_2}\frac{1}{s}\sum_i e_i^2[f_{i1}(x_1)\bar{f}_{i2}(x_2)+\bar{f}_{i1}(x_1)f_{i2}(x_2)], \tag{1.21}$$

where x_1 and x_2 are the respective momentum fractions of the quark and anti-quark and $\sqrt{x_1x_2s}=M$, which is the mass of the virtual photon. CERN-NA51 measured $\frac{\bar{u}}{\bar{d}} = 0.51\pm0.04(\text{stat.})\pm0.05(\text{syst.})$ at a target momentum fraction of $x=0.18$ and a center of mass energy of 29.01 GeV^2 which supported the idea that the isospin symmetry in the nucleon sea was broken, however the degree of symmetry breaking warranted another more comprehensive measurement [61].

The followup was Fermilab Experiment-772 (E772) which attempted to probe the LQFA by comparing proton induced Drell-Yan on isoscalar (even number of protons and neutrons) D and Carbon (C) targets with an isovector (many more neutrons than protons) Tungsten (W) target at 800 GeV (maximum $\sqrt{s}=q^2=38.76$ GeV^2). While it was more sensitive to the nuclear effects than the LQFA and acknowledged that a more sensitive experiment would compare H to D, cross section comparisons provided additional constraints on the asymmetry which tempered results from CERN-NA51 [62]. Primary results are shown in Figure 1.10 [63, 64, 65].

In order to further constrain the measurements made by E772, Fermilab Experiment-866/NuSea (E866/NuSea) examined ratios of proton induced Drell-Yan from H and D targets. E866/NuSea not only measured a cumulative asymmetry integral $\int_0^1[\bar{d}(x)-\bar{u}(x)]dx = 0.118\pm0.012 \implies I_G^{E866}|_0^1 = 0.215\pm0.012$ but demonstrated an unequiv-

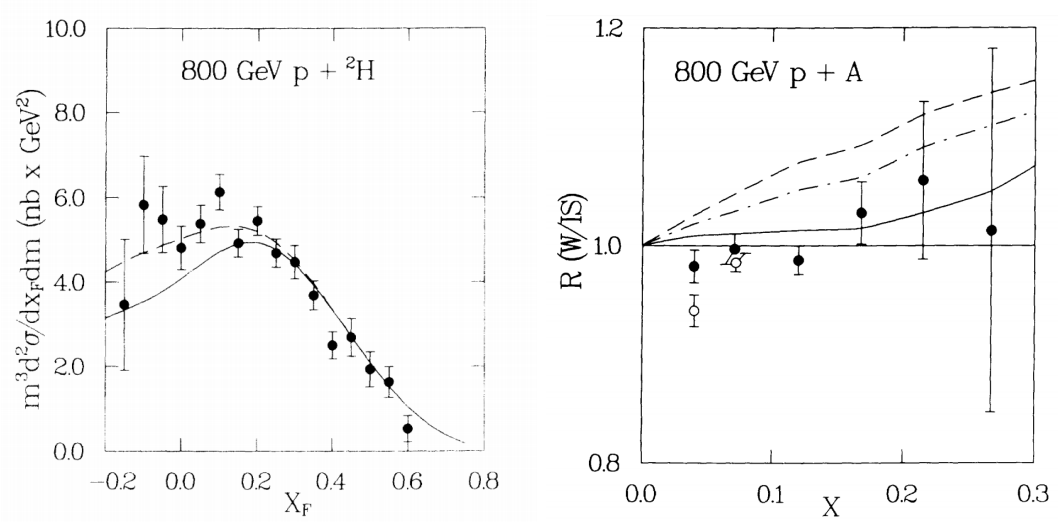

Figure 1.10: **Primary results of Fermilab E772.** On the left is the differential cross section with respect to the "forwardness" of the proton interaction with D. The solid (dashed) curve is a calculation of the D cross section using the Ellis-Stirling structure functions with (without) isospin symmetry of the nucleon sea. The figure on the right compares the recovered cross sections of W interactions to D (solid circle) and C (open circle) interactions. The curves are cross section ratio calculations using the Ellis-Stirling structure functions (dashed), Eichten-Hinchliffe-Quigg structure functions (dot-dashed), and the Kumano-Lundergan structure functions (solid).

ocal LQFA and displayed the dependence of the asymmetry on parton sea quark momentum fraction [66, 67]. Primary E866/NuSea results (which are shown in Figure 1.11) provided a robust calculation of the GSR but introduced a new mystery as the momentum dependence of the nucleon sea showed striking behavior. The flavor asymmetry measurement by E866/NuSea showed CERN-NA51 had measured the asymmetry of the nucleon sea at its maximum, but at momentum fraction ranges which favored the valence singlet, the relationship between sea quark flavors appeared to reverse.

The theoretical and phenomenological investigation of the nonperturbative processes contributing to the nucleon sea are varied. Field and Feynman suggested that the Pauli exclusion principle favored $\bar{d}$ in the nucleon sea because of the composi-

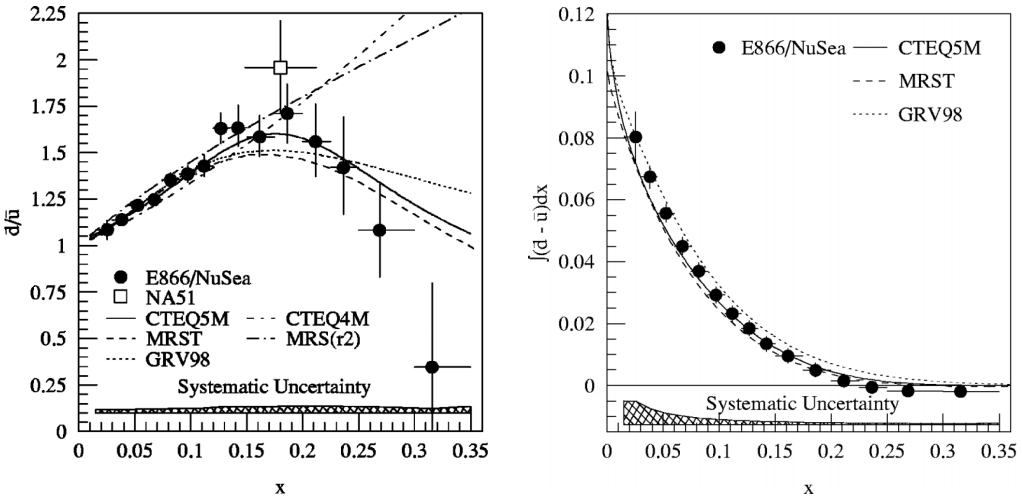

Figure 1.11: **Primary results of Fermilab E866/NuSea.** On the left is the $\frac{\bar{d}}{\bar{u}}$ ratio as a function of target quark momentum fraction evolved to a $q^2 = 54$ Gev^2. The right graph is the cumulative $\bar{d} - \bar{u}$ integral from $x = 0$ with $x = 0.35$.

tion of the valence singlet, but after results from the later DIS and early Drell-Yan experiments Steffens and Thomas calculated that contribution from this effect was negligible [68, 69]. A bevy of meson cloud models which emphasize different ratios of possible meson bound states within and between nucleons might also contribute to the asymmetry but the intractability of calculations as well as the lack of possible incisive bound state meson measurements make exclusion of possible models difficult [70]. Not only could meson bound states affect the distribution of quarks within the nucleon, but probing processes could also interact with the meson instead of the nucleon in what is known as the Sullivan process [71]. Finally, chiral quark models emphasize virtual meson coupling to individual quarks in the nucleon as opposed to nuclei, with uneven production a result of the flavor structure of the singlet [72]. To resolve the source of the asymmetry more experimental, phenomonological, and theoretical work is needed.

1.4.1 Fermilab Experiment-906/SeaQuest

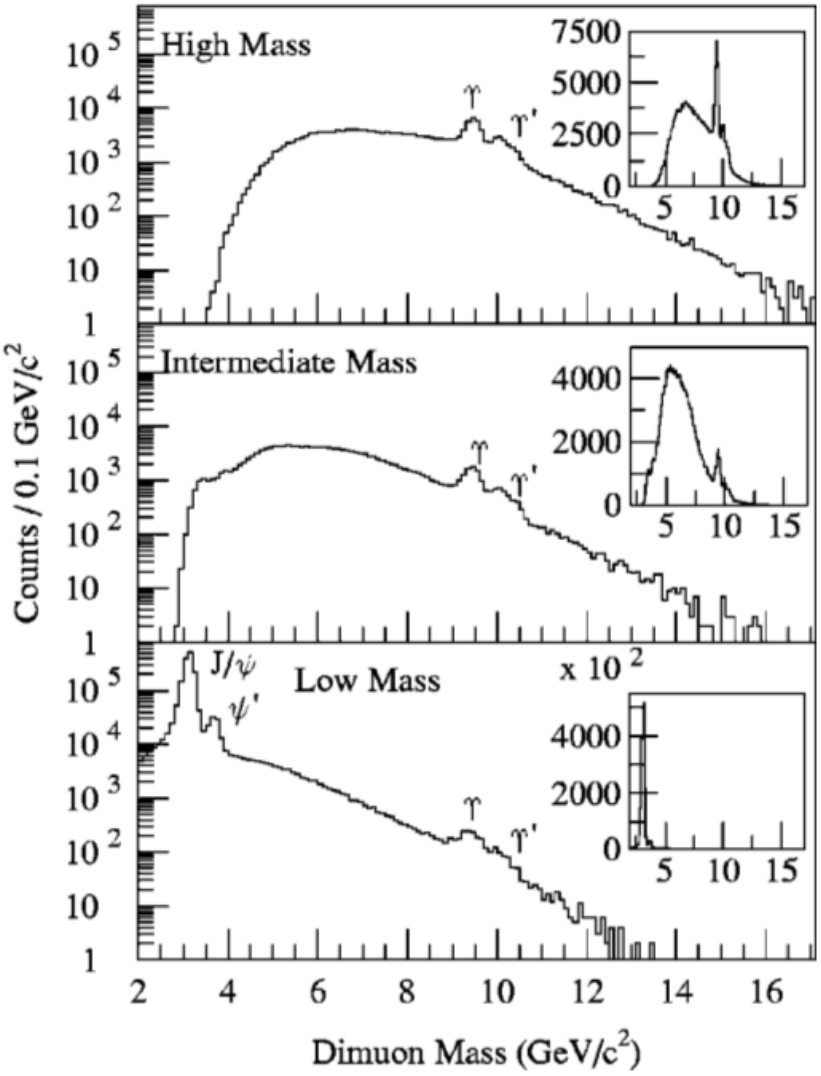

Figure 1.12: **E866/NuSea mass spectra.** E866/NuSea used three different magnet settings to privilege different mass regions. The high mass setting emphasized the production of the Υ(1S), Υ(2S), Υ(3S) and Drell-Yan over 12 GeV but recorded vanishingly small amounts of J/ψ. The intermediate mass setting emphasized the collection of Drell-Yan between 4 GeV and 9 GeV while still collecting equivalent amounts of both quarkonia states. The low mass magnet setting emphasized the collection of J/ψ(1S) and ψ'(2S) over Drell-Yan and Upsilon dimuons. Qualitatively E906/SeaQuest has a very similar mass spectrum but does not have the center-of-mass energy to observe a significant number of bottomonia.

Fermilab Experiment-906 (E906/SeaQuest) is the latest in a long tradition of fixed-target Drell-Yan experiments beginning with Fermilab Experiment-288, which discovered the upsilon (Υ) particle in 1977 [73]. The purpose of E906/SeaQuest is to observe various properties of nucleon structure, including the LQFA, using a spectrometer design reminiscent of E866/NuSea which observed the muonic products of Drell-Yan. Both experiments inevitably privilege the forward direction in acceptance, selecting the second of two terms in equation 1.21 which emphasizes high momentum fraction beam quarks and low to mid momentum fraction target anti-quarks. Direct background for both E866/NuSea and E906/SeaQuest consists of hadrons with dimuon decay channels and indirect background are hadrons with high decay rates to single muons. The E866/NuSea mass spectra shown in Figure 1.12 show that the biggest contaminations for Drell-Yan at this $\sqrt{s}$ and below are the charmonia resonances at 3.097 GeV and 3.686 GeV, with other contaminations coming from "randoms" or "accidentals" which are the muonic decay products of pions, kaons and other mesons and baryons [74, 75, 67].

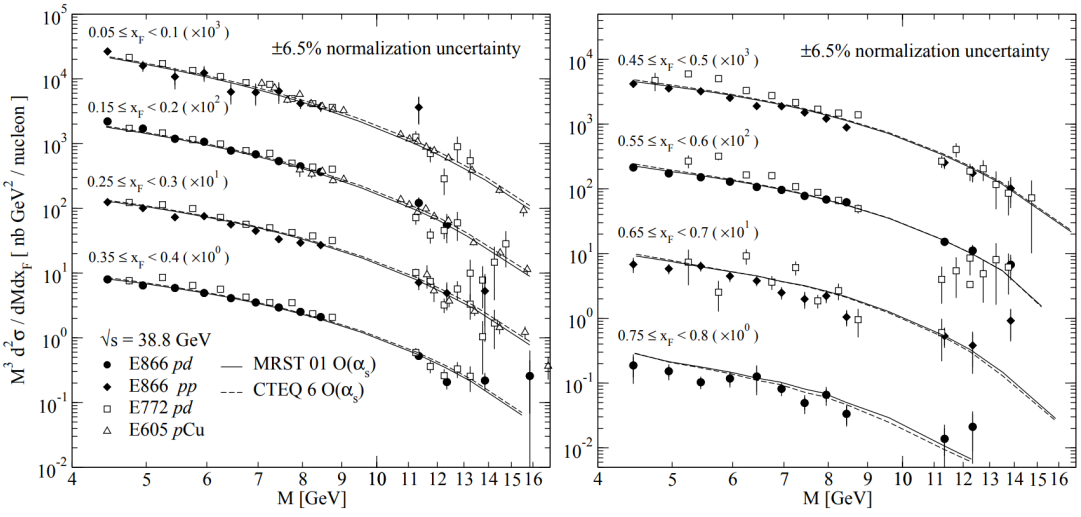

Figure 1.13: **Drell-Yan absolute cross sections as measured by E866/NuSea.** On the left are Drell-Yan cross sections with respect to dimuon mass and feynman-x. These cross section measurements do not include radiative corrections.

Differences between the two experiments center around a less energetic but more intense proton beam for E906/SeaQuest which has a beam energy of 120 GeV and intensity of 2.0×10^{12} protons per second, as opposed to an 800 GeV beam delivered at an intensity of 10^{11} protons per second for E866/NuSea. Momentum transfers and total center-of-mass energy are directly related to beam energy which, by equation 1.21 in the previous section, is in turn inversely related to Drell-Yan cross section, indicating that more Drell-Yan is produced per incident proton in E906/SeaQuest than in E866/NuSea. While Drell-Yan production is increased on a per-proton basis, E906/SeaQuest energies do not allow for a significant production of bottomonia. For comparison, absolute Drell-Yan cross sections as measured by E866/NuSea are shown in Figure 1.13 [76].

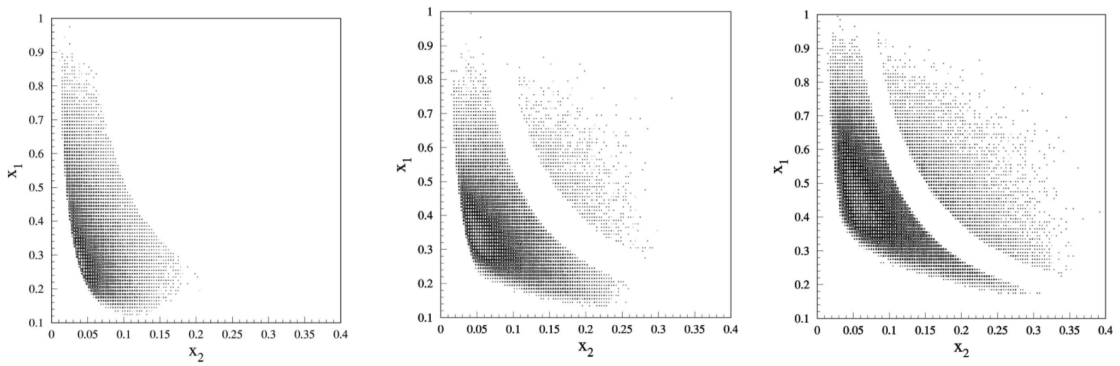

Figure 1.14: **E866/NuSea interaction kinematics.** In privileging the different Drell-Yan mass regions, the three magnet settings significantly change the kinematics of the observed Drell-Yan. The majority of events in the low mass setting (left) occur at a target momentum fraction of x=0.04, the intermediate range (middle) has a majority at x=0.06, the high range (right) has the majority of events at x=0.06 and achieves a higher hard scattering scale by privileging higher beam momentum fractions

Further implications of the large differences in beam energy combined with small differences in acceptance are the relatively large changes in observed kinematics, with the E866/NuSea Drell-Yan kinematical range available in Figure 1.14 [67]. The lower

beam energy delivered to E906/SeaQuest means muonic products are less boosted in the forward direction, leading to wider solid angle acceptance over a smaller longitudinal distance. This results in an experiment which has a larger fraction of total events in a relatively high mass region despite the fact that the absolute mass range of the E906/SeaQuest is lower than E866/NuSea. The wider angle of acceptance also allows E906/SeaQuest to achieve one of its design goals: higher reach into target momentum fractions.

1.5 Drell-Yan Angular Distributions, Boer-Mulders, and other Transverse Momentum Dependent Distributions

While an explosion of Drell-Yan experiments at Fermilab and CERN measured the cross section ratios of various nuclear species to understand evaluations of the GSR a parallel effort existed, aimed at understanding the particulars of the Drell-Yan process. Initial undertakings involved evaluations of lepton pair production with current algebras and an assumption that a virtual photon mediated production. With these assumptions, C.S. "Harry" Lam and Wu Ki Tung were able to generate a description of the angular distributions of an assumed two-to-two process with virtual photon structure functions:

$$\frac{d\sigma}{d^4q d\Omega} = \frac{1}{32\pi^4}\left(\frac{\alpha}{Ms}\right)^2 [W_T(1+\cos^2\theta) + W_L(1-\cos^2\theta) + W_\Delta \sin 2\theta \cos\phi + W_{\Delta\Delta}\sin^2\theta\cos 2\phi], \tag{1.22}$$

where W_T and W_L are the structure functions for transversely and longitudinally polarized virtual photons, W_Δ is the single-spin-flip structure function, and $W_{\Delta\Delta}$ is the double-spin-flip structure function [77]. A more precise definition relates these

structure functions directly to the hadronic tensor, defined as:

$$W^{\mu\nu}(P,S) = \int d^4x e^{ik\cdot x} \langle P,S|[J^\mu(x), J^\nu(0)]|P,S\rangle \,, \tag{1.23}$$

with the following relations:

$$\begin{aligned} W_T &= \epsilon_1^\mu(q) W_{\mu\nu}(P,S) \epsilon_1^{*\nu}(q), \\ W_L &= \epsilon_0^\mu(q) W_{\mu\nu}(P,S) \epsilon_0^{*\nu}(q), \\ W_\Delta &= \frac{1}{\sqrt{2}}[\epsilon_1^\mu(q) W_{\mu\nu}(P,S) \epsilon_0^{*\nu}(q) + \epsilon_0^\mu(q) W_{\mu\nu}(P,S) \epsilon_1^{*\nu}(q)], \\ W_{\Delta\Delta} &= \epsilon_1^\mu(q) W_{\mu\nu}(P,S) \epsilon_{-1}^{*\nu}(q), \end{aligned} \tag{1.24}$$

where $\epsilon_\sigma^\mu(q)$ is the polarization vector for the spin-1 virtual photon and, in this context, q is defined as the sum of the two lepton momentum vectors $q = l_1 + l_2$. The polarization vector can be defined in the Cartesian frame as:

$$\epsilon_1^\mu(q) = -\frac{1}{\sqrt{2}} \begin{pmatrix} 1 \\ i \\ 0 \end{pmatrix}; \qquad \epsilon_{-1}^\mu(q) = \frac{1}{\sqrt{2}} \begin{pmatrix} 1 \\ -i \\ 0 \end{pmatrix}; \qquad \epsilon_0^\mu(q) = \begin{pmatrix} 0 \\ 0 \\ 1 \end{pmatrix}; \tag{1.25}$$

with redefinitions of the polarization vector necessary to make sure the virtual photon aligns with both the hadronic and leptonic plane. If the spin-$\frac{1}{2}$ nature of the quarks are included in the model, a relationship between the longitudinal and double-spin-flip virtual photon structure emerges:

$$W_L = 2W_{\Delta\Delta}, \tag{1.26}$$

which with a simplification of the Drell-Yan angular cross section:

$$\frac{1}{\sigma}\frac{d\sigma}{d\Omega} = \frac{3}{4\pi}\frac{1}{\lambda+3}[1 + \lambda\cos^2\theta + \mu\sin 2\theta\cos\phi + \frac{\nu}{2}\sin^2\theta\cos 2\phi], \tag{1.27}$$

yields a Callan-Gross-like relationship called the Lam-Tung relation:

$$1 - \lambda = 2\nu, \tag{1.28}$$

where the three angular magnitude parameters are defined as $\lambda = \frac{W_T - W_L}{W_T + W_L}$, $\mu = \frac{W_\Delta}{W_T + W_L}$, and $\nu = \frac{W_{\Delta\Delta}}{W_T + W_L}$ [78, 79]. Integrating over θ ($d\Omega = \sin(\theta) d\theta d\phi$) yields a compact expression by which to directly probe the Lam-Tung relation ($\frac{3}{4\pi}(\lambda + 3) \to \lambda, \frac{3}{4\pi}\nu \to \nu$):

$$\frac{d\sigma}{d\phi} = \lambda + \nu \cos 2\phi, \tag{1.29}$$

The above integration and resulting equation also implies that the single-spin-flip term, μ, should vanish in integration over θ or ϕ and in practice vanish even in differential expressions.

Numerous attempts have been made to measure the validity of the Lam-Tung relation, most recently concluding with a trio of experiments at CERN and Fermilab. The CERN experiment at North Area 10 (NA10) observed pion induced Drell-Yan at 140 GeV, 194 GeV, and 286 GeV on W and D targets and found a violation of the Lam-Tung relation with a clear emphasis on the double-spin flip term [80, 81] (shown in Figure 1.15). Concurrently, Fermilab Experiment-615 (E615) also observed pion induced Drell-Yan on tungsten targets with a beam energy of 252 GeV and found qualitative agreement with CERN-NA10, however the extracted magnitude of the Lam-Tung violation was considerably higher than what was observed at CERN-NA10. The increase in degree of violation can be attributed to the nonzero μ and ν values. Results are shown in Figure 1.16 [82].

The third experiment to measure the magnitude of the modulations in Drell-Yan angular distributions was E866/NuSea which did so with an 800 GeV proton beam interacting with H and D targets. These data (shown in Figure 1.17) show a clear departure from the results of previous experiments [83, 1]. While the pion induced

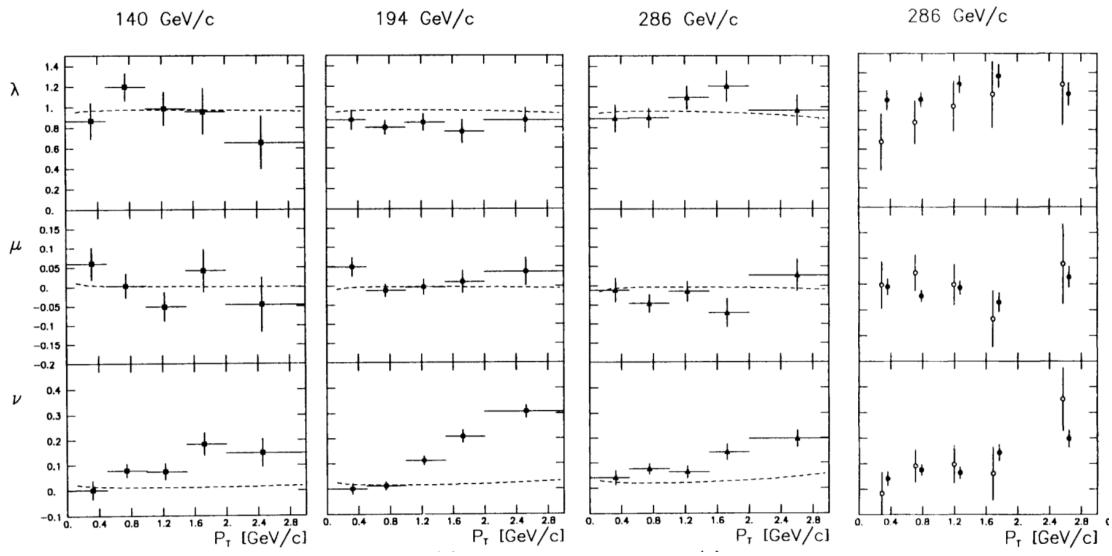

Figure 1.15: **π^-+W,D Drell-Yan angular modulation magnitudes measured by CERN-NA10.** The three left graphs are measurements of the magnitude of various angular modulations in Drell-Yan (λ, μ, and ν) as a function of transverse momentum at three different energies. The curved lines represent higher order corrections to the expected value of each modulation. The last graph on the right shows measurements of the same parameters in Drell-Yan from π^-+D interactions. On the right graph, black points are the $\pi^- + W$ measurements and open circle points are π^-+D.

Drell-Yan experiments both show large violations of the Lam-Tung relation the proton induced Drell-Yan show very small violations.

Explanations for the differences in the magnitude of the Lam-Tung violation center around explaining the difference in magnitude of the ν modulations. Obvious sources of the difference could be in the valence quark structure of the beam particle as well as the different hard scattering scales of the interaction or nuclei size dependent nuclear effects. Pion valence structure must include an antiquark which when involved in Drell-Yan with baryons is more likely to result in interaction with target valence quarks than the nucleon sea however, static valence structure does not explain the correlation of the ν-modulation magnitude with transverse momentum. At higher scattering scales, gluon fusion and scattering could contaminate Drell-Yan processes

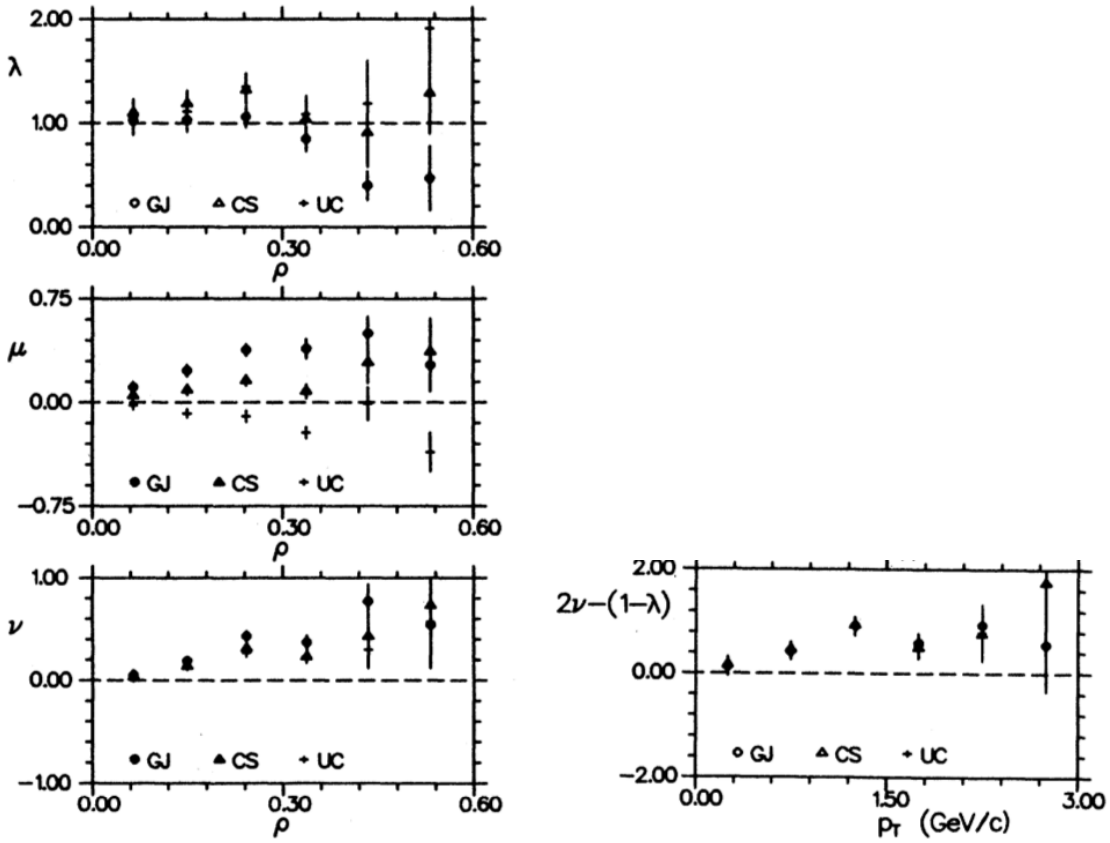

Figure 1.16: π^-**+W Drell-Yan angular modulation magnitudes measured by Fermilab E615.** The three left graphs are measurements of the magnitude of various angular modulations in Drell-Yan (λ, μ, and ν) as a function of the value $\rho = \frac{p_T}{M_{\mu\bar{\mu}}}$. The graph on the right is a calculation of the deviation of the Lam-Tung relation from zero as a function of p_T. Open circle points chart the measurement performed in the Gottfried-Jackson frame, the filled triangles indicate a shift to the Collins-Soper frame, the circle represents the Mandelstam u-channel frame.

leading to a large violation of the Lam-Tung relation, but is unlikely at the energy scale of E866 [84]. Nuclear effects might explain the dependence of the violation on transverse momentum, but gluon radiation in the beam or target quark would also affect the virtual photon polarization.

Other non-obvious explanations for the difference could be dynamic in nature and non-perturbative, possibly giving more insight into the origin of the LQFA. In

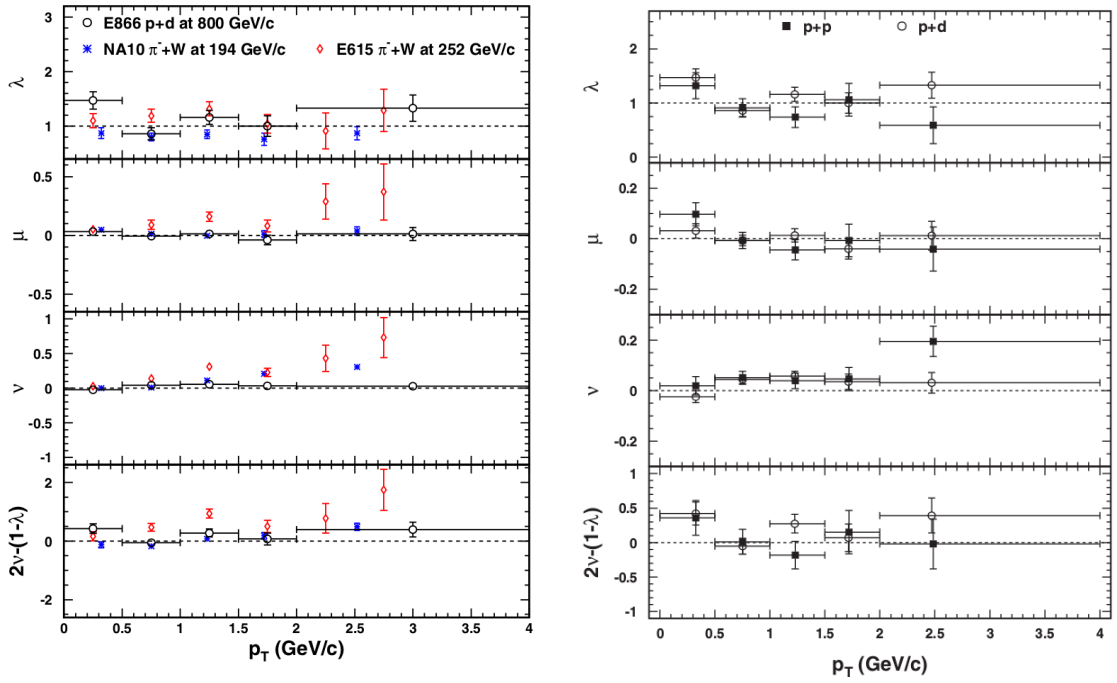

Figure 1.17: **p+H,D Drell-Yan angular modulation parameter magnitudes measured by E866/NuSea.** On the left are the angular modulation parameters as a function of p_T and an evaluation of the Lam-Tung relation for three different experiments: p+d from E866/NuSea (open circle), π^-+W from CERN-NA10 (blue star), π^-+W from E615 (red diamond). On the right are the angular modulation parameters and evaluation of the Lam-Tung relation for p+H (p+p) and p+D (p+d).

the original treatment of SLAC data, Bjorken and Paschos used a transformation to the infinite momentum frame ($q \to \infty$) to understand parton dynamics. This assumption included a corollary that parton transverse momentum was negligible. More recent formal treatments replace the infinite momentum frame with the light front frame (with calculations done in the accompanying gauge) which maintains the features necessary for incorporating asymptotic freedom and Bjorken scaling but also allows for the formulation of a new framework that describes possible "spin-orbit" and "spin-spin like" couplings between nucleons and their constituent quarks [85]. These correlations are known as Transverse Momentum Dependent distributions (TMDs) and were motivated by the study of what were assumed to be disparate effects in

lepto- and hadroproduction.

The first of three studies motivating the TMD framework posited the existence of the Sivers effect, a "spin-orbit like" coupling between initial state quarks with non-negligible transverse momentum and the longitudinal motion of a polarized nucleon. Observables of the initial state Sivers effect are a measurable preference in jet angular production from polarized proton interactions known as a single-spin production asymmetry (SSA) [86]. An unrelated followup examined how final state quark spin influenced hadron angle with respect to the fragmenting quark during hadroproduction, resulting in a distinct SSA known as the Collins effect [87]. The third study, by Daniel Boer and Piet Mulders, explored the Boer-Mulders effect or how a transversely polarized quark within an unpolarized nucleon might influence the production of hadrons in semi-inclusive DIS [88]. After furious theoretical work on the topic, including a definition of terms at the 2004 European Center for Nuclear Theory at Trento (and the introduction of the "Trento Conventions" for TMDs), a viable framework was finalized by John Collins in his textbook [89, 41].

A derivation of the TMDs starts with the quark-quark correlator in the light front frame [90, 91, 88, 92, 93]:

$$\Phi(x, k_\perp, S) = \int \frac{d\chi^- d^2\chi_\perp}{8\pi^3} e^{i(k^+\chi^- - k_\perp\chi_\perp)} \langle P, S|\bar{\psi}(0)\mathcal{W}(0,\chi)\psi(\chi)|P, S\rangle \tag{1.30}$$

where $\mathcal{W}(0,\chi)$ is the Wilson Line (or Gauge Link) which preserves the Lorentz invariance of the gauge fields in the expression despite the interaction of the initial state (or final state in the case of DIS) quarks with spectators. A Dirac projection of the correlator which is defined as $\Phi^{[\Gamma]}(x, k_\perp, S) = \frac{1}{2}\mathrm{Tr}[\Phi(x, k_\perp, S)\Gamma]$ leaves eight of the

thirty-two possible terms available at leading order (Twist-2):

$$\begin{aligned}
\Phi^{[\gamma^+]} &= f_1(x,k_\perp^2) - \frac{\epsilon_T^{ij} k_\perp^i S_\perp^j}{M} f_{1T}^\perp(x,k_\perp^2) \\
\Phi^{[\gamma^+\gamma_5]} &= S_z g_1(x,k_\perp^2) + \frac{k_\perp \cdot S_\perp}{M} g_{1T}(x,k_\perp^2) \\
\Phi^{[i\sigma^{i+}\gamma_5]} &= S_\perp^j h_1(x,k_\perp^2) + S_z \frac{k_\perp^j}{M} h_{1L}^\perp(x,k_\perp^2) \\
&\quad + \frac{\epsilon_T^{ji} k_\perp^i}{M} h_1^\perp(x,k_\perp^2) + S_\perp^i \frac{2k_\perp^i k_\perp^j - k^2\delta^{ij}}{2M^2} h_{1T}^\perp(x,k_\perp^2),
\end{aligned} \tag{1.31}$$

In this framework $f(x,k_\perp^2)$, $g(x,k_\perp^2)$, and $h(x,k_\perp^2)$ parameterize the magnitude of the "spin-orbit like" and "spin-spin like" correlation with respect to the polarization of the quark in the initial state, with f describing unpolarized quarks; the helicity functions, g, describing longitudinally polarized quarks; and the transversity distributions, h, describing transversely polarized quarks. The chart in Figure 1.18 describes the eight terms in 1.31 within the context of quark and nucleon polarization. Of the eight remaining functions, one exists with one defined direction of motion or spin (the unpolarized PDF $f_1(x,k_\perp^2)$ only has the longitudinal motion of the nucleon), two exist with two defined directions of motion or spin, and five functions have explicitly defined motion or spin defined which explicitly effect the symmetry of the functions. One of the functions which has two defined directions of motion or spin, the Boer-Mulders PDFs ($h_1^\perp$) is time and parity odd, indicating that it must be coupled with another chiral odd function in order to be observed. The Boer-Mulders PDF, which parameterizes the correlated motion generated by a coupling of a transversely polarized quark with an unpolarized nucleon, can be observed in Drell-Yan with the following integrated cross section:

$$\sigma_{UU} \propto f_1(x_1,k_{\perp 1}^2) f_1(x_2,k_{\perp 2}^2) + h_1^\perp(x_1,k_{\perp 1}^2) h_1^\perp(x_2,k_{\perp 2}^2)\cos(2\phi) \tag{1.32}$$

which, depending on the magnitude would register as a contribution to the tree level

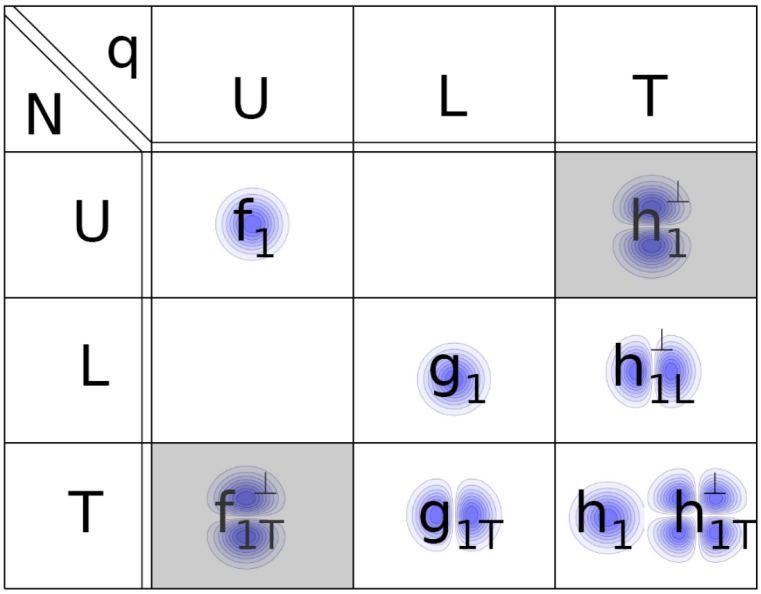

Figure 1.18: **Initial State TMDs at Twist-2.** The columns and rows of the chart describe three discrete polarization states which are also reflected in the symbols describing the magnitude of the correlation. The terms for a longitudinally polarized quark in an unpolarized nucleon and for a unpolarized quark in a longitudinally polarized nucleon do not exist because in the cases where spin direction align with nucleon motion, not enough vectors exist to define a preferred direction of coupled motion. The monopole, dipole, and quadrupole figures attached to each correlation function indicate the order of $\frac{k}{M}$ in the equation.

angular distributions cross section integrated over θ and resemble a violation of the Lam-Tung relation. The dependence on transverse momentum could be paramterized as a function of $k_{\perp}^2$ in the following form [94]:

$$\nu = 16C\frac{q_T^2 M_C^2}{(q_T^2 + 4M_C^2)^2}, \tag{1.33}$$

where C and M_C are fitting constants. This relationship has already been tested in E615, CERN-NA10, and E866/NuSea data and can be tested in the angular distributions of Drell-Yan dimuons at E906/SeaQuest.

CHAPTER II

The Fermilab Experiment-906 'SeaQuest' Spectrometer

Distilling all the physics in Chapter 1 into a practically achievable goal, ultimately, the mission of the SeaQuest Experiment is to measure muonic Drell-Yan cross sections in a range of nuclear environments. To do this, the experiment must be able to reliably generate, observe, and measure the properties of the muonic products of the Drell-Yan process. This is achieved through use of the SeaQuest Spectrometer, a custom designed fixed-target type, forward detector provided with accelerated protons by the Fermilab Main Injector (MI), the former supplier ring to the now retired Tevatron. The various sub-detectors and support systems which together make up the E906/SeaQuest Spectrometer are detailed in this chapter along with their individual operation and cohesive integration.

2.1 E906/SeaQuest Spectrometer Overview

In more detail, the E906/SeaQuest Spectrometer is designed to infer dimuon mass and momentum from position measurements of pairs of single muons produced in the Drell-Yan process with an approximate center-of-mass energy of 15.06 GeV, induced by a 120 GeV proton beam (.99996c average proton velocity) incident on a stationary

nuclear target. To this end, the spectrometer is twenty-five meters long and consists of a cycling stationary target table with two different liquid hydrogen isotopes, protium and deuterium, as well as three nuclear targets, solid carbon, iron, and tungsten. After the target is a five meter long iron-core "focusing" dipole magnet (dubbed FMag), which serves as a beam dump and muon filter. Following FMag is the first of four measurement stations made up of two spatial sub-detectors, the multi-plane Multiwire Drift Chambers (MWDC) and Scintillating Hodoscopes, both of which register muon transverse position at well defined longitudinal positions. Progressing further downstream, a smaller and weaker air-core "analysis" dipole magnet (dubbed KMag) is followed by the second and third measurement stations, a nonmagnetic solid iron "Muon Identification" wall, and the fourth and final measurement station which pairs the hodoscopes with plane arrays of Proportional Counter Drift Tubes (PCDTs) instead of a MWDC. An illustration of the entire E906/SeaQuest Spectrometer is shown in Figure 2.1.

Proton beam delivered to E906/SeaQuest by the MI sometimes falls well below and often exceeds the expected design intensity of the E906/SeaQuest Spectrometer, considerably complicating the reliable inference of muon properties from reconstructed particle tracks. Because of the intensity fluctuations, several additional subsystems are necessary: an instantaneous Proton Beam Intensity Monitor (BIM) based on a Charge Integrator and Encoder (QIE) board, a total Proton Beam Intensity Monitor (Unser Monitor) based on a Fast Current Transformer, and two corresponding dedicated DAQ systems.

2.1.1 Fermilab Main Injector Beam Structure

The E906/SeaQuest Spectrometer was designed to estimate Drell-Yan cross sections from measured dimuon yields by observing the products of 5.2×10^{18} protons in the interaction range of the target, over a two year run period. Given an expected

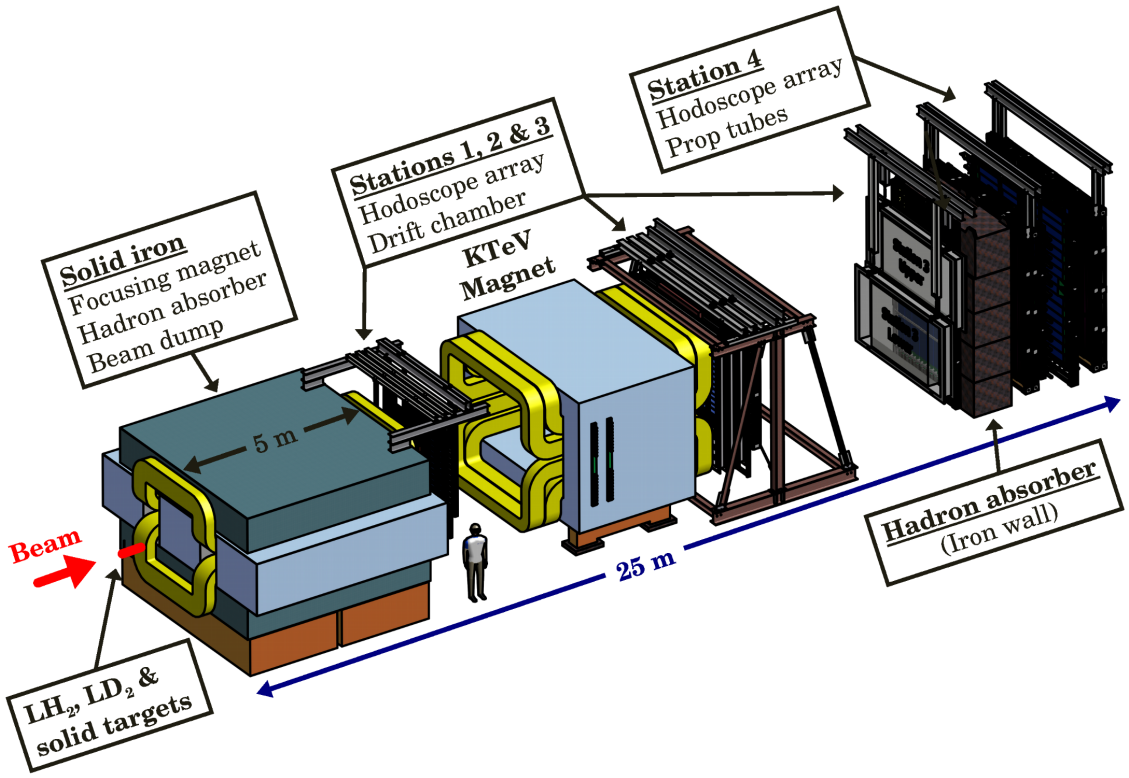

Figure 2.1: **The E906/SeaQuest Spectrometer.** Beam goes from left to right and magnet poles are designated in yellow.

incident beam intensity of 4.0×10^4 protons per pulse at a rate of one pulse every 19 nanoseconds for the duration of a four second "spill" occurring once every minute, cross sections could be calculated from yields using the following equation:

$$N_i^{q\bar{q}\to\mu\bar{\mu}} = \int \frac{dR_i}{dt} dt = \mathcal{L}_i \sigma_i^{q\bar{q}\to\mu\bar{\mu}} \int_0^{T_i} dt = \mathcal{L}_i \sigma_i^{q\bar{q}\to\mu\bar{\mu}} T_i, \qquad i = \mathrm{H}_2, \mathrm{D}_2, \mathrm{C}, \mathrm{Fe}, \text{and } \mathrm{W} \tag{2.1}$$

where $N_i^{q\bar{q}\to\mu\bar{\mu}}$ is the total Drell-Yan dimuon yield (in number of observed particles) from the relevant target, $\frac{dR_i}{dt}$ is the event rate in particles per unit time, $\mathcal{L}_i$ is the interaction luminosity which can be thought of as the number of chances a particular event has of occurring and is in units of inverse area-time, $\sigma_i^{q\bar{q}\to\mu\bar{\mu}}$ is the particle interaction cross section in units of area and can be thought of as the probability of

a particular event occurring, and t and T_i are the instantaneous time and total time, respectively. In reality, proton beam from the MI has significant time dependence stemming from how it is created and delivered to the spectrometer.

The entire process of generating and accelerating protons takes place in the Fermilab Acccelerator Complex (AC) and begins with ordinary hydrogen gas. A model of the AC is shown in Figure 2.2. Gaseous hydrogen atoms are injected into two magnetrons along with gaseous Cesium which forms a plasma and produces negatively ionized hydrogen at an energy of 35 keV. The magnetron cathodes feed directly into Low and Medium Beam Energy Transports which in turn feed directly into a Radio Frequency Quadrupole (RFQ) injector line, further accelerating the ionized hydrogen atoms to 750 keV. From there, the ionized hydrogen atoms enter a 116 MeV Drift-Tube Alvarez Linear Accelerator followed by a carbon foil which establishes beam structure at 53.1 MHz and strips the ionized hydrogen atoms of their electrons. The last linear accelerator, the Side-Coupled Cavity Linear Accelerator, accelerates protons from 116 MeV to 400 MeV and prepares them for injection into the Booster synchrotron accelerator.

In order to efficiently negotiate the transition from linear acceleration to accelerating in a ring, the 474 meter Booster synchrotron accelerates 84 proton pulses up to 8 GeV in groups called "batches" before they are "kicked" into the Recycler Ring. Additional beam structure is created in the Recycler Ring which can hold a total of seven batches in one "turn" of 588 pulses, however 92 radiofrequency pulse envelopes are always left empty in every turn as an injection and extraction window into and out of the ring, as well as an "abort gap" for beam dump in emergency scenarios.

Beam from the MI gets to E906/SeaQuest through the Fermilab Switchyard in a process known as "slow" spill extraction. Before extraction, beam pulses remain in circulation due to the successive focusing and defocusing effects of consecutive quadrupole bending magnets. This oscillatory transverse motion is known as betatron

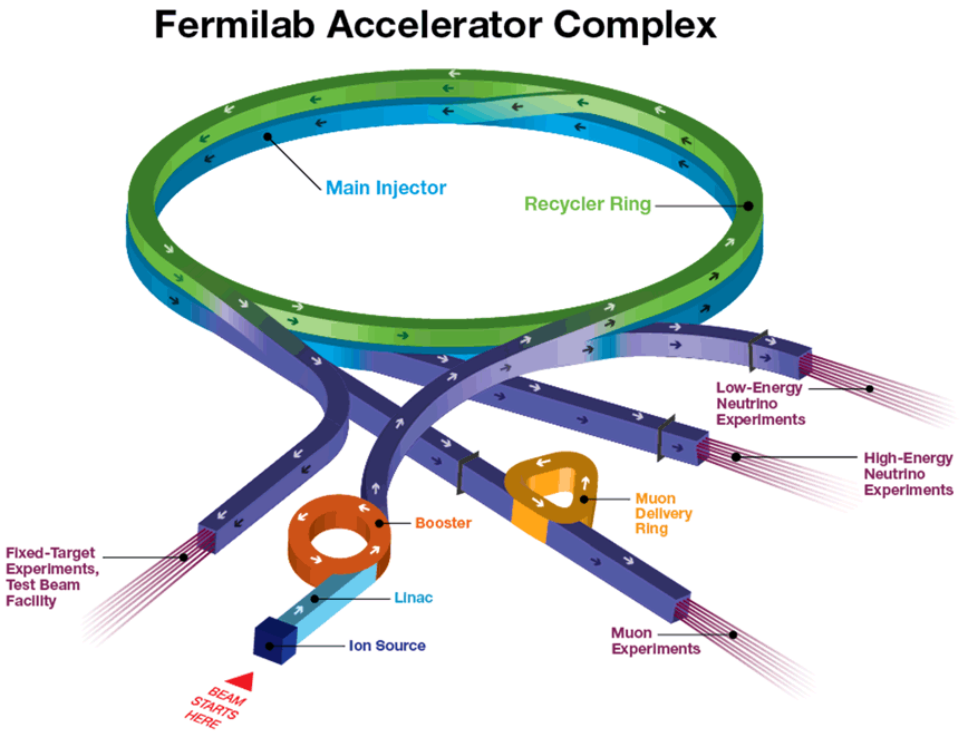

Figure 2.2: **Fermilab Accelerator Complex.** Beam starts with the Ion Source, proceeds through the Linear Accelerator (Linac) and is accelerated in the Booster Ring before being sent to the Recycler Ring and Main Injector. The vast majority of beam is sent to the local neutrino experiments (NOvA, MicroBooNE, MINERvA, MINOS, DUNE, and the Short-Baseline Neutrino Experiment) with the rest being sent to the Muon g-2 experiment, and the Switchyard which services the Fermilab Test Beam Facility and E906/SeaQuest.

motion. Slow spill extraction exploits betatron motion to divert circulating protons from the edge of their transverse spatial envelope using a pair of electrostatic septa. During the spill period, a kicker quadrupole is moved closer to circulating beam, destabilizing it just enough to graze the high field region of the septa and break off smaller beam pulses to be sent to the E906/SeaQuest Spectrometer.

In operation, betatron motion is highly dependent on accelerator "tunes" or perturbations of circulating proton paths from resonating frequencies which are further affected by the operating and electric power delivery frequencies of the focusing dipole and quadrupole magnets in the accelerator. Furthermore, Fermilab neutrino experiments like NOvA, the Short-Baseline Neutrino Program, DUNE, MINOS, and MINERvA require world-leading intensity for measurement of rare neutrino interactions, which motivates doubling load pulses in the transition from the Booster to the Recycler Ring through a process known as "slip-stacking"; however the process significantly alters the absolute transverse spatial envelope, or emittance ε, of circulating protons within the ring. The combined effects of all intentional and unintentional perturbations with imposed beam structure lead to large variations in the transverse position of individual proton positions between consecutive pulses which leads to significant pulse occupancy variations to incident proton beam in the E906/SeaQuest Spectrometer.

During physics data collection, the MI delivered a pulse once every 18.8 nanoseconds for less than 2 nanoseconds over a 3.9 second spill with an average measured pulse occupancy of 3.35×10^4 protons. Pulse occupancy, shown across different time intervals in Figure 2.3, varied across three orders of magnitude causing nearly empty buckets as well as in-time and out-of-time pile-up (colloquially called 'splat').

This difference is easily implemented in equation 2.1 by introducing time dependence in luminosity, but a time-varying luminosity represents a significantly more complicated experimental undertaking than otherwise implied:

$$\begin{aligned} N_i^{q\bar{q}\to\mu\bar{\mu}} = \int \frac{dR(t)}{dt} dt &= \int_0^{T_i} \mathcal{L}_i(t) \cdot \sigma_i^{q\bar{q}\to\mu\bar{\mu}} dt \\ &= \rho_i l_i \int_0^{T_i} \Phi_i(t) \cdot \sigma_i^{q\bar{q}\to\mu\bar{\mu}} dt, \qquad i = Targets \end{aligned} \tag{2.2}$$

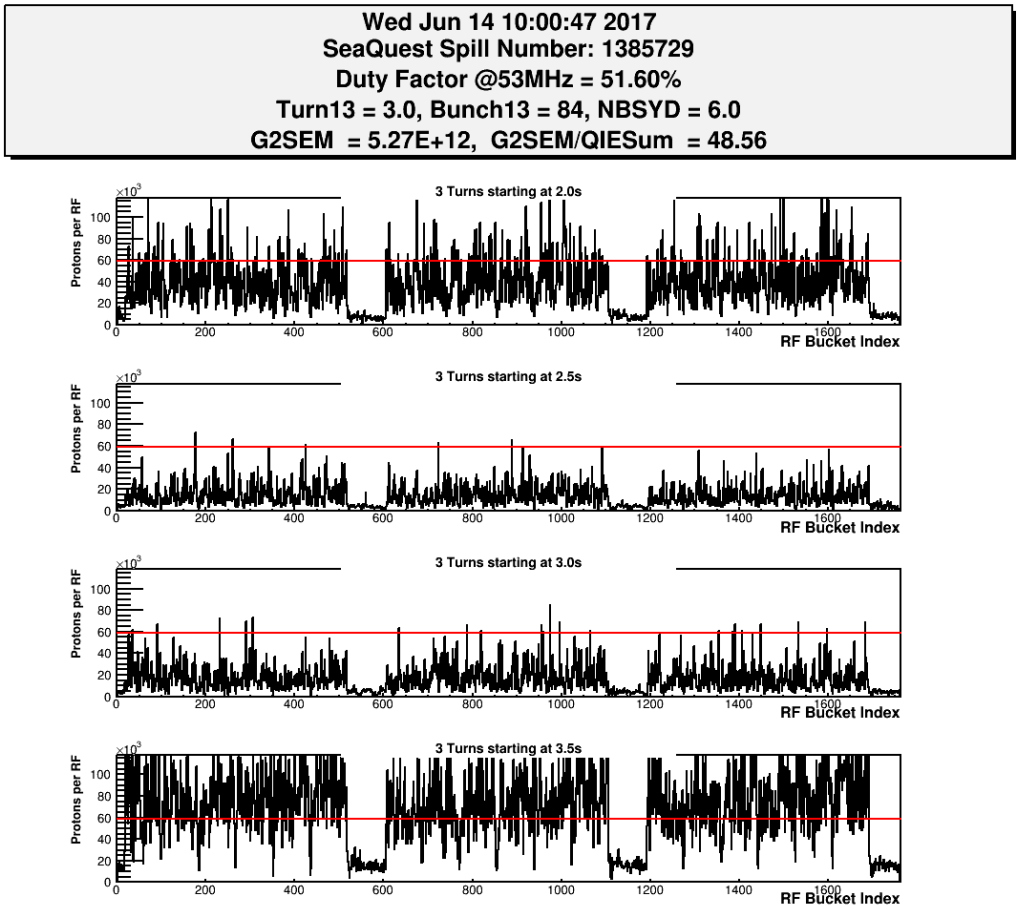

Figure 2.3: **Pulse Occupancy Spill #1,385,729.** More detailed online analysis of spills shows pulse occupancy varying from nearly no occupation to over 10^5 protons per pulse multiple times over the course of a spill. The red line represents the current trigger veto amount and an "RF Bucket" is a pulse.

Indicating that instead of inferring the Drell-Yan cross sections from observations of cumulative Drell-Yan yields over the course of the experiment for each target, each event (which is defined as the interaction of one pulse with the spectrometer) must be scrutinized with respect to its instantaneous particle flux, $\Phi(t)$.

Mitigation of the difficulties imposed by variation in pulse occupancy relied primarily on BIM integration into the E906/SeaQuest trigger as well as an event-based offline analysis of the BIM provided spill structure. A yet to be performed cross

section normalization using the Unser monitor will allow calculation of the Drell-Yan cross sections to within one percent uncertainty.

2.2 The Proton Beam Intensity Monitor

The BIM allows for the measurement of pulse occupation and ultimately, beam intensity, through the counting of protons intended for target interaction in consecutive pulses throughout the entire four second spill. This information can be integrated into the trigger system to avoid in-time pile-up and applied in offline analysis for the mitigation of efficiency losses from in-time and out-of-time pile-up.

Motivation for the BIM came during the commissioning Run period from March to April of 2012. It was observed that proton bunch occupation fluctuated by at least three orders of magnitude, leading to significant variations in instantaneous intensity and a duty factor of 34%. While target interaction with low occupation pulses produced events that fired the trigger and were reconstructed, Drell-Yan yield is directly proportional to intensity indicating a clear reduction in produced signal events. On the other end of the spectrum, high occupation pulses produced splat events leading to long detector dead-times as all event information was pulled from subdetector buffers and permanently stored. Additionally, high intensity events occupy a region of phase-space dominated by large pairs of single muons from unrelated background events, yielding low muon path reconstruction efficiency regardless of the presence of target Drell-Yan dimuon pairs.

Neccessary conditions for operation of the BIM were pulse-by-pulse beam resolution with negligible interaction of the beam exposed components. Indirect measurement of pulse occupation occurs through the observation of Cherenkov radiation induced by the pulse protons in the detector. Cherenkov photons are measured by a photomultiplier tube (PMT) and tallied by a custom NIM module. The dielectric medium contained in the BIM for charged particle interaction is an 80/20 mix

of room temperature gaseous argon and carbon dioxide cycled at a pressure only slightly above atmosphere, yielding a 1.000316984 index of refraction. The low density of the gaseous dielectric medium, the relatively thin aluminized mylar window, photon blocker, and titanium beam windows at either end of the pipe present a negligible scattering cross section to incoming beam. The entire device imposes 0.282 interaction lengths on incident beam before the target.

2.2.1 Hardware Components and Design

The physically interacting portion of the Proton BIM consists of 4 major parts: a custom built beam pipe section for use as a Cherenkov chamber, a custom built aluminized mylar window, a photomultiplier tube (PMT) and voltage sag resistant, fully transistorized PMT base paired with a neutral density filter, and a photon blocking material. The completed detector design is shown in Figure 2.4. The BIM is located

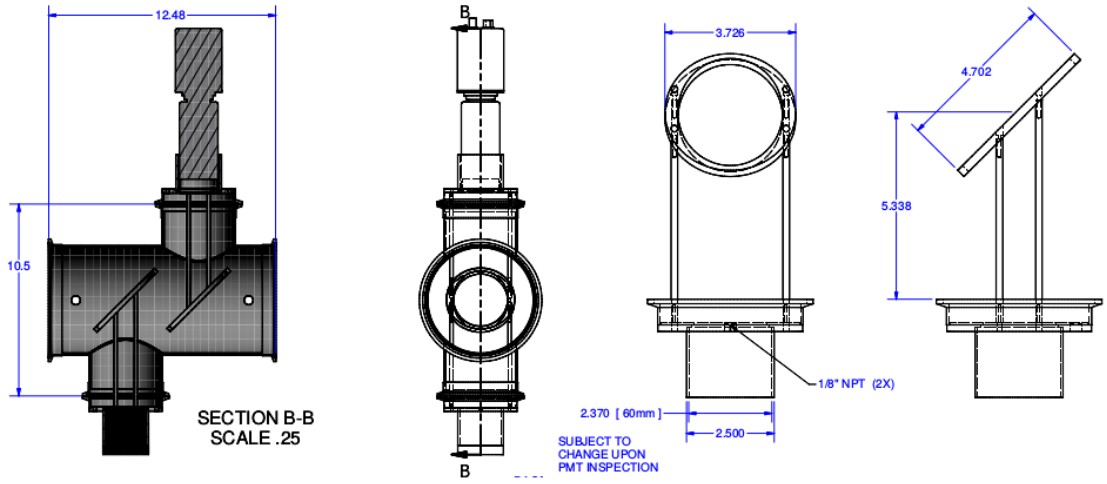

Figure 2.4: **Proton BIM Schematics.** Pictured from left to right are a side and beam perspective profile of the fully assembled Proton BIM with the PMT base combination and port cap and beam and side perspectives of the bezel supports for the aluminized mylar window and photon blocker.

roughly 7 meters upstream from the target enclosure giving roughly 23 nanoseconds

before interaction with the target. Both sides of BIM have a thin titanium beam window with one side leading to free atmosphere for interaction with Fermilab beam monitoring equipment.

The BIM beam pipe was fabricated from aluminum alloy and is approximately 31.7 centimeter long and 15.25 centimeter in diameter. The aluminized mylar window and photon blocker are mounted on two identical bezel supports and are fastened to stands which are mounted to port caps each with a slot reserved for the PMT. Planning diagrams for both the material support and stands are presented in Figure 2.4. Mirror and photon blocker support bezels are oriented at 45° with respect to the beam direction but the window portion of both bezels are parallel to each other in the path of the beam. The photon blocking material (in this case, a piece of black construction paper) is glued to the upstream bezel and its port closed with a plastic plug. Its purpose is to limit the size of the Cherenkov cone projected onto the PMT aperture. The bezel furthest down stream supports the aluminized mylar window which collects light and directs it towards the PMT.

2.2.2 Processing Components

Direct signals from the PMT and base combination are processed by a NIM fitted with a custom Charge Integrator and Encoder "QIE" circuit developed for the Compact Muon Solenoid Spectrometer (CMS) at the Large Hadron Collider (LHC) and first used in the Fermilab Kaons at Tevatron (KTeV) experiment. The primary function of the QIE board is to act as a real-time Analog-to-Digital Converter (ADC) and signal interpreter at the 18.8 nanosecond beam clock frequency, enabling *in-situ* measurement of pulse occupancy and trigger veto for splat blocking. Real-time analog-to-digital conversion is performed by the fully digitized and transistorized PMT base while real-time interpretation uses an on-board Field Programmable Gate Array (FPGA) loaded with a digitized and linearized look-up table to interpret 8-bit

signals from the PMT base as an intensity rating in "QIE units". The look up table is shown in Figure 2.5 along with a conceptual schematic of the modified NIM and logic diagrams for calculating beam measured during DAQ busy periods and trigger vetoing.

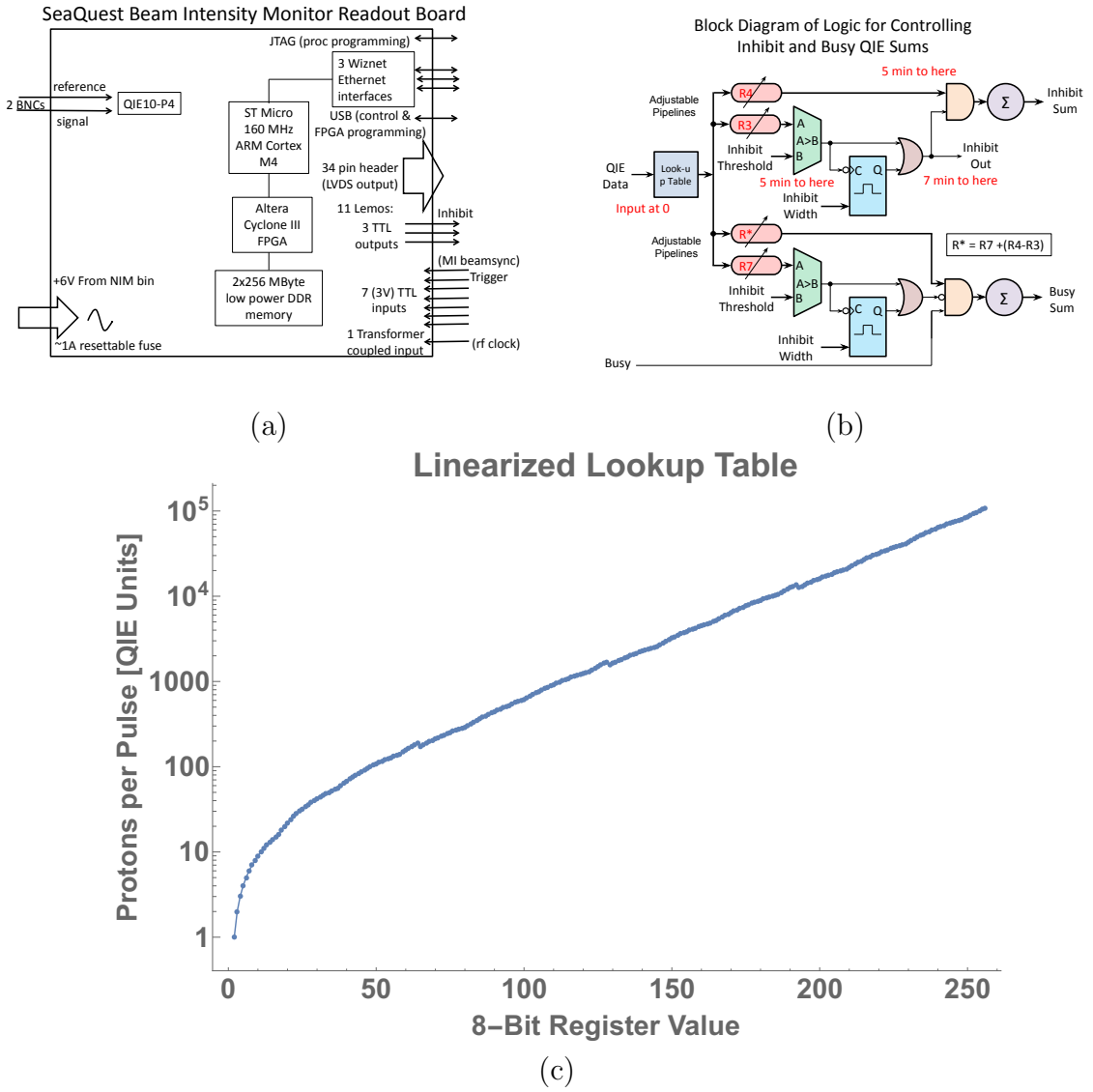

Figure 2.5: **QIE Board Schematics and Programming.** (a) Customized NIM board layout with associated hardware components. (b) Logic for calculating beam during DAQ busy periods and trigger vetoing (c) QIE Look-up table

In addition to pulse occupancy measurements for splat block, the QIE board also

has two 256 MB RAM banks for temporary storage of pulse occupancy values during the entire spill and instructions in the on-board FPGA for calculating various cross section normalization values which have become invaluable for all analyses. The entire suite of on-board measurements includes calculation of total integrated spill charge, charge missed during DAQ processing time, charge missed during trigger veto, pulse occupancy of triggered events, and spill duty factor. All intensity ratings are converted from QIE units to protons per pulse in offline analysis through normalization using the total integrated spill charge, an upstream Fermilab Secondary Emissions Monitor (SEM), dubbed "G2SEM" by the Fermilab Accelerator Division, and the following equation:

$$I_{\text{Event}} = I_{\text{Trigger}} \times \frac{I_{\text{G2SEM}}}{\sum_i^{N_{\text{Spill}}} I_i}. \tag{2.3}$$

Where I_{G2SEM} is the SEM measured value in protons per pulse, I_{Event} is the calculated intensity value of the event, I_{Trigger} is the measured intensity in QIE units, N_{Spill} is the number of events in the spill, and I is the measured intensity of ith event in the spill. Finally, the pulse occupancy of each induced beam event (triggering, veto, or busy) is recorded to tape as well as the occupation of a set number of events before and after each pulse, protecting against the relative long term effects of splat. A dedicated Beam DAQ system is responsible for accessing the QIE board from the custom NIM to perform additional online processing which is shown in Figure 2.3 and Figure 2.6.

2.3 The Target System

The E906/SeaQuest experiment provides multiple prepared nuclear environments for the production of Drell-Yan through the use of a cycling cryogenic targeting system. Five possible environments exist: liquid protium (LH_2) and deuterium (LD_2) provide information about protons and neutrons in similar nuclei (if isospin symmetry is assumed) and solid Carbon (C), Iron (Fe), and Tungsten (W) targets enable

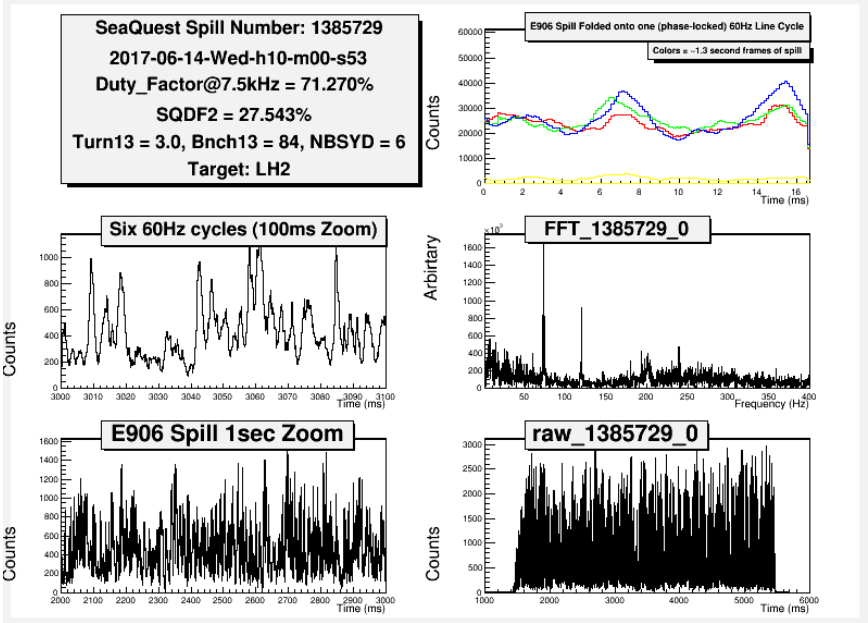

Figure 2.6: **Pulse Online Analysis Spill #1,385,729.** From the collected pulse occupancy data information about beam structure can be gathered and used for beam tuning.

E906/SeaQuest to probe some effects of the nuclear medium. Two additional target positions exist for background normalization purposes, one with a vacuum sealed vessel of the same type containing the liquid hydrogen and deuterium and another going directly to the beam dump.

Supporting hardware consists of a translational target table and proximity sensors which work together to physically support the targets and assign physical addresses for all possible target positions during cycling, dual cryogenic refrigerators, extensive dual vacuum systems, and various liquid and gas phase pressure and temperature sensing electronics. Operation of all supporting hardware is coordinated with a Programmable Logic Controller (PLC) which monitors all sensing electronics, sounds safety alarms, activates interlock conditions, and delivers telemetry to the Experimental Physics and Industrial Control System (EPICS) monitoring software. EPICS distributes information to other automated processes throughout E906/SeaQuest and its target telemetry output is stored on an event-by-event basis for detailed calculation

of luminosity.

2.3.1 Target Spatial Arrangement and Cycling

Originally, E906/SeaQuest requested 5.2×10^{18} protons on target with two-thirds of that beam incident on targets with light nuclei. In order to collect data in multiple nuclear environments while keeping systematic uncertainty as low as reasonably possible (a problem readily apparent in the results of the European Muon Collaboration which have high systematic uncertainty due to run periods which focus on one target at a time [95]), nuclear targets are swapped in between spills by an automated target motion system implemented on a translating table. The table is positioned directly in front of the last beam pipe in a designated high radiation area known as the target "cave" and supports all additional equipment for the safe operation of the liquid targets as well as the solid nuclear targets. From upstream of the target and oriented in the same direction as beam, all targets are arranged sequentially from left to right on a remotely operated table with a translation range of 91.4 centimeters. Properties of the five possible nuclear environments are detailed in Table 2.1. As illustrated in Figure 2.7, the vacuum sealed LD_2 target occupies the center of the table with the "Empty" target and LH_2 targets fanning out to the left and "No Target" position and solid targets fanning to right. Table motion is implemented through fixed nuts attached to a large lead screw which when rotated a fixed amount by a stepper motor, translates on tracks. The stepper motor receives rotation instructions from a separate motor driver which is given scripted movement instructions by a motor controller programmed by specialized Windows software.

2.3.2 Liquid Target Cryogenics and Vacuum System

Within the context of relevant physics observables, the two hydrogen targets enable some properties of light flavored seaquarks to be measured with minimal con-

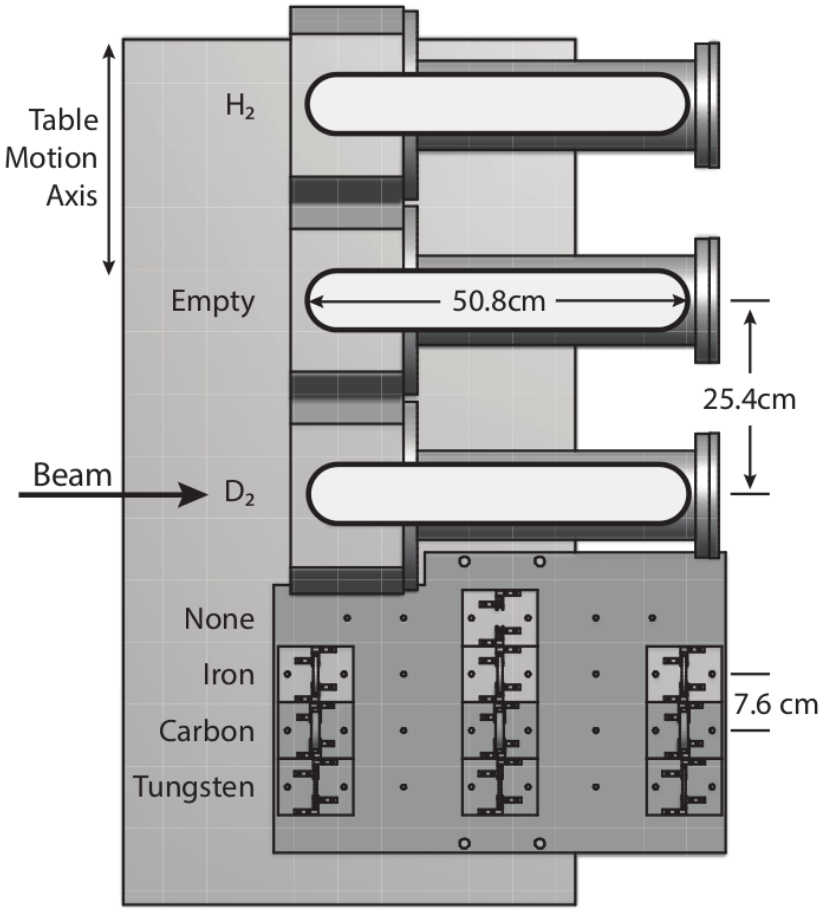

Figure 2.7: **Translational Target Table.** The target flasks are part of a larger insulating vacuum vessel increasing the necessary interval between liquid targets. The solid targets rest on a leveling table with precision drilled holes guaranteeing that all solid targets are at the same height. Immobile magnets are fitted directly in front of each target position on the same resting surface as the table and a sensor affixed to the table uses a short range magnetic field to determine which target is in position to accept beam.

tributions from interaction with the nuclear medium. However, hydrogen is a gas at standard temperature and pressure which is not ideal for use in a high-yield experiment. Cooling the hydrogen targets to liquid phase increases process luminosity by three orders of magnitude and leads to a reduction in spatial and temporal inhomgeneity during beam deposition but also introduces significant complication to the

Target Index	Target Nuclei	Atomic Number	Neutrons	Density (g/cm^3)	Target Length (cm)	Interaction Lengths	Left Spill Cycle	Right Spill Cycle
1	Liquid H_2	1	1	0.071	50.8	0.069	5	5
2	Empty Flask	–	–	–	–	0.0016	1	1
3	Liquid D_2	1	2	0.163	50.8	0.120	2	3
4	No Target	–	–	–	–	0	1	1
5	Fe	26	56	7.87	1.905	0.114	0	1
6	C	6	12	1.80	3.322	0.209	1	1
7	W	74	184	19.30	0.953	0.096	0	1

Table 2.1: **Nuclear Environment Cycling Details.** The target table translates left (west, -x) to right (east, +x) in the orientation of the E906/SeaQuest Spectrometer. A full spill cycle (cycles going left and cycles going right) lasts approximately twenty-four minutes and during that time approximately ninety-six seconds of beam is taken. Target cycles happen in between four second spills unless the table is directed to wait on a particular target for consecutive spill collection. A schematic of the target table is shown in Figure 2.7.

target system. Keeping both targets below their respective boiling temperatures of 20.15 K for protium and 24.15 K for deuterium (at standard pressure) required the use of a custom vacuum apparatus salvaged from NuSea/Experiment-866. A custom coldhead and compressor package acting as a cryogenic refrigerator for each isotope of hydrogen was integrated into the vacuum system to maintain cryogenic temperatures for an extended period of time.

Preparing either liquid target for data taking requires preparing the associated insulating vacuum chamber by using its associated Agilent/NRC/Varian HS/2 air-cooled diffusion pump. Each diffusion pump maintains nominal chamber pressure at 5.9×10^{-6} Torr during operation limiting conduction heat loss of the liquid through the 2.2 liter aluminum flask containing it. In addition to the flask, each chamber houses a Cryomech AL230 coldhead, which is capable of continuously applying 20 watts of cooling power to hydrogen gas until it condenses and drips into the flask. Phase dependent potentiometers at different heights in the flask, known as "level sensors", relay information about flask fill level. Once the associated flask is full of liquid, three Cernox temperature sensors attached to the coldhead monitor the temperature of the system and four 660 Ω resistance heaters with a maximum power output of 31.1 watts keeps the liquid from freezing. Phase diagrams indicating the operating

conditions of the two flasks are shown in Figure 2.8.

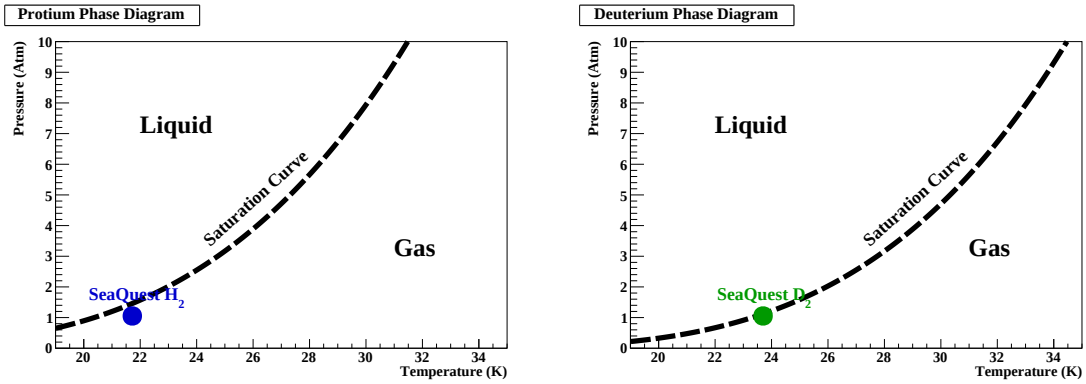

Figure 2.8: **Liquid Target Phase Diagrams.** The liquid targets both maintain liquid as evidenced by the level sensors, but measurements of temperature take place outside of the flask and pressure measurements occur both outside of the insulating vacuum and outside of the cave. This indicates target measurements of liquid flask telemetry are really measurements of hydrogen vapor saturated air, hence the target phase positions. It should be noted that saturated air would still be in equilibrium with the liquid in the flasks.

Outside of the cave, additional support hardware for the main vacuum and cryogenic systems is connected to the vacuum chamber through various stainless steel flex hoses. Dual Cryomech CP950 Compressors transfer heat from the gas through cryogenic cold heads and specialized helium charged lines that then dissipate the collected heat through water cycled by a single Durachill Polyscience water chiller. Other supporting vacuum hardware includes support for the diffusion pumps which are not operable above 2.0×10^{-3} Torr and must have vacuum prepared for them by Welch Duo Seal 1402 wet pumps. Those same pumps also act to evacuate diffusion pump exhaust and serve as emergency backup pumps in the event of an interlock activating event involving the high vacuum pumps. Flow diagrams of each integrated vacuum and cryogenic system are shown in Figure 2.9.

2.3.3 Target Monitoring and Control System

Target monitoring and control is implemented through an APACS+ central Programmable Logic Controller (PLC) manufactured by Siemens and comprised of seven different input and output modules. The seven PLC modules are the Advanced Control Module, which is responsible for managing the other six modules; two Standard Discrete Modules, which are responsible for interacting with digital sensors and controls; the Voltage Input Module, which receives measurements based on continuous differences in voltage; two Standard Analog Modules which actuate most valves; and a Resistance Temperature Module which records target temperature data. The PLC is programmed using Siemens associated Windows-based 4-Mation software and real-time telemetry and interaction is mediated with a Windows computer running GE Fanuc iFix software. Physically, intermediate target chambers are controlled by a series of electronic switches connected to pneumatically actuated valves with electronically actuated solenoid valves mediating the major connections from the pump cart to the insulating vacuum chamber.

The PLC manages all telemetry dependent interlocks, which keeps the target flasks from bursting or imploding due to extreme pressure changes, protects the insulation vacuum from condensation of vacuum contaminants, and protects all vacuum and cooling systems from overloading. It also manages automated table motion through the magnetic proximity sensors detailed in the previous subsection and coordinates Fermilab Main Control Room "ready" flags for beam delivery. Finally, the PLC monitors FMag current and prevents the chambers from being overloaded with direct beam.

2.4 The Spectrometer Magnets

E906/SeaQuest has two large magnets necessary for observation of Drell-Yan dimuons within the spectrometer. FMag, the larger and more powerful of the two magnets is of a single 5 centimeter aluminum "bedstead" coil recovered from the previous Fermilab Experiment-866/NuSea SM3 magnet. It runs nominally at 50 volts using 2,000 amps of current while consuming 50 kilowatts of power and generating a maximum field strength of 1.8 Tesla translating into an integrated magnet deflection of 3.07 GeV/c. Its primary purpose is to increase the total Drell-Yan dimuon yield from the target.

FMag serves this purpose in two ways: first, it forces dimuon pairs which would otherwise fall outside of the measurement stations, to curve back into the detector, increasing the overall geometric acceptance. Given this reasoning, multiple 43.2 cm $\times$ 160 cm $\times$ 503 cm slabs of 99.9% pure iron recovered from the Columbia University Nevis Laboratory Cyclotron were installed in the magnet core to increase field strength and maximize geometric acceptance. The second way the addition of the iron core increases total signal Drell-Yan dimuon yield is by counterintuitively enabling an increase in experiment luminosity, allowing the spectrometer to passively attenuate a more intense proton beam than would otherwise be tolerated by the measurement equipment.

The solid iron core enables the magnet to achieve a higher maximum than would otherwise be gained (at 1.8 Tesla) but the addition also introduces new challenges for dimuon observation. FMag gave consistent field strengths after accounting for the hysteresis of the iron, but multiple scattering under magnet drift in the iron significantly increases the systematic uncertainty of all reconstructed muon properties. In addition, even though the magnet acts as a hadron absorber for the remaining proton beam after passing through the target, significantly more background is produced

than would otherwise be observed in the spectrometer.

KMag, recovered from Fermilab Experiment 799/KTeV, is the smaller and less powerful of the two magnets with an active volume of 300 cm $\times$ 289 cm $\times$ 203 cm and a 0.4 Tesla maximum field strength, which is only an integrated magnetic deflection of 0.39 GeV/c. During nominal operation it maintains 1600 amps of current at 270 V and consumes 430 kW of power. The primary purpose of KMag is to impart a small transverse momentum "kick" to accepted muons for the calculation of particle momentum and charge.

Coarse magnet calibration for FMag was performed by the E906/SeaQuest collaboration and the KMag spatial field strength measurement was conducted by KTeV. Fine tuning of the each field strength map was done by examining the mass residuals of the $J/\psi(1S)$ resonance (3.097 GeV).

2.5 The Scintillating Hodoscopes

Reconstructing muon trajectories from the response of the E906/SeaQuest Spectrometer requires spatially and temporally collocating two different types of position measurements emphasizing precision in timing or physical path. The rapid response of the hodoscopes enables precise timing of muon trajectories paired with a loose spatial approximation, and the small amount of data as compared to the wire chambers makes the hodoscopes suitable for event triggering in E906/SeaQuest. A single hodoscope element is composed of a scintillating plastic paired to a PMT and PMT base. Element activation occurs when a charged particle of sufficient energy passes through the element and excites atoms that fluoresce in the material which is specially designed to channel generated photons to the attached PMT.

The first two stations have planes of hodoscopes arranged in x- (vertical) and y- (horizontal) directions perpendicular to the beam and each hodoscope plane is composed of two stand-alone modules of fanning elements which completely cover

Plane & Orientation	Number of Elements	Length(cm)	Width (cm)	Overlap (cm)	Total Module Width (cm)	z-Position (cm)
1-Y	20 × (Top/Bottom)	78.74	7.32	0.32	140.12	667
1-X	23 × (Left/Right)	69.85			162.01	
2-Y	16 × (Top/Bottom)	132.00	13.00	0.32	241.29	1403
2-X	19 × (Left/Right)	152.00			203.24	1421
3-X	16 × (Left/Right)	167.65	14.59	0.32	227.52	1959
4-Y1	16 × (Left) × (Left/Right)	152.4	24.48	0.32	365.80	2130
4-Y1	16 × (Right) × (Left/Right)					2147
4-Y2	16 × (Left) × (Left/Right)					2200
4-Y2	16 × (Right) × (Left/Right)					2216
4-X	16 × (Top/Bottom) × (Up/Down)	182.88	19.65	0.32	304.52	2235

Table 2.2: **Hodoscope Plane Scintallator Composition.** Hodoscope planes in station 1 and 2 are divided into Top and Bottom modules for x-direction measurement and Left and Right for y-direction measurement. Station 3 does not have a y-direction measuring module and station 4 has two sets of y-direction measuring hodoscopes which in addition to being divided into Left and Right modules like y-direction Hodoscopes from other stations, are also further divided into a second level of Left and Right modules. Only the x-direction hodoscopes are used for triggering.

the acceptance of the high-resolution drift chambers. The fluorescent material in the first two stations is "BC-412" a scintillating plastic manufactured by the Bicron Company and scavenged from the HERMES Experiment at DESY. The material has an attenuation length of 2.1 meters, a light output of 60% Anthracene, a rise time of 1 nanosecond, and a pulse length of 4 nanoseconds.

Hodoscopes in the third and fourth stations are slightly different in configuration and construction because they were made from new components for E906/SeaQuest and must cover a larger transverse area associated with larger wire chambers. The scintillating material is new Eljen "EJ-200" which has an attenuation length of 3.8 meters, a light output of 64% Antracene, a rise time 0.9 nanoseconds, and a pulse length of 2.5 nanoseconds. The biggest difference between the first two stations and the last two stations is the number of measuring planes for each station. The third station only has an x-direction measuring plane while the fourth station has an extra y-direction measuring plane. Additionally, each of the measuring planes in the last two stations is divided into more than two modules.

Attached PMTs for stations 1 and 2 were recycled from the HERMES experiment while new Hamamatsu brand PMTs were fitted to elements on stations 3 and

4. Due to the relative size of station 4, elements in physically divided modules were fitted with PMTs effectively treating two individual elements within different modules as one element with regards to triggering and data taking. Output from all PMTs were "clipped" to a pulse maximum of 15 nanoseconds from 25 nanoseconds allowing per-proton-pulse trajectory timing. To prevent efficiency-harming voltage "sagging", which becomes significant in the first two stations due to a much higher relative particle flux as compared to stations three and four, PMT bases were "fully transistorized". Spatial details of all hodoscope measurement planes are shown in Table 2.2. Of particular interest, all hodoscopes in all planes overlap each other by 0.32 centimeters, eliminating any gap in acceptance and improving total trigger efficiency, but possibly contributing to experiment "pile-up" from the double counting of particles passing in the overlap region.

2.6 Wire Chambers

Precise observation of muon trajectories in three-dimensional physical space is possible through the use of wire chambers which are present in all spectrometer stations. The simplest conceptual picture of a wire chamber is an array of charged conducting wires placed in an ionizing gas and electric field. When a charged particle passes through the plane it ionizes the gas, producing free electrons which drift towards the wire. A change in wire charge registers as an activated wire and is interpreted as a "hit" generated by an energetic muon. A single plane would only correspond to a location in one dimension of measurement. Multiple planes with differing orientations placed in close consecutive proximity give hit information in multiple dimensions. It can be assumed that wherever activated lines intersect a charged particle passed in each chamber.

Station	Orientation (Angle)	Number of Elements	Cell Width(cm)	Spacing(cm)	Plane Height(cm)	Plane Width (cm)	z-Position (cm)	Resolution (cm)
1	U/U′ (14°)	201	0.635	0.635	101.60	121.92	594/595	0.022/0.021
	X/X′ (0°)	160					617/617	0.026/0.026
	V/V′ (-14°)	201					637/638	0.021/0.020
2	V/V′ (14°)	128	2.02	2.02	264.16	233.28	1315/1321	0.033/0.031
	X/X′ (0°)	112	2.08	2.08			1347/1340	0.033/0.033
	U/U′ (-14°)	128	2.02	2.02			1366/1373	0.033/0.032
3-Minus	V/V′ (14°)	134	2.0	2.0	166.00	320.00	1889/1887	0.024/0.024
	X/X′ (0°)	116					1895/1893	0.026/0.026
	U/U′ (-14°)	134					1901/1899	0.024/0.024
3-Plus	V/V′ (14°)	134					1925/1923	0.024/0.024
	X/X′ (0°)	116					1931/1929	0.025/0.025
	U/U′ (-14°)	134					1937/1935	0.023/0.023

Table 2.3: **Multiwire Drift Chamber Plane Spatial Arrangement.** The z-position of every precision measuring plane along with its muon hit resolution is displayed in the table above. The closer the station is to the interaction point, the higher the hit rate for that station. Station one has a higher density of smaller sense wires than stations two and three but roughly the same resolution as larger chambers with larger wires because of the relatively high hit rate.

2.6.1 Multiwire Drift Chambers

The MWDCs in E906/SeaQuest operate on the principle outlined above and have many characteristics in common but the details of implementation across the three measurement stations differ. Each precision station has six separate consecutive planes corresponding with three linearly dependent measurement orientations, the x-direction, which has vertical wires, and the u- and v-directions which have wires oriented 14° and -14° with respect to vertical. Pairs of consecutive planes are oriented along the same measurement direction but are staggered in position by half of a cell spacing allowing for stereoscopic observation in each dimension. Spatial details of each precision plane measurement are shown in Table 2.3. Finally, practical application of MWDCs requires more than hit signal generating wires. Static electric fields in each chamber are induced by field wires which are located in sense wire interstices.

Plane idiosyncracies begin with wire size and composition and extend to chamber voltages, plane order, and general construction. A summary of average wire voltage, wire diameter, and wire composition for all wire chambers is shown in Table 2.4. MWDC cathodes are a necessary component of each station plane for field continuity and are implemented in the first station as a pair of two dimensional sheets located

Station	Wire Type	Material	Wire Diameter (μm)	Gas	Nominal Voltage (V)
1	Sense	Gold-plated Tungsten	25	(Ar(88%):CH_4(8%):CF_4(4%))	1500
	Field	Beryllium-Copper	62.5		0
2	Sense	Gold-plated Tungsten	25	(Ar(88%):CH_4(8%):CF_4(4%))	0
	Field Cathode	Beryllium-Copper	62.5		-1850
3-Minus/Plus	Sense	Gold-plated Tungsten	30	(Ar(88%):CH_4(8%):CF_4(4%))	0
	Field Cathode	Beryllium-Copper	80		-2400
	Guard				-1300
4-Prop Tubes	Sense	Gold-plated Tungsten	20	(Ar(88%):CH_4(8%):CF_4(4%))	2000

Table 2.4: **Wire Chamber Plane Material Composition.** All sense wires in all wire chambers are Gold-plated Tungsten and all wire chambers are filled with the argon, methane, and tetraflouromethane gas mix. Station three has guard wires which are necessary to maintain field continuity at the edges of the chamber. In stations one and four the sense wires are positively charged and the cathodes are held at ground, while stations two and three are held at negative potential while the field wires held at ground.

upstream and downstream of a plane of alternating sense wires. In other precision stations arrangements of cathode wires replace continuous planes, but cathode wire arrangement differs from station two to three. Station two has cathode wires arranged in separate planes similar to station one while station three has cathode and field wires arranged in two dimensional cells surrounding sense wires. Additionally, station four has an additional type of wire to insulate sense wires of differing orientations from each other.

In terms of general construction, station one, which was constructed for use in Fermilab Experiment 866 [66, 67], has all wires and planes contained within a single chamber. Station two is also completely contained within a single chamber while station three is divided into two independent chambers. The bottom of station three (Station 3 Minus) along with all of station two were created for use in Fermilab Experiment 605 [96]. The top of station three was built for E906/SeaQuest. All precision measurement chambers are filled with a mix of argon, methane, and tetraflouromethane (Ar(88%):CH_4(8%):CF_4(4%)).

Prop Tube Plane & Orientation	Relative Position	Number of Elements	Cell Width(cm)	Spacing(cm)	Plane Length (cm)	Plane Width (cm)	z-Position (cm)
1-Horizontal	Forward Backward	144	4.76	0.32	368.30	777.24	2097-2099 2102-2103
1-Vertical	Forward Backward	144	4.76	0.32	777.24	368.30	2174 2179
2-Horizontal	Forward Backward	144	4.76	0.32	368.30	777.24	2389-2390 2393-2394
2-Vertical	Forward Backward	144	4.76	0.32	777.24	368.30	2367 2371

Table 2.5: **Single-Wire Proportional Counter Tube Plane Composition.** Prop tube planes are identical in construction with changes in orientation for the different measurement directions.

2.6.2 Single-Wire Proportional Counter Tubes

For the fourth station, instead of pairing a MWDC module to hodoscopes to create an additional point for calculating trajectories, "Muon Identification" is implemented with the use of four Single-Wire Proportional Counter Tubes ("Prop Tubes") planes and a one meter thick iron wall. Particles must traverse the iron wall (after passing through every station in the spectrometer) and register in the prop tubes of the final station in order to be counted as an observed muon. The prop tubes are arranged vertically for measurement in the x-direction and horizontally for the y-direction. An individual proportional counter tube is composed of a single 20 micron diameter tungsten wire within a 5.08 centimeter tube, stretched taught along the entire 3.65 meter length of the tube. Prop tube construction is detailed in 2.5. Each tube is filled with the same (Ar(88%):CH_4(8%):CF_4(4%)) mix as the MWDC.

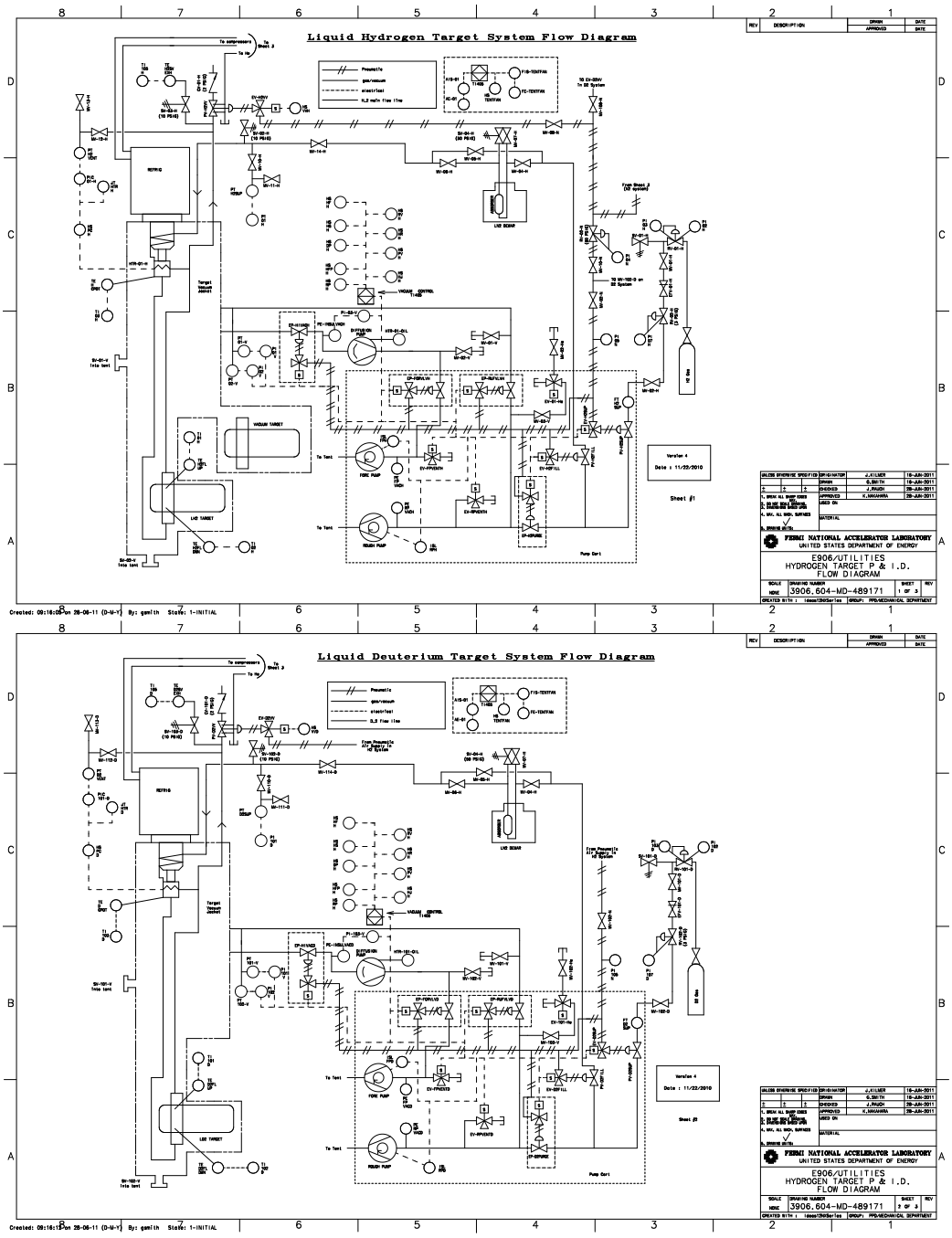

Figure 2.9: **Liquid Target Equipment Flow Diagram.** Planning documents for the liquid hydrogen isotope apparatuses are displayed here. The first document (top) describes the liquid protium apparatus and the second document (bottom) describes the liquid deuterium apparatus. Of particular importance is the pump cart, which houses the secondary pumps for rough vacuum, the target vacuum jacket, which insulates the targets from conductive heat transfer to open air through the use of a diffusion pump, the refrigerator and cold head, the liquid target flask, and the gas delivery system. The protium target differs slightly from the deuterium target in that it includes the empty flask in its insulation vacuum chamber.

CHAPTER III

Analysis

The ultimate goal of this analysis is to qualitatively and quantitatively examine the transverse momentum and angular distributions of dimuon yields from the E906/SeaQuest spectrometer. Information about the relative magnitude of non-perturbative parton dynamics can be gained from qualitative comparison of dimuon transverse momentum to signal Monte Carlo and the extraction of various angular modulation coefficients: λ, μ, and ν with a fourth scaling parameter, κ, (added for completeness and fitting purpose), from the angular distribution of target Drell-Yan dimuons in the Collins-Soper frame. Unless otherwise qualified, all angular variables referenced in this analysis are Collins-Soper angular variables, with Collins-Soper θ measuring the angle of muon motion with respect to the beam axis and Collins-Soper ϕ measuring the difference of orientation of the dimuon plane and the assumed quark-antiquark interaction plane.

To transform from the laboratory frame to the Collins-Soper frame, two transformations are necessary. First a boost along the beam direction to the interaction center-of-mass frame sets the z-momentum of the virtual photon to zero and a boost along the remaining transverse momenta sets the muon pair back-to-back. The effect of this transformation is the distribution of any final state transverse momentum back to the initial hadrons, which roughly approximate average quark motion. Both

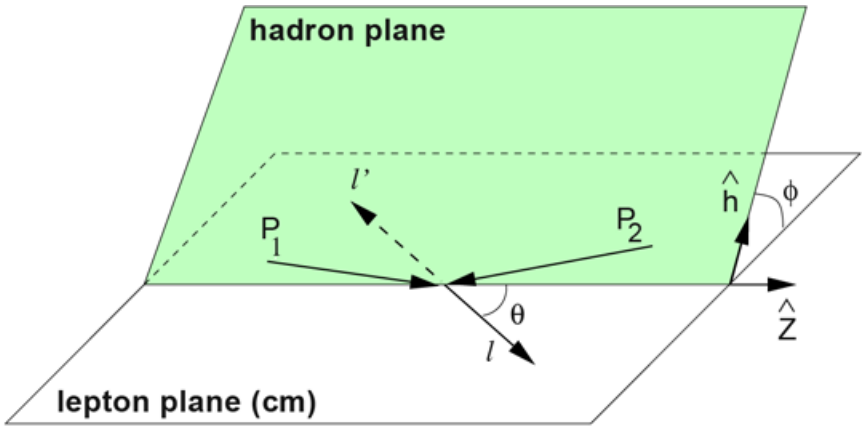

Figure 3.1: **An Illustration of the Collins-Soper Frame.** In this figure the proton beam is aligned with the z-axis, P_1 and P_2 are the momenta of the hadrons with assumed transverse momentum, and l and l' are the momenta of the resulting leptons. This means the azimuthal angle measures the angular difference between the hadron and lepton planes and the polar angle defines the angular difference between the leptons and the beam/z-axis.

transformations can be applied in a succinct manner using the following equations for laboratory variables:

$$\begin{aligned} \theta &= \cos^{-1}\left(\frac{2(l_1^+ l_2^- - l_1^- l_2^+)}{Q\sqrt{(Q^2+Q_T^2)}}\right), \\ \phi &= \tan^{-1}\left(\frac{\sqrt{Q^2+Q_T^2}}{Q}\frac{\Delta_T\cdot\hat{R}_T}{\Delta_T\cdot\hat{Q}_T}\right), \end{aligned} \tag{3.1}$$

where

$$\begin{aligned} l^{\pm} &= \frac{l^0 \pm l_z}{\sqrt{2}} \\ Q &= l_1 + l_2, \qquad \Delta = l_1 - l_2, \\ \hat{R} &= \frac{P_A \times Q}{|P_A \times Q|}, \qquad \hat{Q}_T = \frac{Q_T}{|Q_T|}, \end{aligned} \tag{3.2}$$

l is the lepton momentum vector and P_A is the momentum vector of the accelerated hadron [97]. An illustration of the Collins-Soper frame is shown in Figure 3.1[98].

The analysis was conducted in a modular fashion, meaning at any given time any

of the major pieces could be updated and reapplied allowing for fast updating. Major pieces of the analysis were combined wherever possible. In the simplest interpretation, this analysis is the task of evaluating the following equation three different times for $X = \theta$, $X = \phi$, and $X = p_T$:

$$\begin{aligned} N^{q\bar{q}\to l\bar{l}}_{Est.,i}(X) &= \int_{T_i}\int_{10^3}^{10^5}\left[\frac{N_{Meas.,i}(\mathcal{I}_i(t),X)}{\Gamma(X)\cdot\epsilon_i(\mathcal{I}_i(t),X)}\right]d\mathcal{I}_i(t)dt, \\ &\approx \sum_{T_i}\sum_{10^3}^{10^5}\left[\frac{N_{Meas.,i}(\mathcal{I}_i(t),X)}{\Gamma(X)\cdot\epsilon_i(\mathcal{I}_i(t),X)}\right]\Delta\mathcal{I}_i(t)\Delta t, \end{aligned} \tag{3.3}$$

where $N^{q\bar{q}\to l\bar{l}}_{Est.,i}(X)$ is the estimated event yield as a function of the dimuon observable, X, from the target with the "ith" nuclear species, $N_{Meas.,i}(\mathcal{I}_i(t),X)$ is the measured event yield as a function of, $\mathcal{I}_i(t)$, the proton intensity on the given target as a function of time and the dimuon observable, $\Gamma(X)$ is the spectrometer acceptance as a function of dimuon observable, $\epsilon_i(\mathcal{I}_i(t),X)$ is the efficiency of the reconstruction process as a function of the proton intensity and dimuon observable, and T_i is the total time over which beam was taken on each target. The resolution of pulse occupancy, $\Delta\mathcal{I}_i(t)$, is 1000 protons per event and the time resolution is on the order of the interval between pulses which equates to 19 nanoseconds per event. The pulse size occupancy interval is 10^3 to 10^5 protons. Equation 3.3 gives a natural conceptual framework to the task of extracting any dimuon observable which can be broken into three major parts: a proper evaluation of spectrometer acceptance $\Gamma(X)$, an evaluation of event reconstruction efficiency, $\epsilon_i(\mathcal{I}_i(t),X)$, and an evaluation of the measured sample, $N_{Meas.,i}(\mathcal{I}_i(t),X)$ which will include some consideration of the variation in incident particle flux.

3.1 Spectrometer Acceptance

The evaluation of spectrometer acceptance $\Gamma(X)$ can be broken into multiple parts corresponding with the variables in the following equation:

$$\Gamma(X) = \frac{\sigma_{MC}^{Geom.}(X)}{\sigma_{MC}^{q\bar{q}\to l\bar{l}}(X)} \cdot \frac{\sigma_{MC}^{Trig.}(X)}{\sigma_{MC}^{Geom.}(X)} \cdot \frac{\sigma_{MC}^{Recon.}(X)}{\sigma_{MC}^{Trig.}(X)} = \frac{\sigma_{MC}^{Recon.}(X)}{\sigma_{MC}^{q\bar{q}\to l\bar{l}}(X)}, \tag{3.4}$$

where σ is the simulated cross section. Every term in the equation above can be evaluated using only track reconstruction and simulation however, reconstructed particle trajectories from collected data are used when necessary.

3.1.1 Generalized Geometric Acceptance

In most high-energy nuclear and particle physics experiments acceptance corrections are derived purely from Monte Carlo distributions however, a cursory look at an idealized analytical representation of the the spectrometer yields significant insight into how relevant space observables are distorted. This analysis begins with the intersection of a volume in spherical coordinates and a plane normal to a ray whose origin is also the origin of the spherical volume. The ray serves as a representation of the beam axis as well as an orienting and normal vector for the spherical volume and plane, which is a simplified representation of the spatial distribution of the spectrometer. In Cartesian coordinates, this would align the ray with the z-axis along the Cartesian vector $(0, 0, 1)$ and in spherical coordinates, the ray would be aligned with the spherical vector $(1, 0, 0)$. It can be reasoned that even if the process in question does not have an isotropic distribution over constant spherical surface, its specific deformation can be implemented as a coordinate transform and projected onto the spherical surface.

Assume that the initial frame of interaction is the laboratory frame. Both geo-

metric solids have simple forms in a three-dimensional Cartesian coordinate system:

$$ax^2 + by^2 + cz^2 = d^2, \tag{3.5}$$

$$ex + fy + gz = h, \tag{3.6}$$

with the first equation describing a generalized ellipsoid, and the second, a generalized plane. Forcing the generalized plane to be perpendicular to the beam axis (i.e. $e \to 0$, $f \to 0$) and substituting z in equation 3.5 for the simplified version of equation 3.6 yields a general equation for the intersection of the plane and ellipsoid, which defines a conic section:

$$ax^2 + by^2 + \frac{ch^2}{g^2} - d^2 = 0. \tag{3.7}$$

A point of clarity: to calculate a particle flux through the area defined by the conic section it would be necessary to integrate the interior of the volume which means that the intersection of the surface and volume defines only a boundary of the particle flux. Converting to spherical coordinates ($x \to \rho \sin\theta \cos\phi$, $y \to \rho \sin\theta \sin\phi$) yields the general equation in spherical coordinates.

$$\rho \sin^2\theta \left[a \cos^2\phi + b \sin^2\phi\right] + \left(\frac{ch^2}{g^2} - d^2\right) = 0. \tag{3.8}$$

In order to better implement the physical limits of the detector, constraints must be implemented on the general equation. The first constraint could emphasize that the source and detecting plane are not collocated. This can be done by examining the individual contributions of each direction of the Jacobian for the spherical system with relation to the Cartesian coordinate system. For the z-direction the contribution is $z = \rho \cos(\theta)$. Assuming the plane is some fixed distance from the source, κ, and

rearranging the z-direction Jacobian yields:

$$\theta(\rho) = \cos^{-1}\left(\frac{\kappa}{\rho}\right), \tag{3.9}$$

which fixes the angle of any part of the intersection to ρ. Until the geometric scale of the plane is implemented in equation 3.8, the perpendicular plane is infinite and should demonstrate very specific behavior at extremes. If $\rho < \kappa$, $\cos^{-1}(\frac{\kappa}{\rho})$ becomes imaginary and as $\rho \to \infty$, $\cos^{-1}(\frac{\kappa}{\rho}) \to \frac{\pi}{2}$ indicating that the domain and range of equation 3.9 is $[\kappa, \infty)$ and $[0, \frac{\pi}{2}]$ however the flux through the area defined by the intersection,

$$\int_{\kappa}^{\infty} \cos^{-1}(\frac{\kappa}{\rho}) d\rho = \rho \cos^{-1}(\frac{\kappa}{\rho}) - \frac{\kappa\sqrt{-\kappa^2+\rho^2}\log\left(\rho+\sqrt{-\kappa^2+\rho^2}\right)}{\sqrt{\rho^2-\kappa^2}}\Bigg|_{\kappa}^{\infty}, \tag{3.10}$$

diverges in both directions.

To implement limits on the plane, an equation which gives a square in polar coordinates:

$$r(\phi) = \frac{1}{|\alpha\cos(\phi)+\beta\sin(\phi)| + |\alpha\cos(\phi)-\beta\sin(\phi)|}, \tag{3.11}$$

can be adapted to spherical coordinates:

$$\Theta(\phi) = \tan^{-1}(\sqrt{\frac{|\alpha\cos(\phi)+\beta\sin(\phi)| + |\alpha\cos(\phi)-\beta\sin(\phi)|}{\kappa}}). \tag{3.12}$$

where α and β define the physical limits of the spectrometer in the intersecting plane.

Rearranging equation 3.9 and substituting equation 3.12 for a free θ parameter in the general equation gives the ϕ equation:

$$\begin{gathered}(|\alpha\cos(\phi)+\beta\sin(\phi)| + |\alpha\cos(\phi)-\beta\sin(\phi)|) \\ [a\cos^2(\phi)+b\sin^2(\phi)] + (\frac{ch^2}{g^2} - d^2) = 0.\end{gathered} \tag{3.13}$$

The constants α and β can be varied to capture the effects of specific plane lengths and a and b represent various changes in the source distributions on the overall acceptance in ϕ.

The final piece of the analysis for ϕ concerns simulation of the effects of the SeaQuest focusing magnet in the lab frame. Referring again to the Jacobian of the spherical coordinate system with reference to the Cartesian coordinate system (ie $x = \rho\sin(\theta)\cos(\phi)$ and $y = \rho\sin(\theta)\sin(\phi)$) the general effect of the magnet can be simulated by adjusting the values of a and b or α and β relative to each other, with a reduction in the magnitude of $a(\alpha)$ relative to $b(\beta)$ representing a shrinking of the acceptance in the associated cartesian coordinate direction or an expansion in the opposite direction. Qualitative results for laboratory ϕ, show a deformation to a $\cos^2\phi$ modulation for single muons. Qualitative results for the azimuthal angle, which can be interpreted as a periodic sum of two points randomly chosen on the single muon curve, show a deformation to a $\sin^2\phi$ modulation. Both are shown in Figure 3.2.

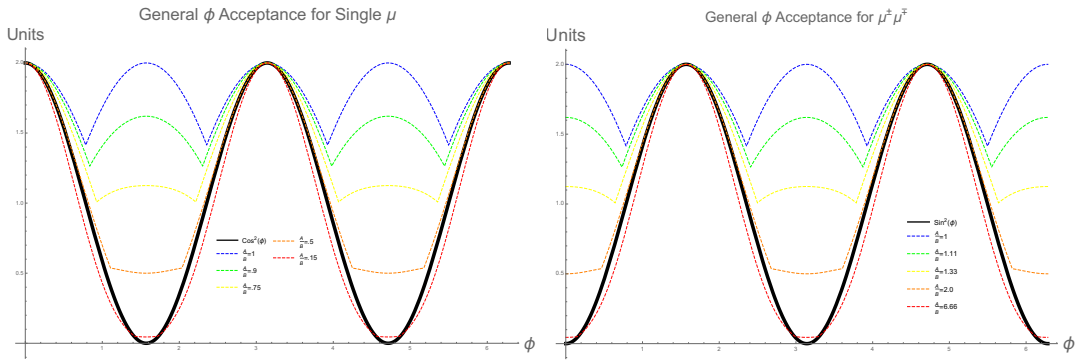

Figure 3.2: **E906/SeaQuest spectrometer ϕ acceptance distortion.** On the left is a model of the relative single muon distribution in laboratory ϕ produced by the relative physical limits of the detector for single muons. When magnet effects are implemented by changing the ratio of A to B the idealized acceptance reduces to a simple trignometric function. On the right is the distribution in the azimuthal angle produced by the limits of the detector for dimuons with the reduction in magnet effects coming from a shift in phase due to the adding of two single muons.

The acceptance modulation for single muons in laboratory θ is dependent on a ratio of transverse momentum to longitudinal momentum, which is limited by the transverse coverage of the detector. Given the fowardness of the interaction, the longitudinal momentum dominates, with assumed exponential decay in transverse momentum dominating falloff from the forward beam direction. Qualitative results for dimuons in the Collins-Soper frame benefit from a boost first to the center-of-mass frame, and then to a frame where outgoing leptons are back-to-back distributing transverse momentum evenly between the two. This results in a relatively simple relationship which can be read off from equation 3.8 as a $\sin^2\theta$ modulation. This relationship and possible effect on theoretical dimuon distributions as well as its sensitivity to acceptance edges is shown in Figure 3.3.

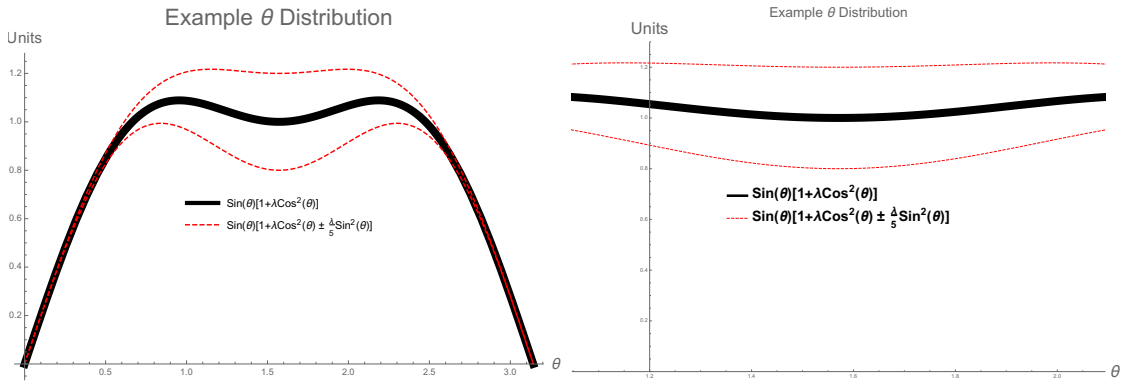

Figure 3.3: **E906/SeaQuest spectrometer polar acceptance distortion.** The plot of the left shows a theoretical model of relative dimuon cross section distribution in the polar angle (black solid line) with an assumed polarization of 1 ($\lambda = 1$). The dashed red lines represent distortions of the underlying distribution by the detector of 20%. The plot of the right is the same as the plot on the left but shows as detector acceptance shrinks in the polar angle (where here the interval is $[\cos^{-1}(0.5),\cos^{-1}(-0.5)]$), distinguishing between any of the lines in normalized samples becomes difficult.

3.1.2 Geometric Acceptance for Single Muons

Before considering the geometric acceptance of a particle pair, it is necessary to examine the behavior of single muons in the spectrometer. Given that it is impossible to do a single muon analysis in the Collins-Soper frame consideration of single muon acceptance in laboratory frame is a reasonable analog. Simulated angular behavior from target Drell-Yan Monte Carlo qualitatively agree with the analysis in the previous section.

To compare to real data, reconstructed muon trajectories from the pseudo random NIM 3 "Minimum Bias" trigger were used, however the abundance of contributing physics processes as well as imperfections in the detector distort behavior which would otherwise be well described by the analytical model. An exponential decay function describes the transverse momentum distribution between a certain range of momenta but at high values, acceptance and inefficiency of reconstruction lead to unreliable counts. In the lower bins, reconstruction cuts, a change in physics regimes, and reconstruction inefficiency all affect beam occupancy. Laboratory θ shows the same relation to transverse momentum as the simulated muon trajectories and also decays exponentially with similar measurement limits. Laboratory ϕ loosely resembles the trigonometric functions derived analytically however the addition of a pedestal implies significant background. Reconstructed acceptance for single muons is shown in Figures 3.4 and 3.5.

The most striking differences between the Drell-Yan simulations and pseudo random spectrometer response are two asymmetries, one in true incident beam position and the other in relative charge yields, both of which artificially induce modulations in the angular distributions of single and dimuon pairs. Evidence for the difference in charged yields can be inferred from Figure 3.4, but is explicitly shown in wire chamber element response distribtions in the Appendix. The asymmetry in charge yields is explained by the charge of the initial state nucleons and is partially corrected by

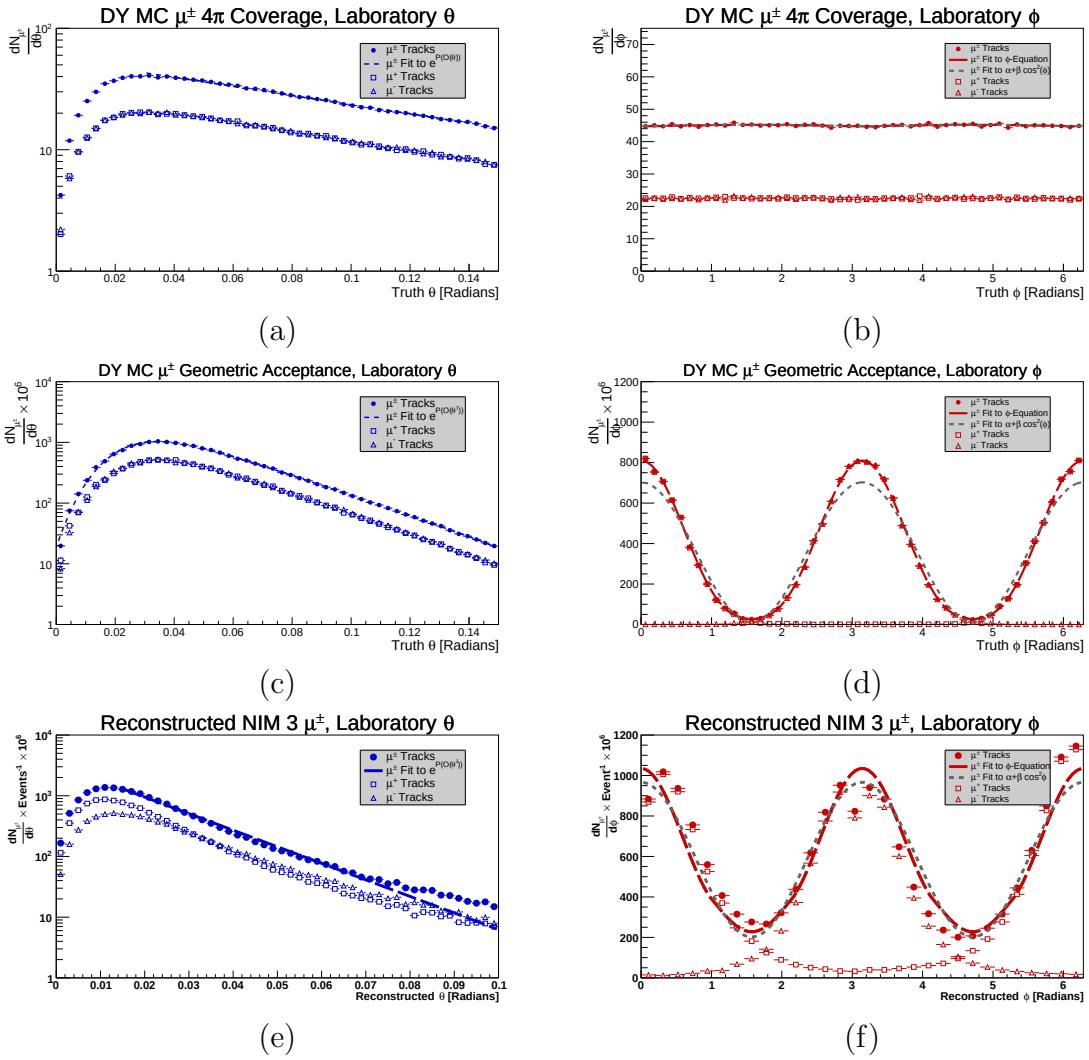

Figure 3.4: **Single Muon Angular Acceptance.** Graphs (a) and (b) show the default angular distributions of single muon tracks in Drell-Yan simulations. Graphs (c) and (d) show the portion of those distributions accepted in the E906/SeaQuest spectrometer as well as fits to the simplified and full angular modulations suggested by the *ab initio* analysis. Graphs (e) and (f) show the angular distributions of muon trajectories reconstructed from data collected with the minimum-bias trigger. Both distributions show an abundance of positive muons relative to negative muons.

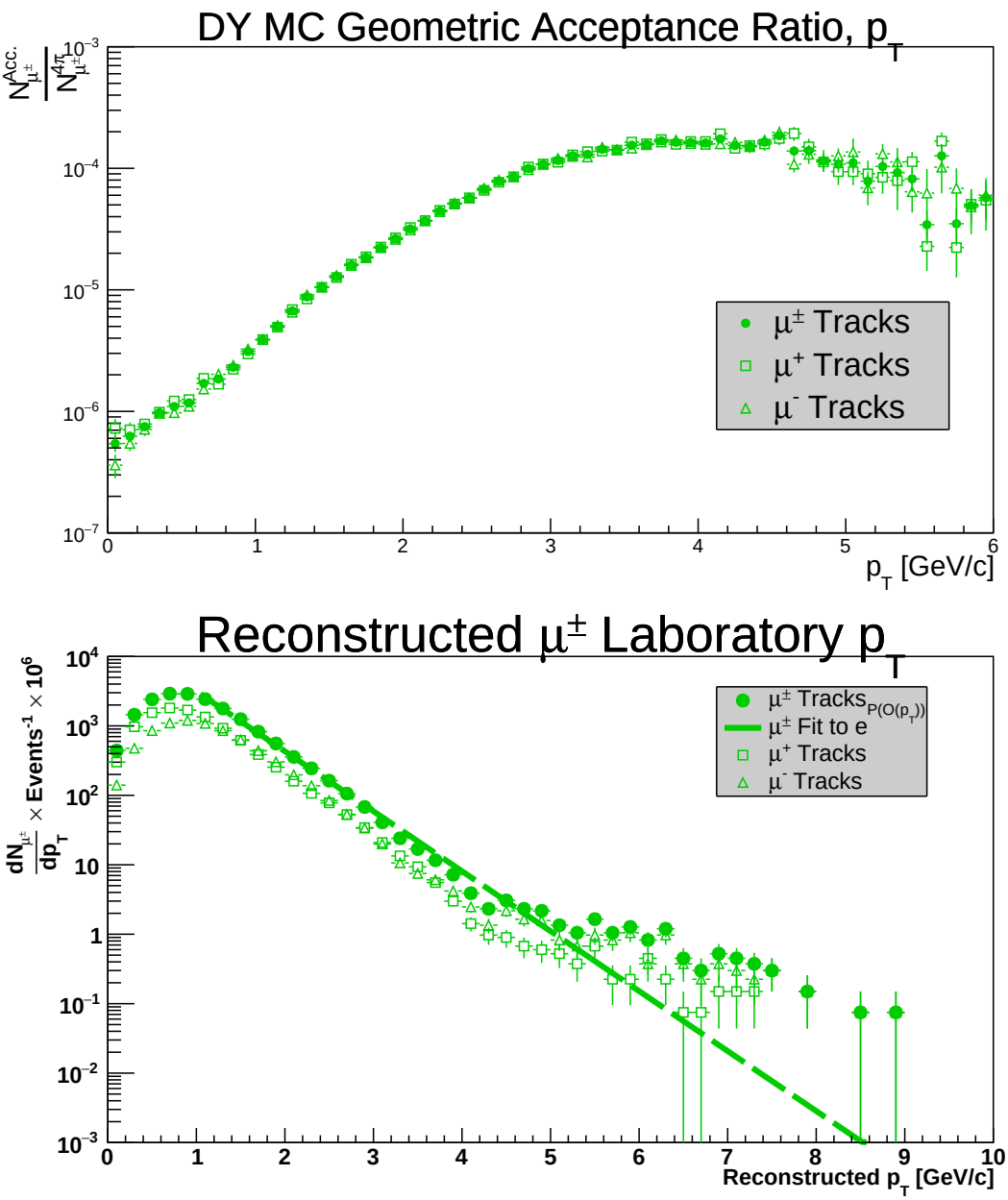

Figure 3.5: **Single Muon Transverse Momentum Acceptance.** The top graph shows the ratio of muons accepted in the E906/SeaQuest spectrometer as a function of transverse momentum. This was done because transverse momentum distributions in the Drell-Yan Monte Carlo do not accurately represent Drell-Yan transverse momentum yields. The bottom graph shows the yield of single muons per event as a function of transverse momentum. An abundance of positive tracks exists below $p_T < 1.0$.

the physics triggers and trackers with the remaining corrections applied in analysis. The trigger requires a pair of single muons from either side of the detector, improving the probability of collecting charged pairs for physics analysis, and the tracker only declares muons of opposite signs as signal dimuons. The error in true incident beam position was estimated by examining the offset of the initial transverse position of reconstructed tracks from the NIM3 trigger, the details of which are discussed in the following section.

Finally, the NIM 3 trigger demonstrates unequivocally that geometric element activation increases with intensity which shows in Figure 3.6 that the response of the detector to produced muons (including reconstructed particle yield) is acutely dependent on beam intensity.

3.1.2.1 Incident Beam Position and Angle

True incident beam position can be estimated using the NIM3 "Minimum Bias" Trigger as shown in Table 3.2 however, without a detailed separation of reconstructed muons produced in the target from those in the dump it is difficult to estimate whether reconstruction with either constraint (i.e. target or dump z-position) is appropriate. An examination of the reconstructed position for all tracks reconstructed in the NIM3 data sample of Roadset 67 save for quality cuts (as shown in Figure 3.7, suggests reconstructed muon path fits to the dump are more precise than fits of those same reconstructed muon paths to the target however, it is still unclear whether fits using muon paths reconstructed with a target z-position constraint are an accurate measure of the offset at the target or not.

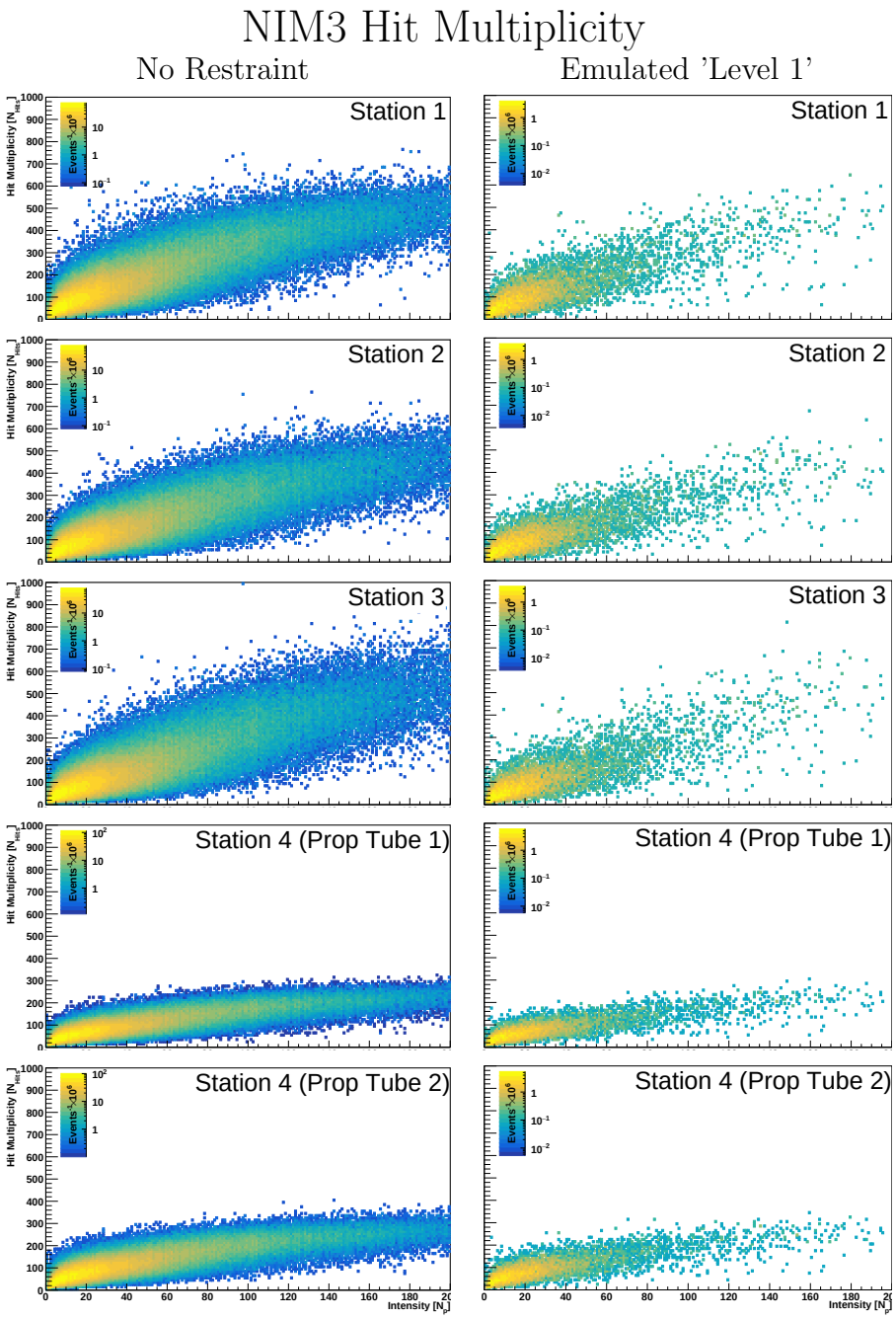

Figure 3.6: **Hit Multiplicity.** The E906/SeaQuest spectrometer has a clear multiplicity dependence that is not affected by the 'Level 1' trigger emulation restraint. The response of the detector falls off from ideal below 10,000 protons per pulse (ppp) indicating that some form of pile-up affects almost all collected data.

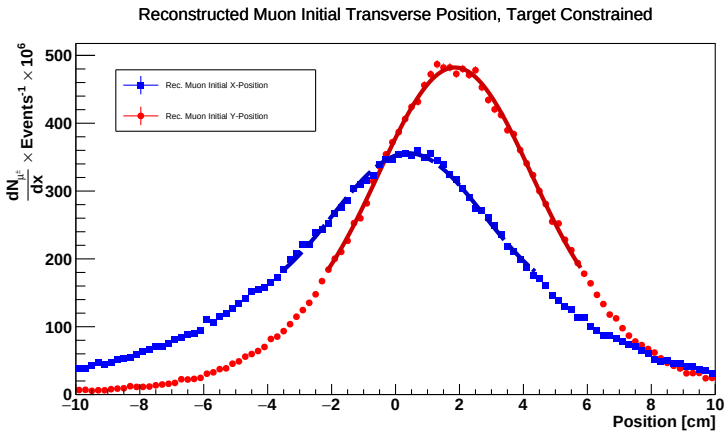

(a)

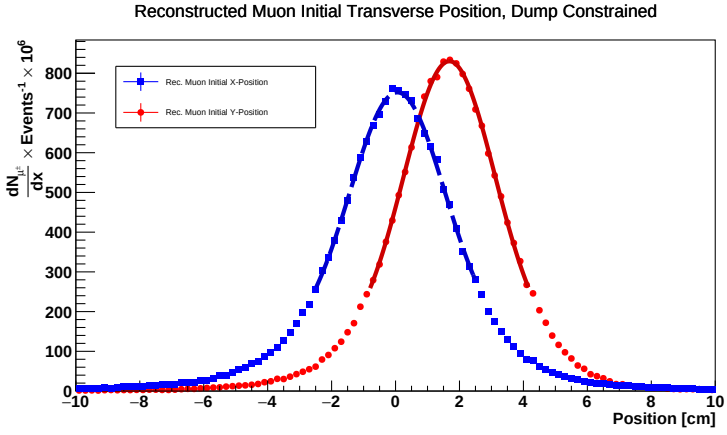

(b)

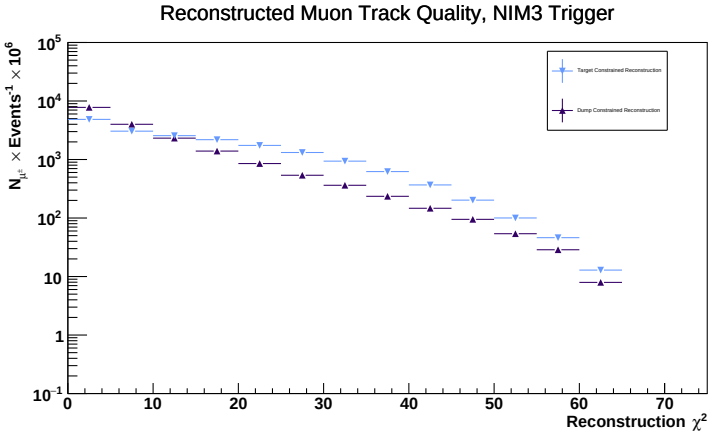

(c)

Figure 3.7: **Initial Beam Position Estimates.**(a) Muons from the NIM3 trigger reconstructed with an initial z-position in the target (-129.54 cm absolute z-position) (b) Muons from the NIM3 trigger reconstructed with an initial z-position in the beam dump (42 cm absolute z-position) (c) The χ^2 'goodness-of-fit' measure of reconstructed muon trajectories.

If the procedure for traceback through the beam dump to the target can be assumed to be a good estimator, a true target incident beam position would be 1.69 ± 0.01 cm in the y-direction and 0.5 ± 0.01 cm in the x-direction. To remain consistent with dump values, a nonzero beam angle on the order of milliradians would be added to simulations with the magnitude of each offset measured by the difference between the target and dump values. Differences show an angle of 1.1 ± 0.1 mr in the y-direction and 2.1 ± 0.1 mr in the x-direction, which have a negligible effect on reconstructed particle momenta and can thus be set to zero. This also indicates the differences between target and dump transverse position are negligible.

NIM3 Based Incident Beam Position Estimate								
Sample	Figure	z-Position (cm)	χ^2/NDF	Mean (cm)	StdDev (cm)	Scale ($N_{\mu^\pm}$)	Pedestal ($N_{\mu^\pm}$)	Fit Interval (cm)
x-Position	3.7a	42	$33.79/21 \approx 1.61$	0.05 ± 0.01	1.49 ± 0.03	640.4 ± 13.93	111.6 ± 15.13	[-2.5,2.5]
y-Position	3.7a	42	$23.97/21 \approx 1.14$	1.69 ± 0.01	1.43 ± 0.03	733.0 ± 13.11	97.41 ± 14.40	[-0.82,4.18]
x-Position	3.7b	-129.42	$43.86/36 \approx 1.22$	0.40 ± 0.01	2.36 ± 0.09	230.3 ± 9.08	127.6 ± 9.82	[-3.6,4.4]
y-Position	3.7b	-129.42	$62.40/36 \approx 1.73$	1.87 ± 0.01	2.37 ± 0.06	398.6 ± 9.73	95.09 ± 10.54	[-2.17,5.83]

Table 3.1: **Initial Beam Position Estimate Fits.** All uncertainties shown are statistical. Systematic uncertainties on these fits are estimated to be 0.1 centimeter through comparison with other collaboration estimates. The fits show a clear difference between target constrained and dump constrained fits as well as fits of reconstructed muons with or without a 'Level 1' emulation requirement.

3.1.3 Geometric Acceptance for Dimuons

Now that base geometric detector response has been examined, acceptance for dimuons can be evaluated using simulations. The results of those simulations with and without the existence of the E906/SeaQuest spectrometer is shown in Figure 3.8. A $\sin^2\phi$ modulation is visible in the simulated dimuon yield indicating that the geometric acceptance of the dimuon pair is almost directly predicted by the above *ab initio* analysis. Through the use of simple trigonometric identities it can be shown that the spectrometer induced $\sin^2\phi$ (or $\cos^2\phi$) modulation is congruent with the $\cos 2\phi$ modulation. When examining geometric acceptance effects, detector distortion in ϕ manifest as an induced negative value for ν. An example of how the induced

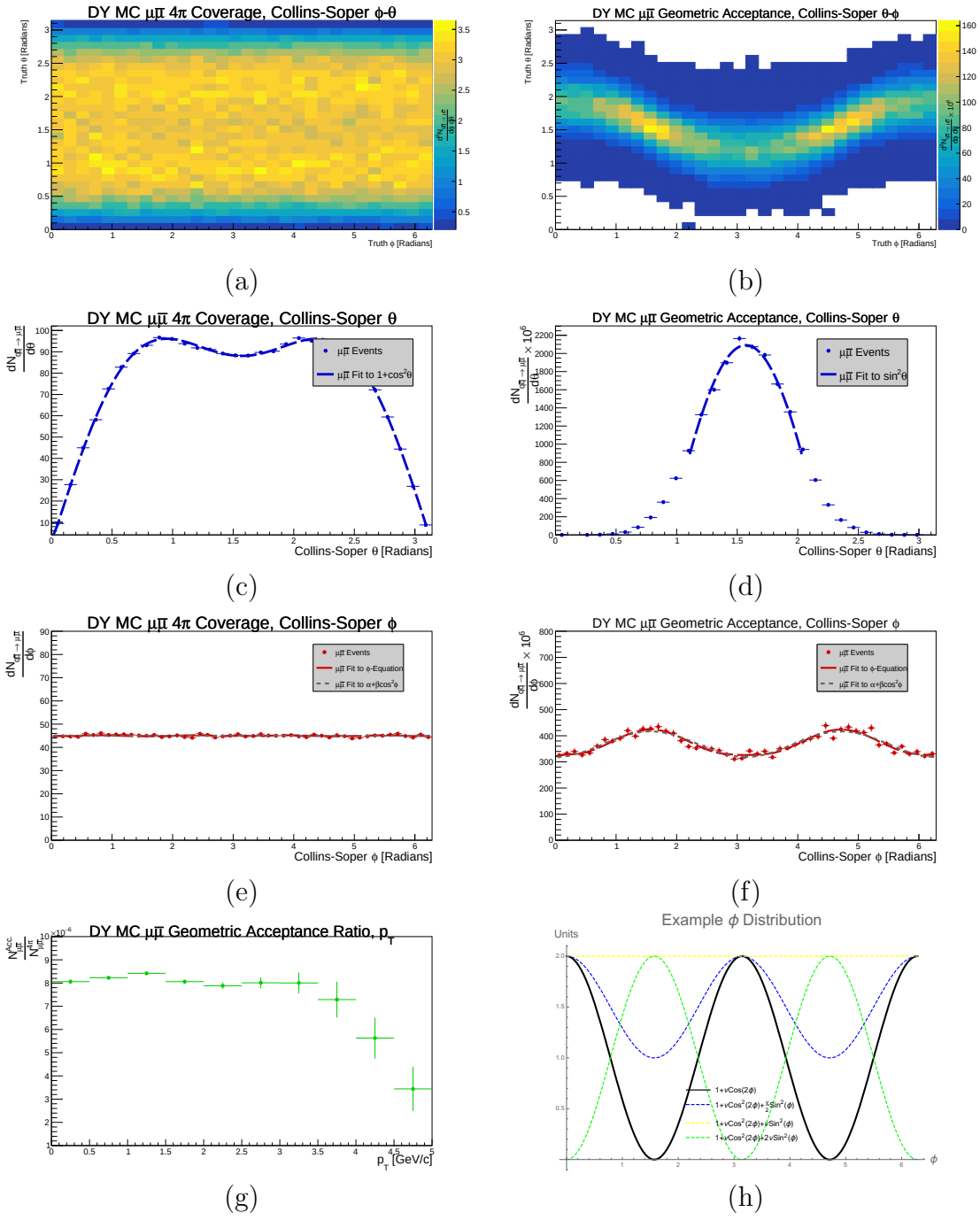

Figure 3.8: **Dimuon Angular & Transverse Momentum Acceptance.** The two dimensional angular distributions of Drell-Yan with and without spectrometer constraints are shown in (a) and (b). Full coverage over the entire angular range was not expected, but the angular correlations or "mixing" add complication to the analysis. Mixing is not apparent in one dimensional projections of the polar angle (c) and (d) or the azimuthal angle (e) and (f). The ratio of accepted dimuons as a function of transverse momentum is shown in (g). How the induced spectrometer modulations affects the extraction of ν-modulation is shown in (h).

detector modulation could affect extracted results is shown in Figure 3.8(h).

No physical detector can have perfect coverage and due to its fixed-target nature, SeaQuest was expected to cover relatively little of the total process solid angle, however the focusing magnet introduces features unique to SeaQuest. First, the spectrometer has limited coverage in angular space, motivating large fiducial cuts in the polar angle when extracting the magnitude of angular modulations. Second, a considerable correlation of the azimuthal and polar angles occurs in intermediate ϕ range, indicating that the E906/SeaQuest spectrometer introduces a mixed term modulation which may function as a method to quantify the quality of fits and acceptance corrections.

3.1.4 Trigger Acceptance

The SeaQuest trigger is physically implemented through the vertical hodoscope planes at all four of the measurement stations. All spectrometer trigger configurations available for use are listed in Table 3.2, with particular emphasis on the MATRIX/FPGA1 trigger as the one used to collect the dimuon sample used in this physics analysis. MATRIX/FPGA2 has the potential for providing a significant boost in the number of high-mass Drell-Yan events but it was heavily prescaled for this run period and will not be used.

Trigger	Type	Quadrants	Description
MATRIX/FPGA1	Software	1 & 4 or 2 & 3	Physics: Level 1: Roadset 67, Level 2: Top-Bottom and Bottom-Top
MATRIX/FPGA2	Software	1 & 2 or 3 & 4	Physics: Level 1: Roadset 67, Level 2: Top-Top and Bottom-Bottom
MATRIX/FPGA3	Software	1 & 3 or 2 & 4	Diagnostics Background: Level 1: Roadsets 67, Level 2: East-East and West-West
MATRIX/FPGA4	Software	1 or 2 or 3 or 4	Singles Background: Level 1: Roadsets 67, Level 2: Top or Bottom or East or West
MATRIX/FPGA5	Software	1 or 2 or 3 or 4	Singles Background with Transverse Momentum Cut: Level 1: Roadsets 67, Level 2: Top or Bottom or East or West
NIM1	Hardware	N/A	Horizontal Diagnostics: One y-hodoscope element from each station + Top-Bottom and Bottom-Top
NIM2	Hardware	N/A	Vertical Diagnostics: One y-hodoscope element from each station + Top-Bottom and Bottom-Top
NIM3	Hardware	N/A	Minimum-Bias: Beating of beam clock with prime number.
NIM4	Hardware	N/A	Independent Intensity: 4 × target upstream particle counter. Scales with intensity.
NIM5	Hardware	N/A	Flush: End-of-spill read-out buffer flush.

Table 3.2: Summary of all available triggers for E906/SeaQuest.

In privileging high-mass Drell-Yan, the laboratory x-direction was chosen to provide greater sensitivity in the bend plane of the focusing and analysis magnets but this constraint significantly alters the geometric acceptance of the detector. It could

be argued that a trigger relying on input from both vertical and horizontal hodoscopes at each of the four stations would be more efficient in selecting Drell-Yan events but sample statistics would suffer with a more strict coincidence condition.

3.1.4.1 Level 1 of The MATRIX/FPGA1 'Dimuon' Trigger: 'Roads' and Quadrant Activation

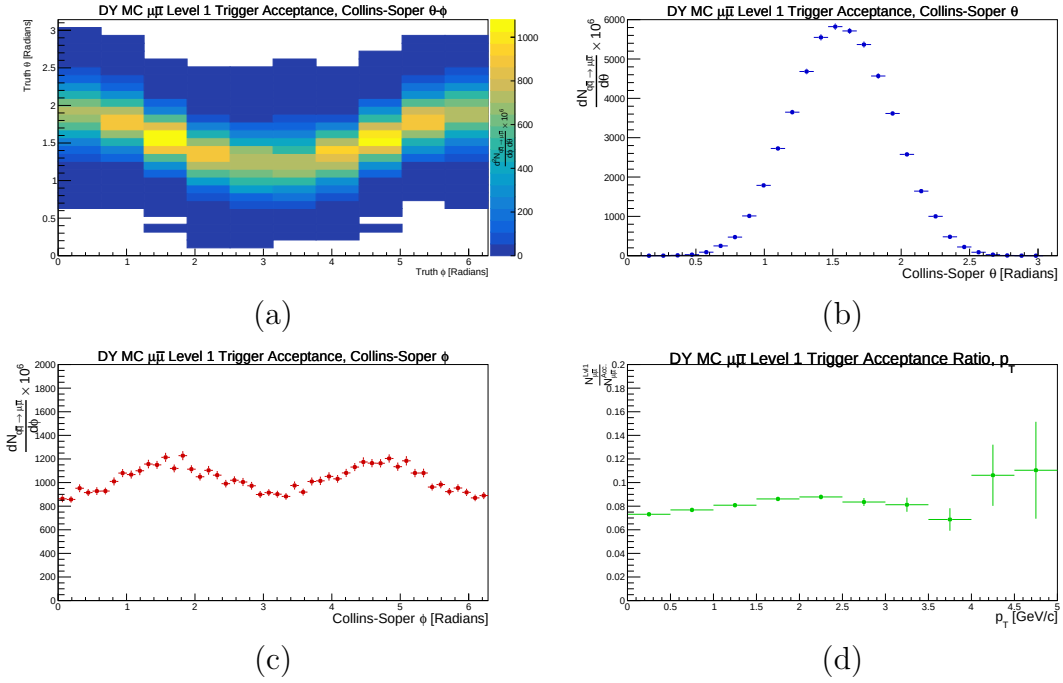

Figure 3.9: **Level 1 Trigger Dimuon Angular & Transverse Momentum Acceptance.** Part (a) is a two dimensional representation of the trigger acceptance in the azimuthal angle and θ after the first level of the dimuon trigger. Parts (b) and (c) are projections of the two dimensional plot into one dimensional polar and azimuth distributions. Part (d) shows how the first level of trigger acceptance changes as a function of transverse momentum.

The first level of the physics trigger is implemented through a coincidence of single vertical hodoscope elements from each of the trigger stations called a 'road'and divided into four quadrants in the laboratory azimuth which is oriented around the beam line. The set of roads, which function as a discrete look-up table, was determined

using Drell-Yan signal Monte Carlo and geometrically optimizes the spectrometer to record as many high-mass Drell-Yan events as possible while rejecting the most background. Drell-Yan simulation software reports a rejection factor of approximately 8.8% for this level of the trigger, indicating that of all dimuons within the spectrometer acceptance, at least one of its tracks will pass the first level of the trigger 91.2% of the time. Background rejection optimization was achieved by eliminating regions with activation rates that overwhelmed the data acquisition system (DAQ). Road dependent triggering can only be done with the Field Progammable Gate Arrays (FPGAs) making them slower, but more selective than the hardware only Nuclear Instrumentation Module (NIM) based triggers.

Level 1 changes to the geometric acceptance are relatively minor indicating that the trigger roads by themselves do not remedy the spectrometer induced modulation in either of the angular variables. This is mostly due to the particulars of selection and geometric acceptance. As shown earlier, in the azimuth, more single muons are accepted in the horizontal directions than in the polar angle, indicating that single muon pairs on either the top or bottom of the detector dominate trigger acceptance at level 1. The transverse momentum acceptance ratio remains relatively flat.

3.1.4.2 Level 2 of MATRIX/FPGA1 'Dimuon' Trigger: Opposite Quadrant Pairs

The second level of the physics trigger requires a coincidence between at least one single road from both the top and bottom halves of vertical hodoscopes in the detector. This configuration reduces the effects of magnet mixing and also reduces the dimuon pairs in the top or bottom of the detector, significantly reducing the observed azimuthal modulation induced by the spectrometer geometry. The physics trigger has a rejection factor of 54.4%, for good dimuons that enter the spectrometer and introduces a slight angular asymmetry in observed events. Transverse momentum

distributions are significantly affected making highly transverse events relatively rare.

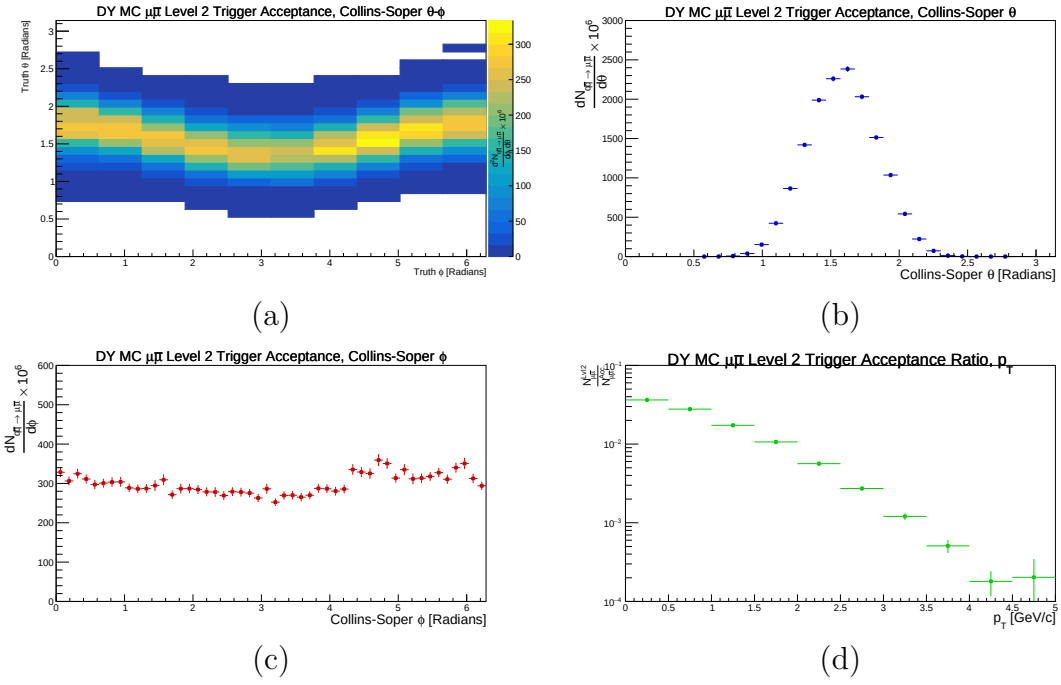

Figure 3.10: **Level 2 Dimuon Angular & Transverse Momentum Acceptance.** Part (a) shows the acceptance of the physics trigger in the polar angle and ϕ with projections of both in parts (b) and (c) respectively. The transverse momentum ratio is shown in part (d). As compared to the acceptance of the level 1 trigger, level 2 shows a large change in angular distributions, with large reductions in dimuons with high vertical momentum.

3.1.5 Event Reconstruction & Acceptance

Event reconstruction is conducted by particle trajectory reconstruction software which uses groups of "hits" or, activated channels in the drift chambers or hodoscopes along with associated timing information, to estimate the four momenta of single muons that pass through the spectrometer. Once at least two good particles are found, the software, colloquially known as kTracker, attempts to pair the tracks into a dimuon. The reconstruction process begins by applying "in-Time" and "afterpulse" cuts to all hits; removing from consideration activated channel duplicates as well as

hits which may have been produced by the beam pulse directly before or after the triggered event[1]. Next, a hodoscope "masking" cut is applied, forcing the rejection of all hits which do not spatially align with an activated hodoscope from a triggered road. The final hit level cut concerns clusters of intersections in the wire chambers which eliminates stray particle decays after the beam dump.

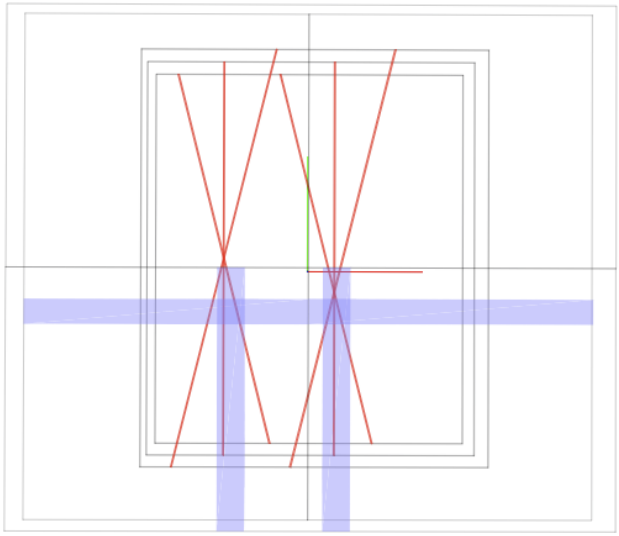

Figure 3.11: **Masked Triplets in Station 1 from Simulated Data.** The image shows multiple Hodoscope masked (blue) drift chamber triplets (red) from a pair of single muons in station 1. The green line is the vertical direction and the perpendicular red line shows the horizontal direction. This event would not satisfy the physics trigger because of its concentration on the bottom of the detector.

Once the set of hit level cuts is applied, kTracker groups the remaining activated signal wires into "triplets" for each station. Triplet groups (which are shown in Figure 3.11) must contain activated wires from at least two of the three orientations (X (vertical), U(+14° from vertical) and V(−14° from vertical)) and are defined by

[1]By comparing the length of the spectrometer ($\sim$ 25 meters) to the interval between beam pulses ($\sim$ 19 nanoseconds), it can be shown that at any given time during a spill, each station is simultaneously interacting with the products of a different pulse. $\frac{c}{19\times10^{-9}\mathrm{s}} \approx 6$ meters is the maximum distance the products of a pulse can travel before another pulse enters the spectrometer however, it is also approximately the average distance between stations.

an intersection within the plane. After all triplets have been identified, trajectory reconstruction starts when triplets at the third station are projected upstream along the beam direction into station two to form "tracklets". Any tracklet that does not intersect an activated hodoscope or points outside of the spectrometer acceptance is ignored. Once all tracklets between station two and three are found, they are projected further upstream through the open air analysis magnet toward triplets in the first station. The modest amount of transverse momentum caused by the Lorentz force in the magnet is dependent on the longitudinal momentum of the particle and is applied as a sharp bend towards station one, the magnitude of which is codified in a sagitta. Once a pair of tracklets that span the first three stations have been matched, they are projected further upstream through the iron core focusing magnet and to the target, necessitating the calculation and application of a separate sagitta incorporating the effects of multiple scattering in the iron through an iterated "magnet swim" process. Through simulation (shown in Figure 3.12) it was verified that the ratio of sagittas from the two magnets in E906/SeaQuest are relatively constant, indicating that a single bend could be applied that reasonably approximated both magnet bends simultaneously.

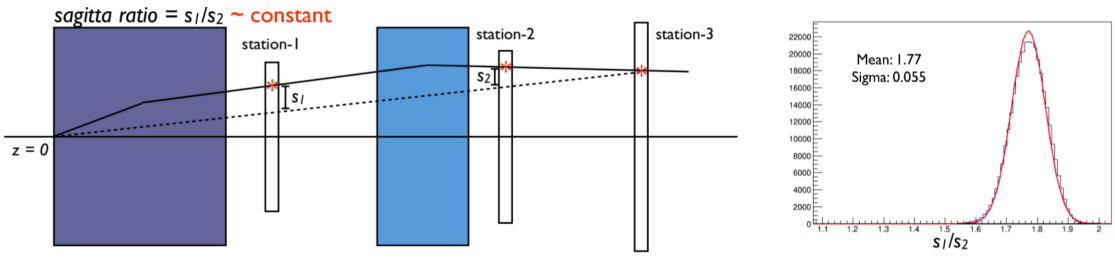

Figure 3.12: **Sagitta Ratio Verification.** The figure shows a schematic representation of the spectrometer magnet bends as well as their ratio, which is Gaussian distributed around a mean of 1.77.

If a rough calculation of the trajectory, including a feasible bend towards the target, is within three standard deviations of an approximated straight line fit to all

available triplets (including a ten by ten centimeter window centered on the beam line at the target position), a final check is made on signal from the proportional counter tubes in the fourth station to verify particle identity. Once a set of triplets passes all of those criteria it is passed to a "Kalman" fitting algorithm and a more precise path through the spectrometer is iteratively calculated along with other state vector properties at each interval point along the beam line [99]. If the Kalman fit converges, the newly minted muon trajectory is stored along with all of its hit information and state calculations at each section of the spectrometer. Pairs of single muons with similar vertices are assumed to be a pair and refit with the Kalman algorithm assuming a converging vertex. A completely reconstructed simulated dimuon pair is shown in Figure 3.13.

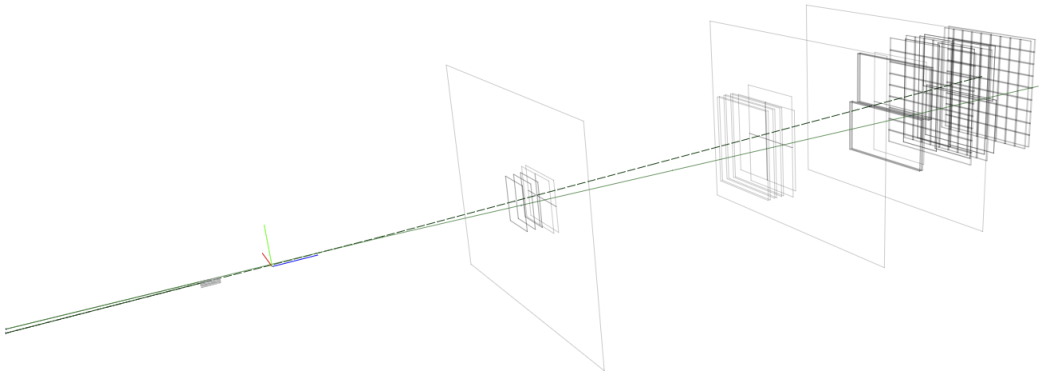

Figure 3.13: **Reconstructed Simulated Dimuon.** The two green lines are the approximate paths of reconstructed simulated muons in the first three stations. The dashed line shows the path of the muon and the solid line shows the path of the anti-muon.

kTracker appears to faithfully reproduce the fiducial limits of the spectrometer as well as the mixing in angular variables while introducing very little bias and reconstructing a dimuon in 59.1% of simulation cases. Angular acceptance is shown in Figure 3.14.

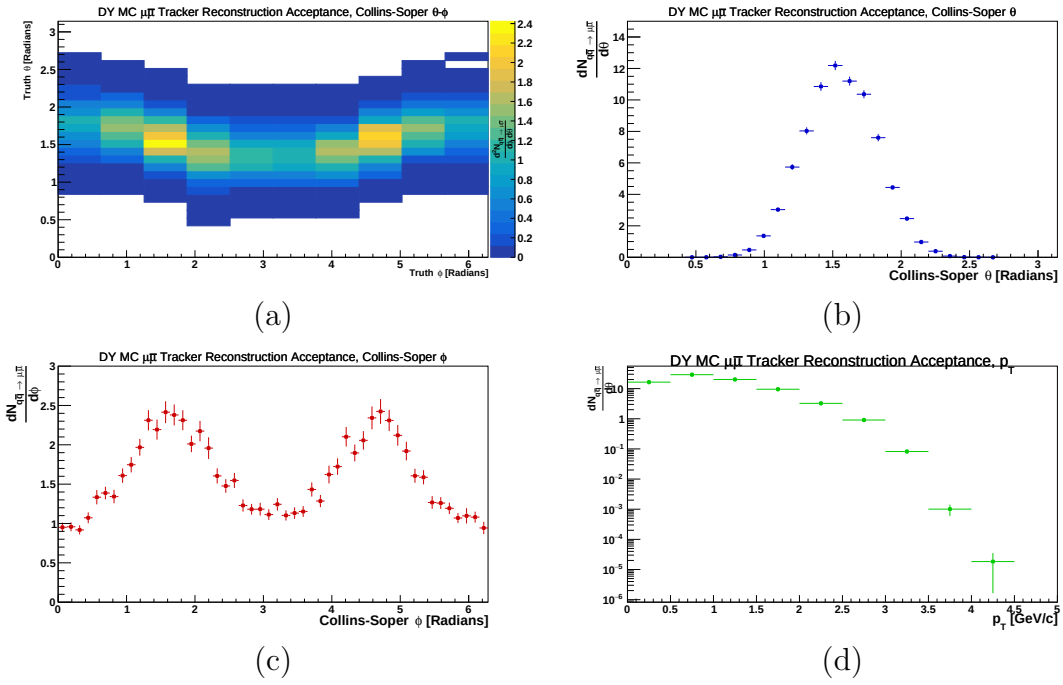

Figure 3.14: **kTracker Dimuon Angular & Transverse Momentum Acceptance.** This set of figures shows kTracker performance in accepting all muons before trigger cuts. The two dimensional angular distribution in (a) is projected into one dimensional polar and azimuth distribution in (b) and (c), respectively. Transverse momentum distributions are shown in (d).

3.1.5.1 Angular Resolution

The E906/SeaQuest spectrometer has well-defined physically determined minimum spatial resolutions but the minimum resolving power of the event reconstruction software when calculating the trajectory of single muons as well as the pairing of those muons to the same vertex are ultimately what determine the resolution of the analysis. Dimuon angular resolving power was estimated by observing the angular residual of reconstructed dimuons from Drell-Yan simulations in the Collins-Soper frame. After fitting the residuals to standard Gaussian distributions, it was found that the standard deviation of the reconstructed polar angle residual was $\Delta\theta = .023$ radians and the standard deviation of the azimuthal residual was about $\Delta\phi = .146$

radians. The standard deviation of the transverse momentum residual is $\Delta p_T = .201$ GeV/c. The residual distributions and fits are shown in 3.15. From this information,

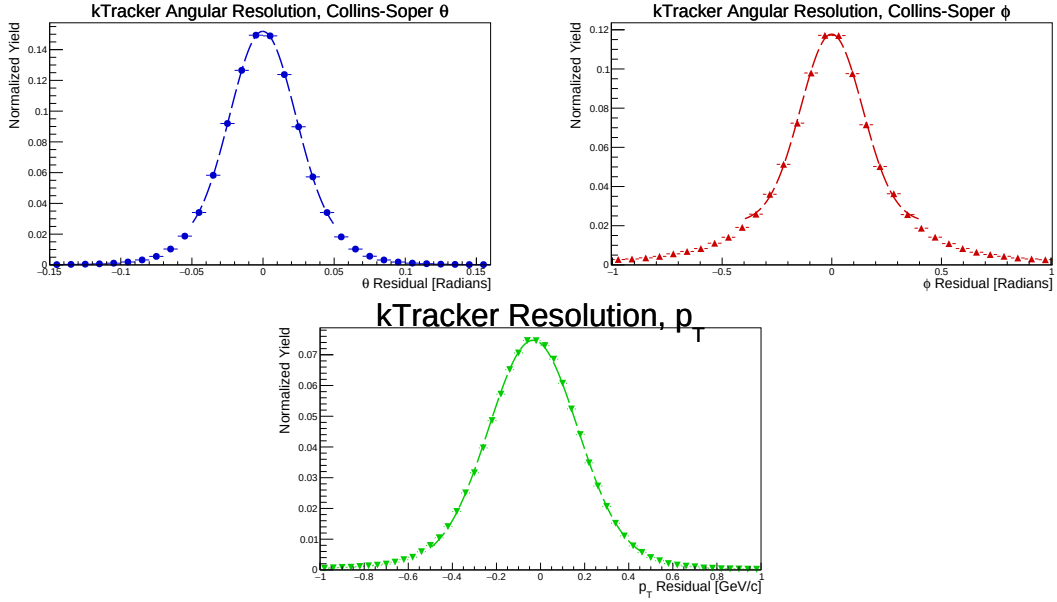

Figure 3.15: **Angular & Transverse Momentum Reconstruction Residuals.** The top graphs show the approximate Gaussian fit to the polar angle (left) and azimuthal angle (right) in the Collins-Soper frame. Both angular residuals are centered at zero down to four orders of magnitude which is well beyond the sensitivity of the track reconstruction software. The bottom graph shows an approximate Gaussian fit of the transverse momentum residual with a mean of -0.03 ± 0.0006. This slightly non-zero result is a consequence of the multiple scattering in the iron beam dump.

a bin sizing for the polar angle that encompasses 99.73% of all actual events which should occupy the bin is $\Delta\theta \times 3\sigma \times 2$ bin halves ≈ 0.14 radians, which when applied to the maximum range of the variable allows for about twenty bins. Following the same bin calculation formula would allow only eight bins in the azimuthal variable, however ten bins would each have a 2.15 residual standard deviation, containing 96.84% of all events which should occupy the bin. Finally, a one standard deviation sized bin interval in distributions of transverse momentum would be about 0.4 GeV/c in length however, the chosen bin sizing of 0.5 GeV/c is 1.24 standard deviations, including

78.5% of all events which should occupy the bin.

3.2 Event Reconstruction Efficiency

The next step in properly extracting the angular parameters is an evaluation of the event reconstruction efficiency, which can be deconstructed into multiple steps:

$$\epsilon_i(\mathcal{I}_i(t), X) = \epsilon^{Trig.}_{Data,i}(\mathcal{I}_i(t), X) \times \epsilon^{Recon.}_{Embed.,i}(\mathcal{I}_i(t), X), \tag{3.14}$$

where $\epsilon^{Trig}_{Data,i}(\mathcal{I}_i(t), X)$ is the trigger efficiency as a function of intensity and observable, and $\epsilon^{Dimuon}_{Embed.,i}(\mathcal{I}_i(t), X)$ is the event reconstruction efficiency as a function of intensity and observable. Most notable about this section of the analysis as compared to the previous section is the outer product in equation 3.14 as opposed to the inner product when examining the spectrometer acceptance in equation 3.4. The difference comes about as the consequence of two major assumptions. First, the lack of intensity dependence in the acceptance correction assumes that beam from the MI only varies in intensity, suggesting that beam profile and spatial interaction of the beam with target are constant. This assumption means that as long as the beam profile is properly defined in the simulation and placement of the beam is properly oriented with reference to the physical dimensions of the detector, spatial distributions can be effectively reproduced and evaluated as *steady state* or time independent solid angle coverage. The second assumption is that different levels of the acceptance analysis are easily separable, meaning that their effects apply predictably, linearly, and do not correlate.

Neither of these assumptions can reasonably apply to efficiency corrections, not least of which because the chance of the muon trajectory reconstruction software effectively reconstructing a given single muon or dimuon pair depends on a myriad of factors including the instantaneous global and local load of the physical measur-

ing apparatus as well as the global and local spatial distribution of signals, all of which may be correlated with the instantaneous intensity of the experiment. Many of these problems could be effectively simulated and corrected with unlimited background simulations, but simulating the E906/SeaQuest intensity through five meters of solid iron is computationally intractable. In the absence of available background simulation, clever application of data recorded using various trigger configurations were used as a substitute. To proceed, an assumption must be made that efficiency corrections between various parts of the detector are effectively separable or further analysis is effectively statistics limited.

3.2.1 Background Triggers

Design particle intensity at E906/SeaQuest is significantly beyond what can be tractably simulated, therefore it is necessary to estimate the effects of background from collected data. For this task, two different types triggers were used, one implemented through the fast acting logic gates in Nuclear Instrumentation Modules (NIM) and the other in the same Field Programmable Gate Arrays (FPGA) used for the physics trigger. Data from the two triggers were collected *in situ* with other triggers to control for variance in systematic uncertainties. Background from known processes like J/ψ and ψ' are trivial to simulate in standard particle packages thus no special trigger was needed to collect events for normalization through a mass spectrum fit.

3.2.1.1 The NIM3 'Minimum Bias' Trigger

The NIM3 trigger (defined in Table 3.2) is the third configuration of available modules that can force the DAQ system to record an event. Its triggering condition is a beating of the delivered beam frequency with a 7.5 kHz pulse signal produced by a gate generator. This trigger is designed to take a reasonable cross section of events as they interact with the detector and is treated as the foundation from which to verify

the behavior of all other triggers. The distribution of NIM3 single muon observables is shown in Figures 3.4 and 3.5. Approximately 1.3×10^7 NIM3 events were recorded in Roadset 67 and they were used as embedded background for evaluation of dimuon reconstruction efficiency under load as well as to verify efficacy of the two trigger types (i.e. FPGA versus NIM type triggers).

Due to various prescalings, not all events which would have fired multiple triggers were registered as firing those triggers, therefore emulation software was used to compare NIM3 triggered events to events recorded by other triggers. It was found that only about 1.5×10^4 satisfied the first level of the MATRIX/FPGA4 trigger (defined in Table 3.2) and 4 events satisfied the top-bottom/bottom-top pairing requirement of the MATRIX/FPGA1 trigger (defined in Table 3.2). Of those events that satisfied the first level of the emulated physics trigger, only about 5.3×10^3 produced a track and of the events that satistified the trigger and produced a track about 1.2×10^3 remained after track quality cuts.

3.2.1.2 The MATRIX/FPGA4 'Single Muon' Trigger

MATRIX/FPGA4 is a prescaled single road and single quadrant triggering configuration setting. Its purpose is to serve as a source of triggered single tracks but also to independently verify response of the detector to the first level of the physics MATRIX/FPGA1 trigger. Angular distributions of single muons as compared to the lowest intensity group are shown in 3.16.

Ignoring differences in trigger efficiency and different prescalings, the acceptance of the MATRIX/FPGA4 should be equivalent to that of the Level 1 trigger emulation applied over the NIM3. In the comparisons differing intensity, a slight intensity dependence exists at the edges of detector acceptance for both angular variables and becomes more pronounced in observations of track transverse momentum.

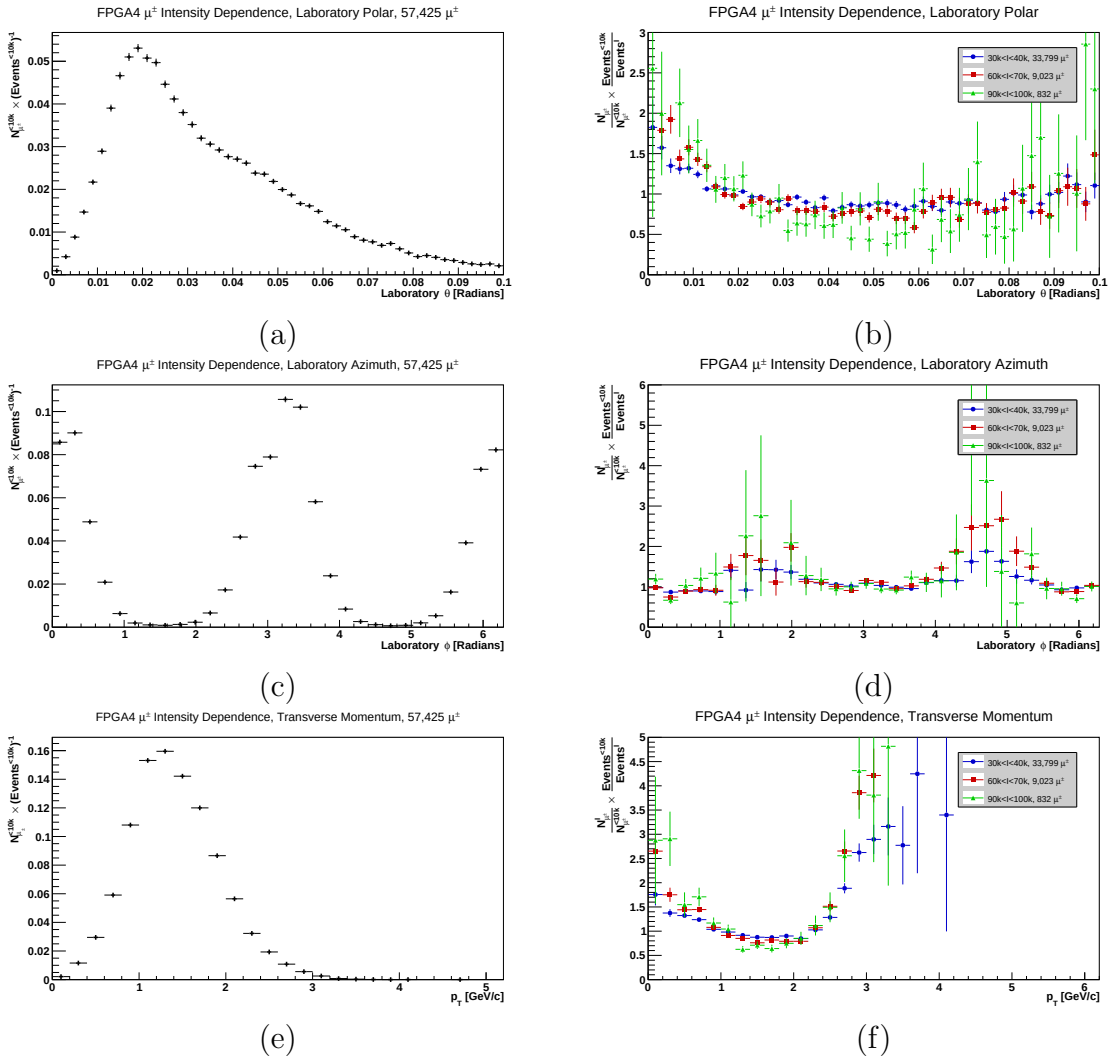

Figure 3.16: **MATRIX/FPGA4 Reconstucted Muon Trajectories.** Plots (a), (c), and (e), show distributions of laboratory angular variables and transverse momentum as collected by the trigger at intensities less than 10,000 ppp. Plots (b), (d), and (f) show comparisons of observables collected by the trigger at different intensities compared to the lower intensity events.

3.2.2 Trigger Efficiency

The efficiency of the physics trigger can be further decomposed into two separate components:

$$\epsilon^{Trig.}_{Data,i}(\mathcal{I}_i(t), X) = \epsilon^{Hodo.}_{Data}(X) \cdot \epsilon^{Recon.(FPGA1)}_{Data,i}(\mathcal{I}_i(t), X), \tag{3.15}$$

where $\epsilon_{Data}^{Hodo.}(X)$ is the collective efficiency of the hodoscope hardware at all stations as a function of dimuons observable and $\epsilon_{Data,i}^{Recon.(FPGA1)}(I_i(t), X)$ is the efficiency of the trigger as a function of intensity and dimuon observable. The effects of PMT voltage sag on the efficiency of the hodoscopes are assumed to be negligible, indicating no hodoscope dependence on intensity at the hardware level.

3.2.2.1 Hodoscope Angular Efficiency

The NIM1 (defined in 3.2) horizontal hodoscope coincidence trigger and overlapping configuration of the horizontal and vertical hodoscopes can be exploited to quantify hodoscope efficiencies in the bend direction. Using this method, stations two, three, and four are at least ninety-five percent efficient with exceptions in one element in station two and two elements in station three. Station one has the most inefficient elements and those panels tend to cluster around the outer edges of the station. The bottom half of the detector is also slightly less efficient than the top half which would certainly affect the angular distributions of the measured dimuons. The combined effect of all hodoscope inefficiencies is a fifteen percent loss in the number of accepted and tracked dimuons in the azimuthal angle, but this leads to only a one percent change in the magnitude of the extracted ν-coefficient. Further details of this study, which was performed by David Kleinjan of Los Alamos National Laboratory (LANL), are available in the collaboration document database [100].

3.2.2.2 MATRIX/FPGA1 Trigger Efficiency

The efficiency of the physics trigger can be estimated using a MATRIX/FPGA1 "pseudo-efficiency" measurement:

$$\epsilon^{Recon.(FPGA1)}_{Data,i}(\mathcal{I}_i(t), X) \approx p\epsilon^{Recon.(FPGA1)}_{FPGA4/NIM3,i} = \sum_{j=Targets} \frac{E^{Recon.(EmuFPGA1(NIM3))}_{NIM3,j}}{E^{Recon.(FPGA1)}_{FPGA1,i}} \frac{dN^{Recon.(FPGA1)}_{FPGA1,i}}{dX} \left(\frac{dN^{Recon.(EmuFPGA1(NIM3))}_{NIM3,j}}{dX} \right)^{-1}, \tag{3.16}$$

where $E^{Recon.(EmuFPGA1(NIM3))}_{NIM3,j}$ is the event normalization for the sum of all emulated MATRIX/FPGA1 events over all target positions for the NIM3 sample for Roadset 67, $E^{Recon.(FPGA1)_{FPGA1,i}}$ is the event normalization for reconstructed FPGA1 events from the MATRIX/FPGA1 sample for Roadset 67, and the differential yields of the indicated sample are defined with regard to the dimuon observable. Whereas a true efficiency calculation would tally the number of successfully reconstructed events over a given training sample, a pseudo-efficiency compares the relative rate of successful event reconstruction for two different samples, and uses emulation and normalization to match sample composition and relative rate. Rates are normalized per event rather than time or luminosity because neither of those units remain constant over the operation of the experiment. This method is useful when no true training sample exists and one sample is assumed to be the subset of another. In this case, the NIM3 sample is the E906/SeaQuest "minimum-bias" trigger, therefore it must contain the types of the events which fire the MATRIX/FPGA1 trigger.

Unfortunately, the rejection factor for the physics trigger is $\sim 10^6$ for the Roadset 67 configuration yielding an emulated sample size from NIM3 on the order of tens of events. One way around this limitation is to assume that to first order, a MATRIX/FPGA1 event is equivalent to a pair of MATRIX/FPGA4 single muon events

with intensity matching to simulate second order effects:

$$\epsilon_{Data,i}^{Recon.(FPGA1)}(\mathcal{I}_i(t), X) \approx [\epsilon_{Data,i}^{Recon.(FPGA4)}(\mathcal{I}_i(t), Y)]^2 \tag{3.17}$$

where $\epsilon_{Data,i}^{Recon.(FPGA4)}(\mathcal{I}_i(t), Y)$ is the efficiency of MATRIX/FPGA4 single muon trigger. Instead of an actual efficiency, a pseudo-efficiency was calculated:

$$p\epsilon_{FPGA4/NIM3}^{Recon.(FPGA4)}(\mathcal{I}(t), Y) = \sum_{i,j=Targets} \frac{E_{NIM3,j}^{Recon.(EmuFPGA4(NIM3))}|_{\mathcal{I}_j(t)}}{E_{FPGA4,i}^{Recon.(FPGA4)}|_{\mathcal{I}_i(t)}} \cdot \frac{dN_{FPGA4,i}^{Recon.(FPGA4)}|_{\mathcal{I}_i(t)}}{dY} \left[\frac{dN_{NIM3,j}^{Recon.(EmuFPGA4(NIM3))}|_{\mathcal{I}_j(t)}}{dY}\right]^{-1}. \tag{3.18}$$

Explicit in equation 3.18 is a double sum over all available NIM3 and FPGA4 target events as well as explicit indication that all values are to be calculated at similar intensities. Total and intensity dependent summaries of pseudo-efficiency calculations are shown in Figure 3.17 and Figure 3.18. The most glaring feature of the MATRIX/FPGA4 pseudo-efficiency calculations is their dependence on reconstructed observables, indicating that single muon observables could vary at the trigger level. Since the MATRIX/FPGA1 physics trigger is currently dependent on the pseudo-efficiencies calculated for MATRIX/FPGA4, it is reasonable to assume that the MATRIX/FPGA1 trigger also suffers from dependence on intensity and reconstructed observable.

-

3.2.3 Dimuon Reconstruction Efficiency

Referring back to equation 3.14, the second contribution to efficiency must be evaluated. At this stage, the dimuon event reconstruction efficiency depends on the efficiency of the event reconstruction software (known as kTracker) and the collective

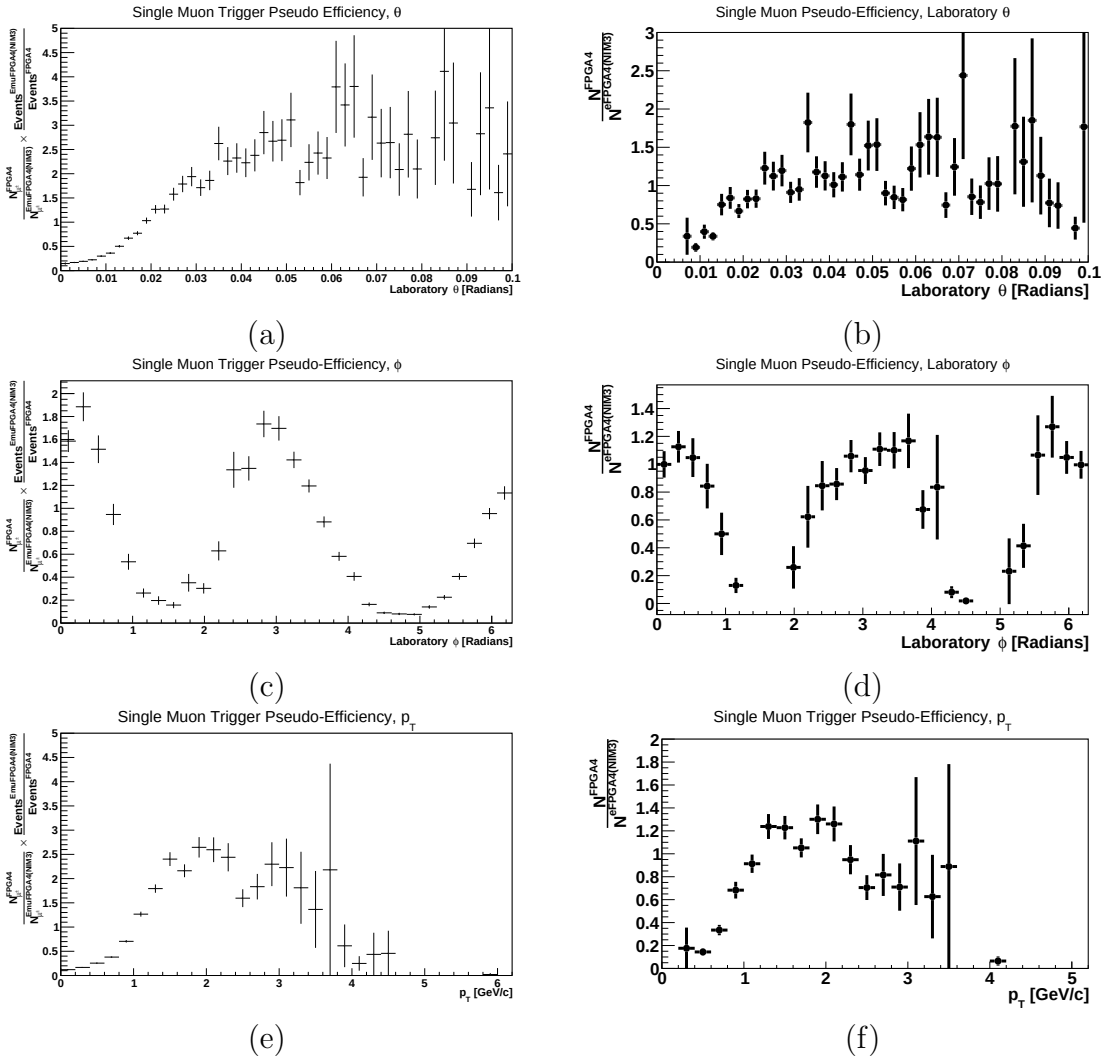

Figure 3.17: **MATRIX/FPGA4 Trigger Angular & Transverse Momentum Pseudo-Efficiency.** Figures (a), (c), and (e) are all raw pseudo-efficiency measurements of the laboratory θ, ϕ, and p_T (respectively). Raw pseudo-efficiency indicates that all reconstructed muons were included in the calculation. Figures (b), (d), and (f) are all pseudo-efficiency measurements with track quality cuts applied. Differences besides minor changes in shape for laboratory ϕ are the overall normalization which converges to unity when all cuts are applied.

hardware efficiency of the chambers in each station:

$$\epsilon^{Recon.}_{Embed.,i}(\mathcal{I}_i(t), X) = \epsilon^{Chamber.}_{Data}(\mathcal{I}_i(t), X) \times \epsilon^{Recon.(\mu\bar{\mu})}_{MC+NIM3}(\mathcal{I}_i(t), X)) \tag{3.19}$$

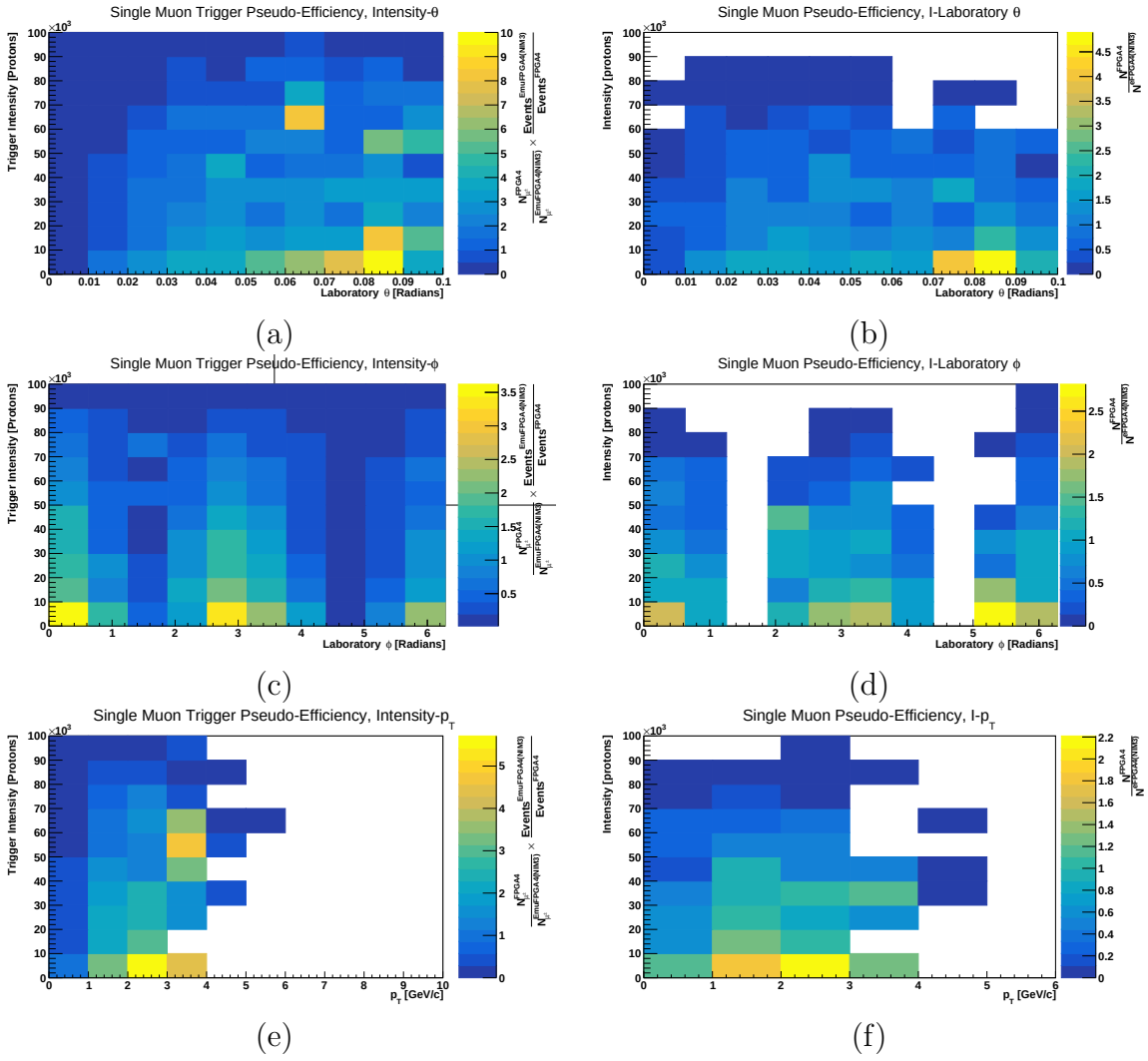

Figure 3.18: **MATRIX/FPGA4 Trigger Angular & Transverse Momentum Intensity Dependent Pseudo-Efficiency.** Figures (a), (c), and (e) are all raw pseudo-efficiency measurements of the laboratory θ, ϕ, and p_T (respectively) with intensity dependence. Raw pseudo-efficiency indicates that all reconstructed muons were included in the calculation. Figures (b), (d), and (f) are all intensity dependent pseudo-efficiency measurements with track quality cuts applied. Bright yellow squares indicate regions where the MATRIX/FPGA4 trigger accepts more tracks than found in the FPGA4 emulation over NIM3 sample.

where here yet another outer product implies that the efficiency of the tracker is correlated with the behavior of the chambers as a function of intensity. Rather than attempt to deal with the cross terms, it can be assumed that the intensity dependence

of the chambers can be measured at the lowest intensity and the competing effects of chamber efficiency and muon trajectory reconstruction dealt with as a combined track reconstruction efficiency problem:

$$\epsilon^{Recon.}_{Embed.,i}(\mathcal{I}_i(t), X) = \epsilon^{Chamber.}_{Data}(0, X) \cdot \epsilon^{Recon.(\mu\bar{\mu})}_{MC+NIM3}(\mathcal{I}_i(t), X). \tag{3.20}$$

where the chamber efficiency at $\mathcal{I}_i(t) = 0$ would be the chamber acceptance with a hardware efficiency correction calculated at low occupancy. Since reconstruction acceptance was addressed in the previous chapter and all relationships with acceptance are linear, only the low occupancy efficiency needs to be considered. A study conducted by Kenichi Nakano shows that overall chamber efficiency is capped at 96% for the first station, 94% for the second station, 94% for the upper part of the third station, and 97% for the lower part of the third station however it is unclear how these changes in chamber efficiency might affect angular distributions as there was no significant localization of any particular inefficiency [101]. A loss of global chamber hits would certainly affect the overall yield, but the relative relationship between bins in observables would not change indicating that contribution to the observed angular parameters would likely be negligible at low intensity.

3.2.3.1 kTracker Reconstruction Efficiency

To evaluate the efficiency of the muon trajectory reconstruction program as a function of intensity, a set of data which combined standard Drell-Yan simulations with NIM3 trigger data from Roadset 67 was created in a process called "embedding". It was assumed that as long as enough events were processed, a realistic intensity dependent efficiency correction could be extracted, as the reconstruction software would identify simulated hits in realistic local and global hit distributions at the same rate as real hits within those same distributions. kTracker reconstruction efficiency

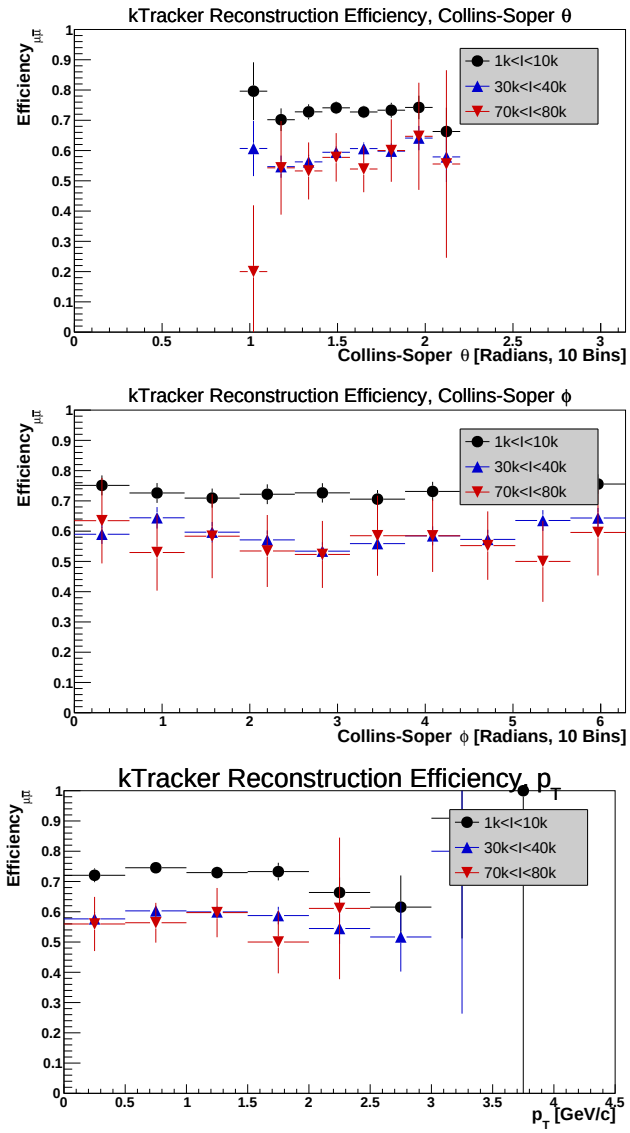

Figure 3.19: **kTracker Intensity Dependent Angular & Transverse Momentum Efficiency.** All three graphs show reconstruction efficiency as a function of intensity in dimuon observable, as calculated by comparing embedded data to base kTracker efficiency. The top and middle graphs are the polar and azimuthal angular variables in the Collins-Soper frame (respectively) and the bottom is the intensity dependent reconstruction efficiency of dimuon transverse momentum. All intensity dependent efficiency measurements have all single and dimuon quality cuts applied.

is show in Figure 3.19. In extractions from data, intensity corrections are applied as inverse weights on an event-by-event basis. Final bin error is recalculated with the addition of each event as a quadrature sum of total bin error and intensity correction

error as a function of unit weight.

3.3 Extractions of Angular Moments from Simulation

It is assumed that the magnitudes of the angular coefficients can be estimated after the application of the combined spectrometer correction to the angular yields of collected data, however, the effectiveness of the method should be verified before its application to data with intensity dependence. The angular moment extraction method in one-dimension was a weighted χ^2 least-squares based goodness-of-fit test, with comparison to the expected integrated modulation. For the polar angle the expected integrated modulation was:

$$\sin\theta\left[\kappa + \lambda\kappa\cos^2\theta\right], \tag{3.21}$$

and the expected value for λ is 1, indicating that in the quark-anti-quark annihilation process, virtual photons are always transversely polarized. In the azimuthal angle the expected integrated modulation was

$$\kappa + \nu\kappa\cos 2\phi, \tag{3.22}$$

and the expected ν value is zero. Angular moments were then extracted from a two-dimensional yield with modulation:

$$\sin\theta\left[\kappa + \lambda\kappa\cos^2\theta + \mu\kappa\sin 2\theta\cos\phi + \frac{\nu}{2}\kappa\sin^2\theta\cos 2\phi\right], \tag{3.23}$$

with expected $\lambda = 1$ and expected $\mu = \nu = 0$. The correction factor without intensity consideration is shown in Figure 3.20.

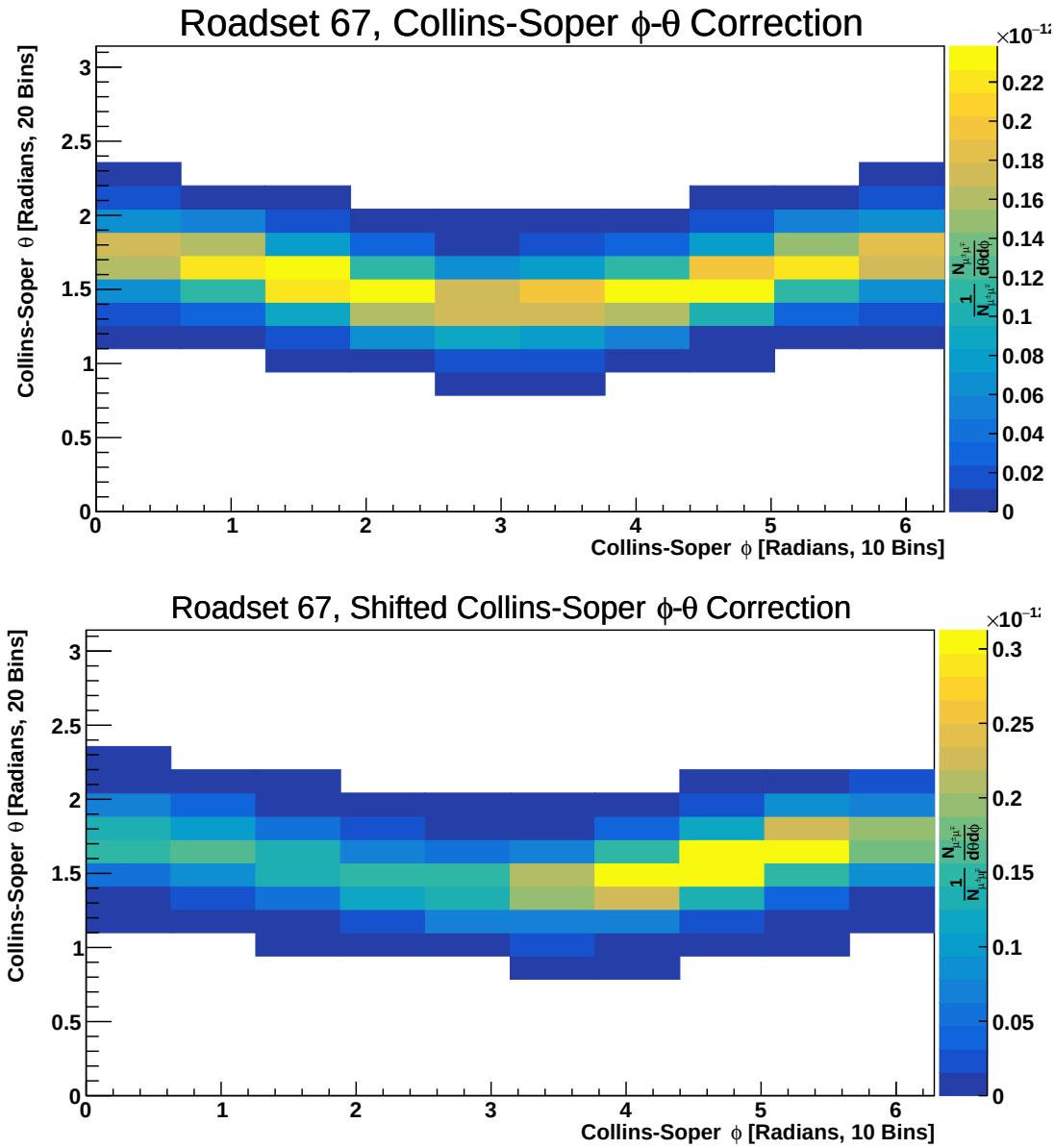

Figure 3.20: **Two Dimensional Angular Correction Factors.** The two correction factors are Drell-Yan simulation data with all applied cuts. The difference between the top and bottom graphs is a 1.7 centimeter y-axis beam shift in simulation which leads to a large asymmetry in angular distributions.

3.3.0.1 Simulated Modulation Datasets

In standard signal simulations, "flat" ϕ-distributions were created by randomly choosing a number from the interval $[0, 2\pi]$ and setting that as the azimuthal angle of the generated event. For testing of extraction accuracy, precision, and the presence of systematic uncertainties inherent to the extraction method, multiple simulated datasets were produced each with an artificially generated $\cos(2\phi)$ modulation of a given magnitude. Modulation magnitudes were implemented through biased random number generation on the interval $[0, 2\pi]$, with the bias described in equation 3.24 understood to be a probability distribution function based on the desired modulation:

$$1 - \nu + \nu \cos 2\phi. \tag{3.24}$$

Another random number was then generated on the interval $[0, 1]$ and compared to the random limit from the probability distribution function. If the comparison passed the event was kept, if not it was thrown away. A summary of simulated datasets used to test the analysis method in this note are shown in Table 4.1.

3.3.0.2 Extraction of Angular Moments from Simulated Modulations

Drell-Yan simulations with artificial angular modulations were treated exactly like measured data sans additional analysis for background subtraction or intensity dependence. Cuts were made to maximize single muon track reconstruction quality, dimuon pair quality, and to limit the edge effects of the detector. In particular a fiducial cut in the polar angle of $|\cos\theta| < 0.452$ was applied. The ν and λ moments were extracted from one-dimensional yields which differed with respect to the azimuthal angle, and were integrated in ϕ, θ, and p_T where relevant. The extracted polar moments are shown in Figure 3.21 along with the ϕ dependent moments. Tables 3.3 and 3.4 show the extraction parameters for both one dimensional extractions. Two

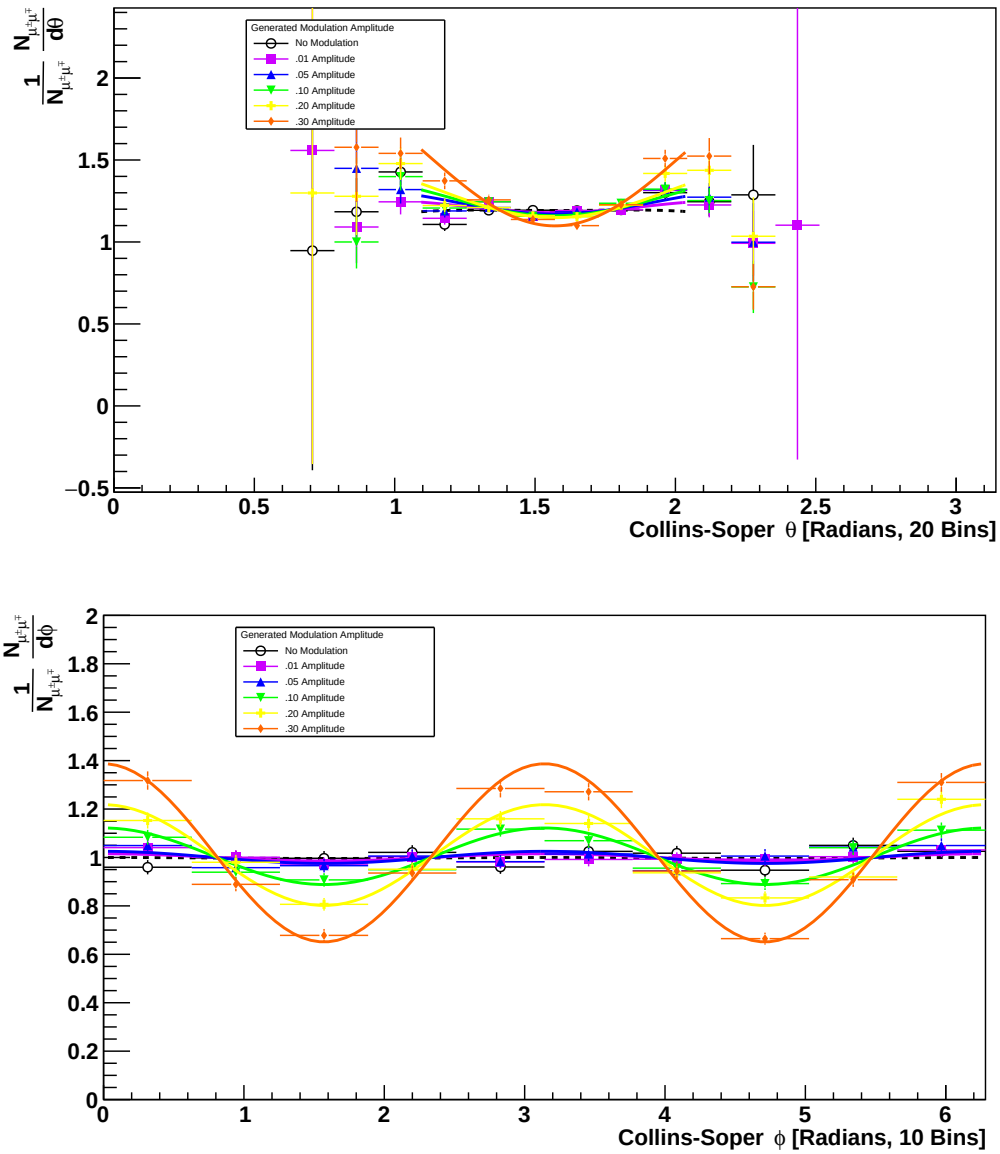

Figure 3.21: **One Dimensional Extractions of Angular Moments from Simulated Modulations.** The top graph shows extractions from the azimuthal angle and the bottom graph shows extractions from the polar angle. Extractions which are dependent on the polar angle show a high sensitivity to the relationship between the outer points and inner points.

dimensional extractions are shown in Figure 3.22 and Table 3.5

Notable features are the limitations of extractions given the resolution and acceptance in the polar angle. Not only are extractions of λ more than one standard de-

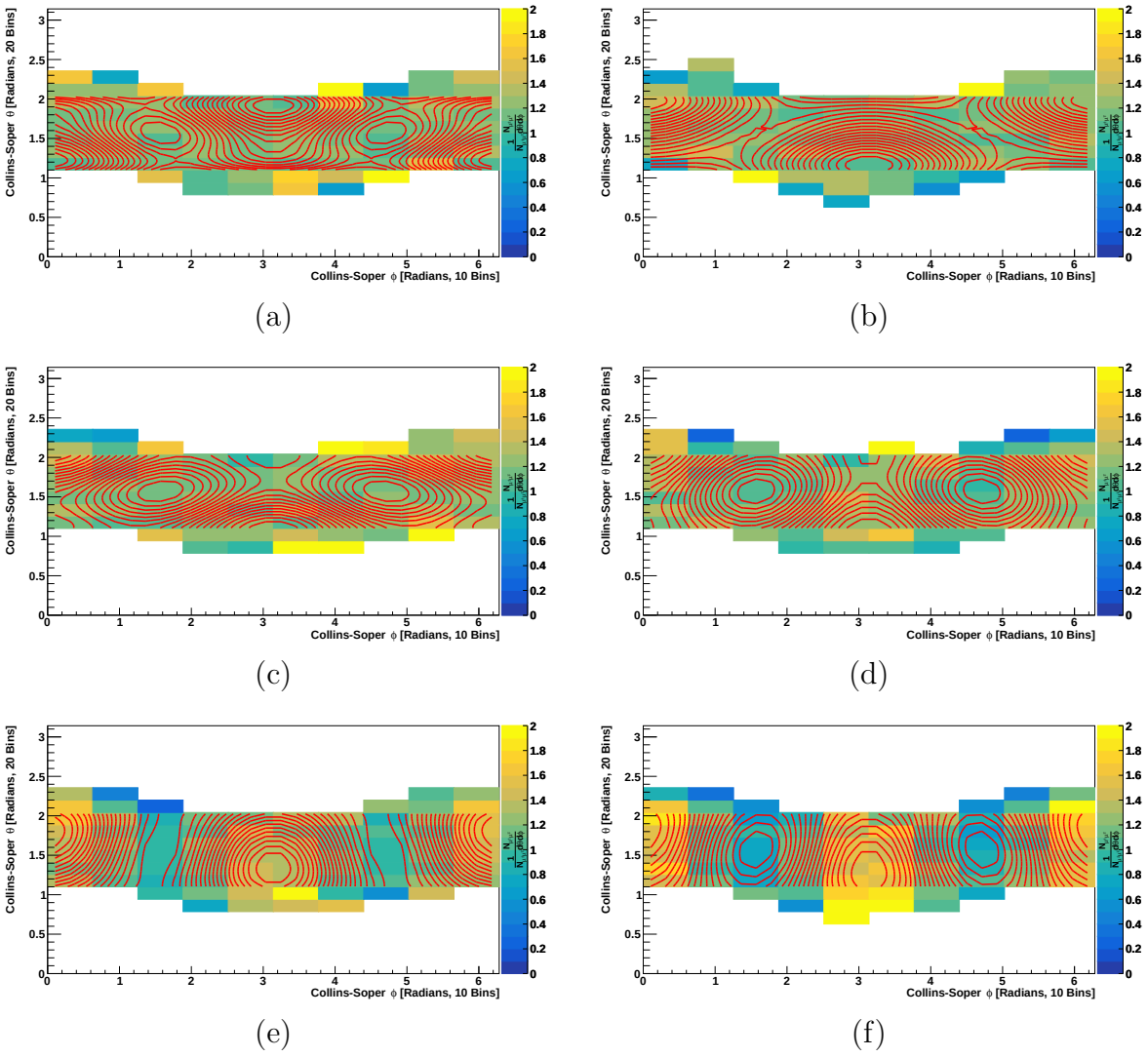

Figure 3.22: **Two Dimensional Extractions of Angular Moments from Simulated Modulations** Extractions are arranged alphabetically from lowest generated ν modulation to highest ν modulation. Fits were evaluated over the full azimuthal range but limited in the polar angle in order to minimize the edge effects of spectrometer acceptance. Fits to the data show a natural mixing of the polar and azimuthal angles which is purely a function of acceptance.

viation from the thrown value but one dimensional and two dimensional extractions disagree with each other above a certain thrown azimuthal modulation amplitude. Extractions of the ν modulation agree with each other and the thrown value in all but two cases. In two dimensional extractions a slight mixing of angular variables

persists but is mostly a function of the limited polar acceptance.

$\sin\theta\Big[[\kappa] + [\lambda\kappa]\cos^2\theta\Big]$ Extractions				
Generated ν	$\chi^2/n.d.f$	λ	$[\kappa]$	$[\lambda\kappa]$
None	$10.332/4 \approx 2.583$	0.562 ± 0.216	1.190 ± 0.017	0.670 ± 0.257
.01	$11.930/4 \approx 2.983$	0.885 ± 0.212	1.180 ± 0.016	1.040 ± 0.250
.05	$6.072/4 \approx 1.518$	1.110 ± 0.216	1.170 ± 0.016	1.290 ± 0.253
.10	$7.263/4 \approx 1.816$	1.330 ± 0.215	1.160 ± 0.016	1.540 ± 0.248
.20	$9.214/4 \approx 2.304$	1.560 ± 0.234	1.150 ± 0.016	1.790 ± 0.268
.30	$5.216/4 \approx 1.304$	2.870 ± 0.274	1.100 ± 0.017	3.150 ± 0.297

Table 3.3: **One Dimensional Extractions of Polar Moments from Simulated Modulations.** Polarizations were all thrown at unity by simulation ($\lambda = 1$). All fits have a reduced χ^2 of less than 3. Half of all extractions are within two standard deviations of the thrown value with the lowest and second highest generated ν at 2.02 and 2.11 standard deviations respectively. Polar extractions fail for $\nu > .30$.

$[\kappa] + [\nu\kappa]\cos(2\phi)$ Extractions				
Generated ν	$\chi^2/n.d.f$	ν	$[\kappa]$	$[\nu\kappa]$
None	$12.025/8 \approx 1.503$	0.002 ± 0.014	0.998 ± 0.0094	0.002 ± 0.014
.01	$3.634/8 \approx 0.454$	0.015 ± 0.013	1.000 ± 0.0089	0.015 ± 0.013
.05	$12.755/8 \approx 1.594$	0.025 ± 0.014	1.000 ± 0.0090	0.025 ± 0.014
.10	$9.623/8 \approx 1.203$	0.116 ± 0.014	1.000 ± 0.0092	0.117 ± 0.014
.20	$7.814/8 \approx 0.977$	0.206 ± 0.015	1.010 ± 0.0097	0.208 ± 0.015
.30	$3.404/8 \approx 0.425$	0.361 ± 0.015	1.020 ± 0.0103	0.368 ± 0.015

Table 3.4: **One Dimensional Extractions of Azimuthal Moments from Simulated Modulations.** Azimuthal moment magnitudes in simulations (ν) were varied up to .30. Most extractions are within one standard deviation of the thrown value, with the agreement of the highest value having the largest difference from its thrown value. Fit quality is good in all cases.

Extractions from simulated angular moments show a slight depedence on extraction method and the true magnitude of the azimuthal moment. As the azimuthal moment magnitude increases, a binned least squares fit in two dimensions tends to underestimate the true polar moment and shows ν dependence in the mixed term. No advantage is gained over using a one-dimensional extraction technique for extracting polar or azimuthal moments, however a simultaneous fit of both variables is necessary to extract the mixed term.

$\sin\theta \left[[\kappa] + [\lambda\kappa]\cos^2(\theta) + [\mu\kappa]\sin(2\theta)\cos(\phi) + [\nu\kappa]\sin^2(\theta)\cos(2\phi) \right]$				Extractions
Generated ν	$\chi^2/n.d.f$	λ	μ	ν
None	$52.652/56 \approx 0.940$	0.591 ± 0.204	0.016 ± 0.038	0.013 ± 0.015
.01	$62.781/56 \approx 1.121$	0.583 ± 0.201	-0.062 ± 0.036	0.017 ± 0.015
.05	$75.120/56 \approx 1.341$	0.765 ± 0.200	-0.032 ± 0.037	0.025 ± 0.015
.10	$49.185/56 \approx 0.878$	0.953 ± 0.203	-0.059 ± 0.038	0.106 ± 0.015
.20	$53.365/56 \approx 0.953$	0.357 ± 0.196	-0.136 ± 0.0384	0.213 ± 0.015
.30	$70.601/56 \approx 1.2607$	0.713 ± 0.21	-0.155 ± 0.0437	0.391 ± 0.017
Generated ν	$[\kappa]$	$[\lambda\kappa]$	$[\mu\kappa]$	$[\nu\kappa]$
None	1.186 ± 0.016	0.701 ± 0.242	0.019 ± 0.045	0.015 ± 0.018
.01	1.178 ± 0.015	0.687 ± 0.237	-0.073 ± 0.042	0.020 ± 0.017
.05	1.172 ± 0.015	0.896 ± 0.234	-0.037 ± 0.043	0.029 ± 0.017
.10	1.169 ± 0.015	1.115 ± 0.237	-0.069 ± 0.044	0.124 ± 0.018
.20	1.185 ± 0.016	0.423 ± 0.233	-0.161 ± 0.045	0.252 ± 0.018
.30	1.180 ± 0.016	0.841 ± 0.247	-0.183 ± 0.052	0.462 ± 0.019

Table 3.5: **Two Dimensional Extractions of Angular Moments from Simulated Modulations.** Thrown angular moments inlude a polar angle moment of unity ($\lambda = 1$), a mixed polar and azimuthal moment of ($\mu = 0$), and various azimuthal moments (ν : [Null, .30]). Fit qualities are all good, but the two dimensional extraction method systematically underestimates polar moments, overestimates the mixed terms at high ν, and faithfully reproduces ν moments up to .30. The mixed term tends to directly vary with the magnitude of the thrown modulation. The azimuth depedent term is extracted within one standard deviation in all but one of the six cases.

CHAPTER IV

Results

The final sequence of steps for measuring the estimated Drell-Yan dimuon angular yields as defined in equation 3.3 is evaluating the purity of $N_{Meas.,D}$, applying the necessary corrections for intensity and beam offset, and extracting the magnitude of the angular moments from the distributed data. The purity of the measured yield is estimated with a mass spectrum fit and acceptance and intensity dependent efficiency calculations are performed bin-by-bin but at different times during tabulation. Efficiency corrections are applied during sample tabulation using a weighted inverse intensity dependent look-up table while acceptance corrections with a simulated 1.7 centimeter beam offset in the y-direction are applied to the entire sample.

4.1 Sample Collection

The last of the three parts to be evaluated from equation 3.3 is $N_{Meas.,i}$, the data collected for evaluation at E906/SeaQuest. The Roadset 67 sample was collected in four second spills every minute over the course of one entire fiscal year, from the end of the 2014 Fermilab Shutdown in November until the beginning of the 2015 Fermilab Shutdown in June. The data were divided into one hour runs of about sixty spills a piece for a total of about 1.8×10^5 events per run. Target rotations were performed between spills, naturally dividing the data by target according to the spill

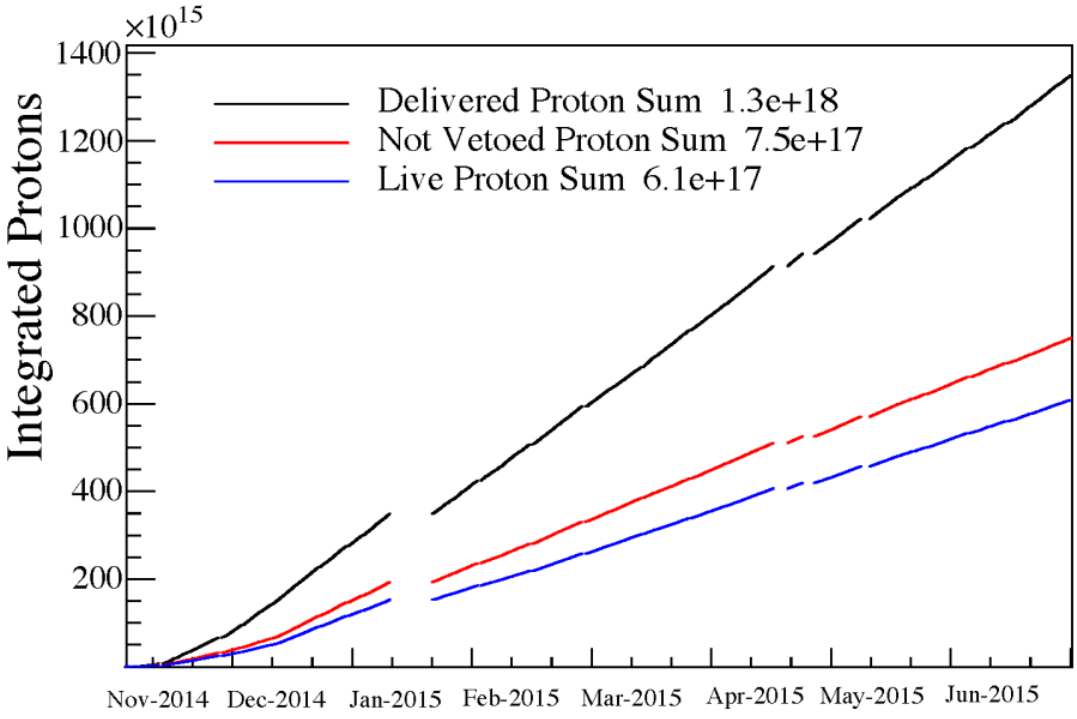

Figure 4.1: **Protons on Target for E906/SeaQuest during Fiscal Year 2015.** From the end of the Fermilab Shutdown in November of 2014 to the beginning of the Fermilab Shutdown in 2015, E906/SeaQuest received approximately 34% of its total beam on target. Of that 34%, about 47% was recorded for offline analysis.

cycle. This analysis focuses on the results from protons on the Deuterium target, $N_{Meas.,D}$, which compromises approximately 22% of all collected data for Roadset 67. The total amount of collected data as measured by the cumulative number of protons on target is shown in Figure 4.1. The Deuterium portion of Roadset 67 consists of 3.6265×10^4 spills which yield approximately 7.26×10^3 Drell-Yan events for analysis after all cuts. A summary of all datasets used in this analysis are shown in Figure 4.1.

After careful study of their effects, various cuts were applied to the Deuterium data in order to emphasize high-mass Drell-Yan events. These cuts were also applied to all other simulated and correction analysis samples. A summary of all analysis

cuts is shown in Table 4.2. Of particular importance is a dimuon mass cut at 4.2 GeV specifically to avoid sample contamination by the $J/\psi/\psi(1S)$ (3.097 GeV) and $\psi'/\psi(2S)$ (3.686 GeV) resonances.

Dataset	Type	Available Events	(λ, μ, ν)	Notes
mc_drellyan_LD2_M019_S001	Monte Carlo, Drell-Yan, D	1.07×10^6	(1,0,0)	Geometry "G17", simulated acceptance, collaboration standard
mc_drellyan_LD2_M019_S001_messy	Monte Carlo+NIM3, Drell-Yan, D	–	(1,0,0)	Geometry "G17" Monte Carlo with, embedded NIM3 in each event
mc_jpsi_LD2_M017_S001	Monte Carlo, J/ψ, D	5.89×10^5	(-,-,-)	Geometry "G17", simulated acceptance, collaboration standard
mc_psiprime_LD2_M017_S001	Monte Carlo, ψ',D	7.81×10^5	(-,-,-)	Geometry "G17", simulated acceptance, collaboration standard
user_bjrams87_LD2_0nu_3M_r67_v3_test	Monte Carlo, Drell-Yan, D	3.04×10^6	(1,0,0)	Geometry "G17", simulated acceptance, correction set
user_bjrams87_LD2_0nu_3M_r67_yshift_v3_test	Monte Carlo, Drell-Yan, D	2.88×10^6	(1,0,0)	Geometry "G17", simulated acceptance with 1.7 cm beam shift, correction set
user_bjrams87_LD2_0nu_1M_r67_v3_test	Monte Carlo, Drell-Yan, D	1.01×10^6	(1,0,0)	Geometry "G17", simulated acceptance, null result/control set
user_bjrams87_LD2_1nu_1M_r67_v3_test	Monte Carlo, Drell-Yan, D	9.42×10^5	(1,0,0.01)	Geometry "G17", simulated acceptance and modulation
user_bjrams87_LD2_5nu_1M_r67_v3_test	Monte Carlo, Drell-Yan, D	9.31×10^5	(1,0,0.05)	Geometry "G17", simulated acceptance and modulation
user_bjrams87_LD2_10nu_1M_r67_v3_test	Monte Carlo, Drell-Yan, D	9.09×10^5	(1,0,0.10)	Geometry "G17", simulated acceptance and modulation
user_bjrams87_LD2_20nu_1M_r67_v3_test	Monte Carlo, Drell-Yan, D	8.05×10^5	(1,0,0.20)	Geometry "G17", simulated acceptance and modulation
user_bjrams87_LD2_30nu_1M_r67_v3_test	Monte Carlo, Drell-Yan, D	7.01×10^5	(1,0,0.30)	Geometry "G17", simulated acceptance and modulation
MATIRX/FPGA1 Trigger, merged_roadset67_R006_V003	Data, Physics Trigger, D	$3.86 \times 10^4/7.26 \times 10^3$	(?,?,?)	Run 3, Geometry "G17", collected data, signal measuring set
MATRIX/FPGA1 Trigger, merged_Roadset67_R006_V003	Data, Physics Trigger, Empty Target	$1.10 \times 10^3/2.35 \times 10^2$	(-,-,-)	Run 3, Geometry "G17", collected data, used for background and corrections
MATRIX/FPGA1 Trigger, merged_roadset67_R006_V003	Data, Physics Trigger, No Target	$8.08 \times 10^2/1.48 \times 10^2$	(-,-,-)	Run 3, Geometry "G17", collected data, used for background and corrections
NIM3 Trigger, merged_roadset67_R006_V003	Data, Minimum Bias Trigger, All Targets	$1.34 \times 10^7/1.30 \times 10^3$	(-,-,-)	Run 3, Geometry "G17", collected data, used for background and corrections
MATRIX/FPGA4 Trigger, merged_roadset67_R006_V003	Data, Single Muon Trigger, All Targets	1.13×10^5	(-,-,-)	Run 3, Geometry "G17", collected data, used for background and corrections

Table 4.1: **Summary of all datasets used in the analysis.** Datasets are identified by generated Monte Carlo sample name for simulation or trigger and target for collected samples. Data sets with two numbers under available events show the number of events before and after analysis cuts.

Cut	Description
	Single Muon Selection Cuts
MATRIX1=true	Single muon tracks must come from events recorded as a result of the opposing detector quadrant trigger.
numHits > 13	Single muon tracks must have at least fourteen independent signals in the first three drift chambers.
-320.0 cm $< \mu^{\pm}_{z_0} < 10.0$ cm	Reconstructed single muon tracks must have an initial vertex between 3.2 meters upstream of the dump face and 0.1 meters downstream.
roadID != 0	Single muon tracks must satisfy the first level of the trigger.
	Single Muon Quality Cuts
$\lvert x_{Target} \times p_{z,\mathrm{D1}} \rvert < 320.0$ GeV/c $\cdot$ cm	Target retracked muon x-position multiplied by its z-momentum at the first drift chamber must be less than 320.0 GeV/c$\cdot$cm.
$\lvert (y_{Target} - 1.7 \text{ cm}) \times p_{z,\mathrm{D1}} \rvert < 320.0$ GeV/c $\cdot$ cm	Target retracked muon true y-position multiplied by its z-momentum at the first drift chamber must be less than 320.0 GeV/c$\cdot$cm.
$\lvert x_{Dump} \rvert < 32.0$ cm	Dump retracked muon x-position must be less than 32 cm.
$\lvert y_{Dump} - 1.7\text{cm} \rvert < 22.0$ cm	Dump retracked muon true y-position must be less than 22 cm.
$\sqrt{x^2_{Dump} + (y_{Dump} - 1.7 \text{ cm})^2)} > 3.0$ cm	Dump retracked muon must be at least 3 cm away from the beam line.
$\frac{\chi^2}{(\text{numHits-5})} < 5.0$	Single muon reconstruction must have a reduced χ^2 less than 5.
$\chi^2_{Target} < 15.0$	Target retracking of single muons must have a goodness-of-fit less than 13.
12.0 GeV/c $< p_{z,\mathrm{D1}} <$ 75.0 GeV/c	Single muons must have a certain z-momentum range at station 1.
-350.0 cm $< z_{0x} < 10.0$ cm	Single track reconstruction must have closest approach to the beam-axis within the target range.
$\lvert p_{x,Target} \rvert < 4.5$ GeV/c	Target retracked muon must have x-momentum less than 4.5 GeV/c.
$\lvert p_{y,Target} \rvert < 3.4$ GeV/c	Target retracked muon must have y-momentum less than 3.4 GeV/c.
$\lvert x_{Target} \rvert < 18.0$ cm	Target retracked muon must have x-position less than 18 cm.
$\lvert y_{Target} \rvert < 16.0$ cm	Target retracked muon must have y-position less than 16 cm.
$\lvert y_{Dump} + y_{Target} - 3.4 \text{ cm} - 130.0 \cdot \frac{p_y}{p_z} \rvert < 30.0$ cm	Average true retracked y-position and muon trajectory polar projection from the beam-axis has a difference less than 30.0 cm.
kmstatus = true	kTracker track fitting for the trakc converged.
	Dimuon Selection Cuts
$\lvert d_x \rvert, \lvert d_y \rvert < 0.7$ cm	Reconstructed dimuon vertex must be within 0.7 cm. of the beam line in both transverse directions (maximum distance of $.7sqrt2 \approx 1$ cm.
-300.0 cm $< dz < 200.0$ cm	Reconstructed dimuons must have an initial vertex between three meters upstream of the dump face and two meters downstream.
$\lvert dp_x \rvert, \lvert dp_y \rvert < 3.0$ GeV/c	p_x and p_y of reconstructed dimuons must be less than 3.0 GeV/c, (this limits p_T to $3\sqrt{2} \approx 4.243$) GeV/c
30.0 GeV/c $< dpz <$ 110.0 GeV/c	Longitudinal momemtum must be between 30.0 GeV/c and 120.0 GeV/c
$0.0 < x_1 < 1.0$	Bjorken-x of beam quark must be physical
$0.0 < x_2 < 1.0$	Bjorken-x of target quark must be physical
$\lvert x_F \rvert < 1.0$	Feynman-x of event must be physical
$\lvert \mu_z - \bar{\mu}_z \rvert < 250.0$ cm	Reconstructed dimuons must come from muon pairs with initial positions no more than two and a half meters apart.
$\chi^2_{\mu\bar{\mu}} < 15.0$	Dimuon reconstruction must be less than fifteen (this leads to a reduced χ^2 of less than one).
$\mu_{p_x} > 0.0$ and $\bar{\mu}_{p_x} < 0.0$	Single muon x-momentum must be in the appropriate direction for the magnet bend. This setting for roadsets 57, 59, 61, and 62.
$\mu_{p_x} < 0.0$ and $\bar{\mu}_{p_x} > 0.0$	Single muon x-momentum must be in the appropriate direction for the magnet bend. This setting for roadset 67.
$\text{roadID}_{\mu} \times \text{roadID}_{\bar{\mu}} < 0$	Reconstructed dimuons must have tracks which satisfy the first level of the trigger logic and be in opposing quadrants.
$q_{\mu} \cdot q_{\bar{\mu}} = 1$	Reconstructed muon trajectories must show bends consistent with oppositely charged muons.
	Dimuon Quality Cuts
$x_F > -0.2$	Drell-Yan must be mostly forward
$.18 < x_2 < .60$	Bjorken-x of the target quark must be greater than .18 and less than .64.
4.0 GeV/c^2 $< M_{\mu\bar{\mu}} <$ 8.7 GeV/c^2	Reconstructed dimuon mass must be greater than 4.0 GeV/c^2 and less than 8.7 GeV/c^2.
$0.94 < \theta < 2.2 \implies \lvert \cos(\theta) \rvert < .589$	Fiducial polar angle cut to minimize detector edge effects.
$N^{Hits}_{D1} < 200$	Event hits in station 1 must be less than 200.
$N^{Hits}_{D2} < 200$	Event hits in station 2 must be less than 200.
$N^{Hits}_{D3} < 200$	Events hits in station 3 must be less than 200.
$N^{Hits}_{D1} + N^{Hits}_{D2} + N^{Hits}_{D3} < 1000$	Events hits in all stations must be less than 1,000.
$\chi^2_{\mu\bar{\mu}} < 16.0$	Dimuon goodness-of-fit must be less than 16.
S:G2SEM $> 1.0 \times 10^{11}$ ppp	Number of protons on target as measured by the G2SEM over the course of a spill must be greater than 1.0×10^{11}.
$I_{trigger} > 1,000$ protons	The number of protons on target as calculated by dividing the QIE sum with the G2SEM value for an accepted event must be greater than 1,000.
$I_{trigger} < 100,000$ protons	The number of protons on target as calculated by dividing the QIE sum with the G2SEM value for an accepted event must be less than 100,000.
$\lvert I_{trigger} - I_{chamber} \rvert < 10,000$ protons	The difference between the calculated trigger intensity and the weighted average of protons in pulses 13 events before and after the triggered event must be less than 10,000 protons.
	Target/Dump Separation Cuts
Single Muon: $\chi^2_{Dump} - \chi^2_{Target} > 10.0$	The goodness-of-fit for retracking to the beam dump must be ten greater than the goodness-of-fit for retracking to the target.
Single Muon: $\chi^2_{Upstream} - \chi^2_{Target} > 10.0$	The goodness-of-fit for upstream retracking must be ten greater than the goodness-of-fit for retracking to the target.
Dimuon: -300.0 cm $< dz < -60.0$ cm	Target dimuons must have an initial vertex within three meters upstream of the beam dump face or sixty centimeters downstream from it.

Table 4.2: **Signal Cut Summary.** Summary of all signal cuts used in this analysis. When extracting shifted data, cuts dependent on vertical position are shifted up by 1.7 centimeters.

4.2 Sample Curation

As discussed earlier, background contamination is assumed to have multiple sources which are relatively easy to identify conceptually, but are much more difficult to constrain within collected data. A minor review of these sources starts with true dimuon events from different unwanted processes in the target, single muons which are accidentally combined into a pair which may come from the target but are considerably more likely to come from the dump, and pairs from Drell-Yan Dimuon events which do not occur in the target region. To attempt to quantify the contamination, a mass spectrum fit to collected data was created using process specific mass shapes generated by multiple single process simulations and input from data collected during EMPTY and NO TARGET spill cycles. Details about the Roadset 67 EMPTY and NO TARGET data sets are available in Table 4.1.

Dimuon Source	Description	Mixed	EMPTY	NO TARGET
Flask	$\mu\bar{\mu}$ from Flask	No	Yes	No
Upstream	$\mu\bar{\mu}$ from Upstream	No	Yes	Yes
Air 1	$\mu\bar{\mu}$ from Air Btwn Spec	No	Yes	Yes
Air 2	$\mu\bar{\mu}$ from Air Filled Targ	No	No	Yes
Dump	$\mu\bar{\mu}$ from Dump	No	Yes	Yes
Random 1	Targ Single Pairs	Yes	No	No
Random 2	Targ+Dump Single Pairs	Yes	No	No
Random 3	Dump Single Pairs	Yes	Yes	Yes

Table 4.3: **Description of Background.** Of all the possible sources contained in the collected Deuterium sample the EMPTY and NO TARGET samples contain all but single muons emanating from the target.

The reasoning behind using collected EMPTY and NO TARGET data as opposed to existing mixing methods requires some explanation. The current collaboration method uses event mixing from the collected Deuterium sample to approximate background in lieu of Monte Carlo simulation. In more detail, this means that single reconstructed muons that are not successfully reconstructed with an oppositely

charged partner are combined with other lone muons at the event level to simulate "accidental" pairing. Conceptually, this idea is sound: true Drell-Yan dimuon pairs are produced at a rate many orders of magnitude less than all relevant background, therefore it is unlikely that an unpaired muon is a signal muon, however it is unclear whether this method can produce realistic background in all relevant kinematic distributions at the same time. The current collaboration mixing method optimizes for mass but does not accurately reproduce the angular distributions of background. Other issues arise when using mixed event including overtraining or overtuning to assumed signal and a lack of statistical independence of the signal sample. A combination of known background from the EMPTY and NO TARGET samples is sparsely populated and also not optimized for mass resulting in a high reduced χ^2, but accurately reproduces angular background, prompting its use.

A summary of background sources produced by Kenichi Nakano is available in Table 4.3 [102]. From the decomposition of possible background sources it is clear that no single sample of data can accurately correct for all sources of background, indicating that some optimized linear combination of mixed event background along with EMPTY and NO TARGET samples is the best solution. In lieu of the collaboration mixing method, it is unclear whether pairs from dump singles or target singles dominate but if it is assumed that dump contamination is nonzero (as evidenced by the existence of NO TARGET and EMPTY target samples after all cuts) at least the combination of the two samples are known to be background pairs and are statistically independent. The two collected background samples also have realistic angular distributions and intensity dependence. A smoothed mass spectrum fit ($\chi^2/n.d.f. = 6.1$) along with associated residuals and pulls are shown in Figure 4.2.

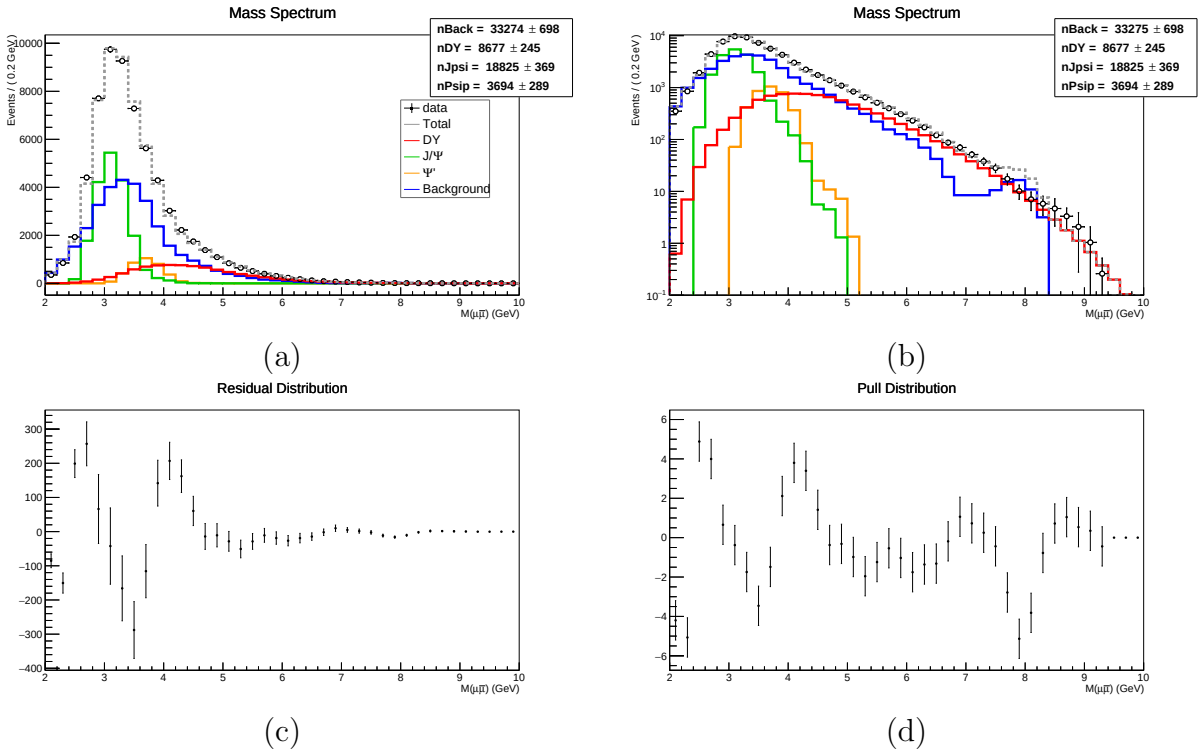

Figure 4.2: **Mass Spectrum Fits to Collected p+D Data.** Graphs (a) and (b) show the cumulative mass spectrum fit with four components. The open circles are the Deuterium distribution with all cuts applied except for an explicit mass cut at 4.2 GeV and x_T cut at 0.18. The green and yellow histograms are concentrations of the J/ψ and ψ' respectively. The blue histogram is the addition of the EMPTY and NO TARGET samples. Each histogram is smoothed in order to eliminate statistical fluctuations at high mass. However high mass fluctuations severely affect the quality of the fit. Graphs (c) and (d) show the fit model residual with respect to data. The pulls show the number of standard deviation each bin in the fit model is away from data.

4.3 Extraction of Angular Moments from Deuterium Sample

As illustrated in Figure 3.20, the acceptance of the spectrometer after the application of cuts severely limits the applicability of an overall bin-by-bin correction in two dimensions, therefore only results from one dimensional extractions are shown. As a result this analysis is insensitive to the mixed angular moment term. Results are divided into four categories: a standard sample set which has all standard collab-

oration cuts and sample preparation techniques, a "Beam Shift" sample, an "I" or intensity corrected sample, and an "I+Beam" intensity and beam shifted sample.

The standard sample uses a collection level correction on momentum components intended to counteract the effects of the beam offset. This means that at the moment of event tabulation in various kinematic distributions, the momenta components in the y and z direction were shifted by some precalculated amount to account for the beam offset of 1.7 centimeters relative to the SeaQuest spectrometer. Unfortunately, momentum based beam shift correction is applied at the event level and does not consider an inherent acceptance difference as a result of the beam shift (i.e. muon trajectories from an event may be shifted in and out of the solid angle covered by the spectrometer), making it unsuitable for a serious angular analysis.

The "Beam Shift" sample is defined by its combined spectrometer correction factor which, instead of correcting the data at the collection level, introduces the effect of the offset at the simulation level (shown in the second graph of Figure 3.20). This was done to minimize the effects of acceptance differences between simulation and the collected sample. The "I" or intensity dependence sample is characterized by an intensity based weighting applied at the collection level. The idea here was to include a correction of intensity dependence that led to accurate relative angular yield. The "I+Beam" sample includes intensity corrections at the collection level as detailed with the "I" sample as well as a beam shift at the acceptance level as applied in the "Beam Shift" sample.

4.3.1 Polar Moment Extractions

Extractions of the polar moment are shown first as a function of intensity in Figure 4.3 and Table 4.4. All extractions are performed over the range $|\cos\theta| < 0.462 \implies 1.09 < \theta < 2.04$ in order to avoid edge acceptance effects. In all configurations the lowest ($I < 10k$) and highest ($50k < I < 60k$) intensity bins tend

Intensity Dependent $\sin\theta \left[[\kappa] + [\lambda\kappa] \cos^2\theta \right]$ Extractions				
	Standard		Beam Shifted	
Intensity	$\chi^2/n.d.f$	λ	$\chi^2/n.d.f.$	λ
$I < 10k$	$7.859/4 \approx 1.965$	-2.420 ± 0.707	$5.924/4 \approx 1.481$	-2.130 ± 0.713
$10k < I < 20k$	$1.830/4 \approx 0.458$	-0.297 ± 0.701	$0.837/4 \approx 0.209$	-0.111 ± 0.703
$20k < I < 30k$	$5.637/4 \approx 1.409$	0.264 ± 0.862	$7.512/4 \approx 1.878$	0.424 ± 0.871
$30k < I < 40k$	$5.180/4 \approx 1.295$	0.305 ± 1.240	$2.523/4 \approx 0.631$	0.633 ± 1.230
$40k < I < 50k$	$5.065/4 \approx 1.266$	-0.667 ± 1.360	$5.177/4 \approx 1.294$	0.745 ± 1.500
$50k < I < 60k$	$7.925/4 \approx 1.981$	-4.210 ± 1.590	$5.302/4 \approx 1.326$	-2.82 ± 1.900
	I Corrected		I+Beam Corrected	
Intensity	$\chi^2/n.d.f$	λ	$\chi^2/n.d.f.$	λ
$I < 10k$	$7.880/4 \approx 1.970$	-2.360 ± 0.714	$6.184/4 \approx 1.546$	-2.050 ± 0.721
$10k < I < 20k$	$1.316/4 \approx 0.329$	-0.177 ± 0.713	$1.320/4 \approx 0.330$	-0.025 ± 0.713
$20k < I < 30k$	$4.806/4 \approx 1.202$	0.387 ± 0.871	$6.939/4 \approx 1.735$	0.630 ± 0.885
$30k < I < 40k$	$3.676/4 \approx 0.919$	0.569 ± 1.250	$1.482/4 \approx 0.370$	0.857 ± 1.230
$40k < I < 50k$	$3.485/4 \approx 0.871$	-0.441 ± 1.410	$3.585/4 \approx 0.897$	1.000 ± 1.560
$50k < I < 60k$	$7.014/4 \approx 1.753$	-4.090 ± 1.600	$4.280/4 \approx 1.070$	-2.680 ± 1.910

Table 4.4: **One Dimensional Intensity Dependent Extractions of Polar Moments from Collected p+D Data.** The expected polar moment is unity ($\lambda = 1$). Polar moment extractions from data are divided into four groups with sample differences explained in the text. The group that most approaches expected values is the "I+Beam" Corrected sample. Plots of all extractions are shown in Figure 4.3.

to underestimate all other intensity bins. Intensity corrections tend to have a small effect on extracted polar moments while the application of acceptance based beam shift corrections having the largest effect on extractions. These values indicate that intensity effects persist even after the application of a pulse size parameterization and correction.

Polar moment extractions integrated over intensity for the entire dataset are shown in Figure 4.4 and Table 4.5 accompanied by extractions over all collected background with standard cuts (shown at the bottom of Figure 4.4) and an "I+Beam" sample treatment. The extracted value to be used for the preparation of a final result is the "I+Beam" corrected sample, however its extracted $\lambda \approx 0$ implies that background contamination for the set overwhelms any possible signal from Drell-Yan on the Deu-

terium target. An estimate of competing magnitudes of the same angular moment from signal and background can be performed using estimates of sample contamination gained from Figure 4.2 and the following equation:

$$\begin{aligned} \lambda^{DY}(1-r) + r\lambda^{Bg} &= \lambda^{Sa}, \\ \lambda^{DY} &= \frac{\lambda^{Sa} - r\lambda^{Bg}}{1-r}, \end{aligned} \tag{4.1}$$

where λ^{Sa} is the extracted polarization from the sample before background subtraction, r is the estimated percentage of background contamination in the sample, and λ^{Bg} is the extracted polarization of the background sample [103, 104]. Using the "I+Beam" and "Background" values from Table 4.5 along with an estimated background contamination of 39.3%, calculated by integrating the mass spectrum fit above 4.2 GeV, yields a $\lambda^{DY} = -1.13$.

$\sin\theta\Big[[\kappa] + [\nu\kappa]\cos^2\theta\Big]$ Extractions				
Sample Class	$\chi^2/n.d.f$	λ	$[\kappa]$	$[\lambda\kappa]$
Standard	$10.846/4 \approx 2.712$	-0.555 ± 0.440	525.0 ± 14.0	-291.0 ± 231.0
I	$7.562/4 \approx 1.890$	-0.401 ± 0.450	797.0 ± 21.3	-320.0 ± 358.0
Beam	$7.342/4 \approx 1.835$	-0.235 ± 0.440	520.0 ± 13.6	-122.0 ± 229.0
I+Beam	$5.576/4 \approx 1.394$	-0.069 ± 0.450	788.0 ± 20.8	-54.2 ± 354.0
Background	$6.500/4 \approx 1.625$	1.580 ± 2.030	41.0 ± 4.10	65.0 ± 83.1

Table 4.5: **One Dimensional Extractions of Polar Moments from Collected p+D Data.** The expected polar moment is unity ($\lambda = 1$). Fit quality improves as more corrections are applied however the extracted value does not move towards the expected value and instead indicates the lack of any relevant polarization of the virtual photon. Plots of all extractions are shown in 4.4.

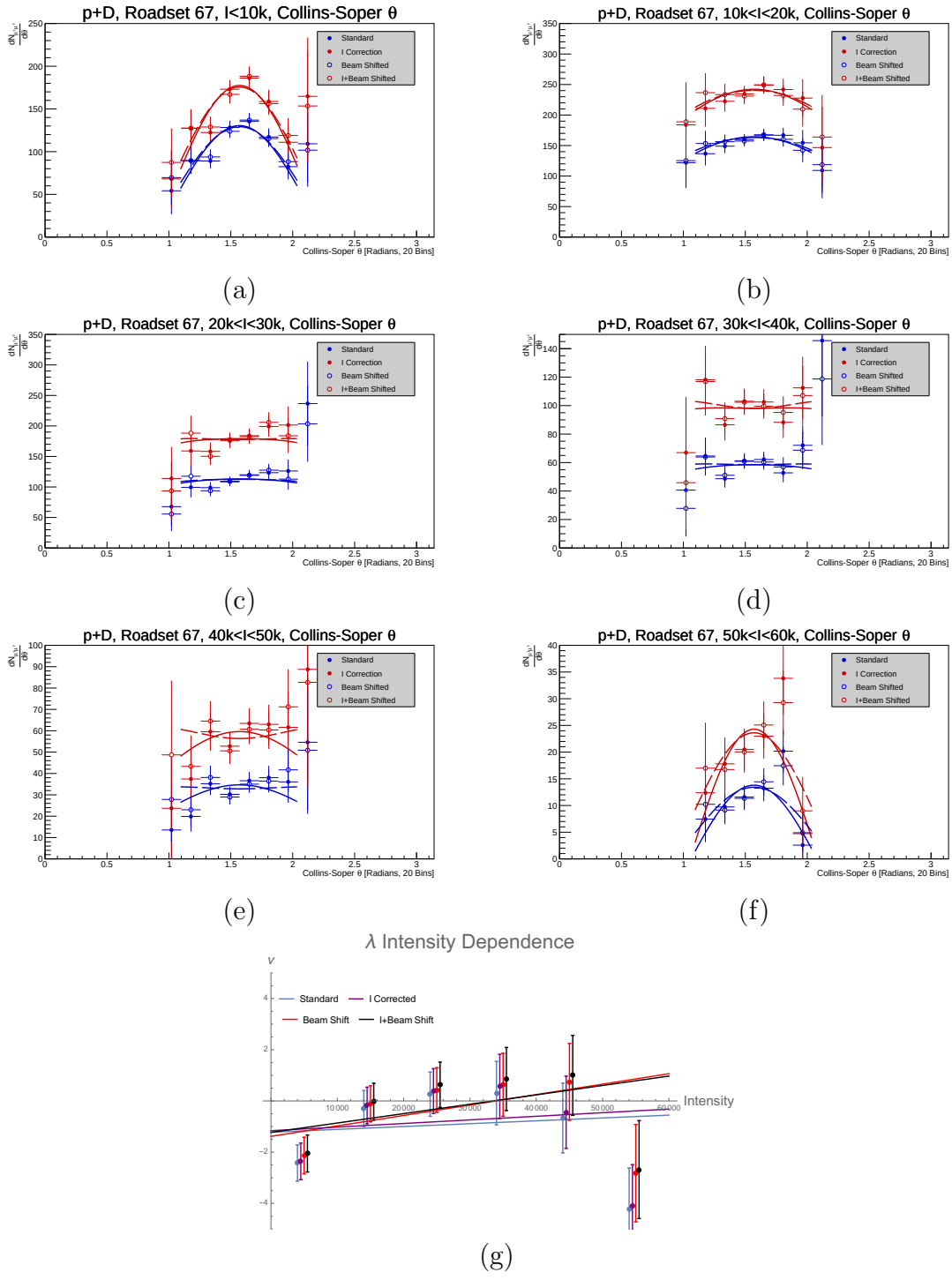

Figure 4.3: **One Dimensional Intensity Dependent Extractions of Polar Moments from Collected p+D Data.** The expected polar moment is unity ($\lambda = 1$) for all polar moment extractions. Sample differences are described in text. Graph (g) shows explicitly how λ varies with intensity. The "I+Beam" corrected sample most approaches expected extraction values. Goodness of fit and extracted values for all graphs are shown in Table 4.4.

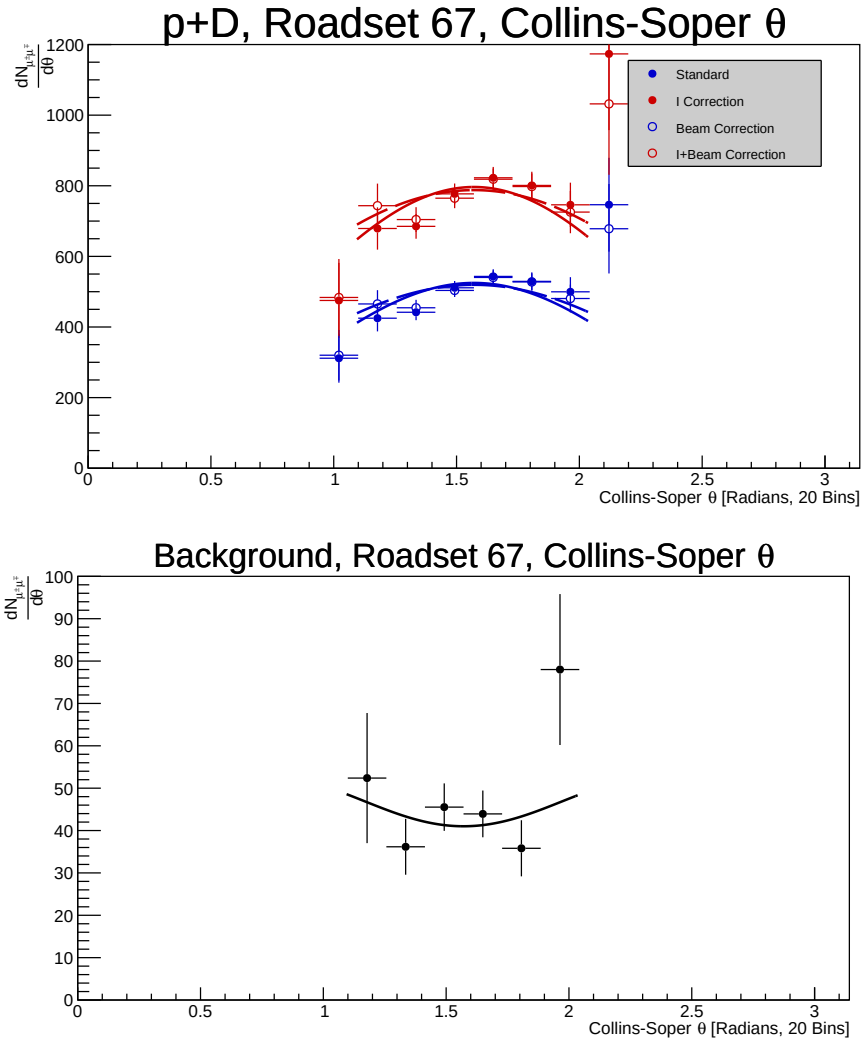

Figure 4.4: **One Dimensional Extraction of Polar Moments from Collected p+D Data.** The expected polar moment is unity for signal ($\lambda = 1$) and zero for background ($\lambda = 0$). The top graph shows extractions of polar moments, integrated over intensity and with various corrections applied. The bottom graph shows a polar moment extraction from the angular distribution of the background data. Goodness of fit and extracted values for all graphs are shown in Table 4.4.

4.3.2 Azimuthal Moment Extractions

The structure of the previous section is adapted for use with presentation of the azimuthal moment extraction from the Deuterium sample. Shown first are extractions of the azimuthal moment as a function of intensity in Figure 4.5 and Table 4.6. Extractions are performed over a wider polar range of $|\cos\theta| < 0.589 \implies 0.94 < \theta < 2.2$. In this case, the lowest intensity bin tends to underestimate all other bins in all sample configurations, however intensity dependence is less pronounced as intensity increases in all sample configurations.

Intensity Dependent $[\kappa] + [\nu\kappa]\cos 2\phi$ Extractions				
	Standard		Beam Shifted	
Intensity	$\chi^2/n.d.f$	ν	$\chi^2/n.d.f.$	ν
$I < 10k$	$3.705/8 \approx 0.463$	0.164 ± 0.051	$10.664/8 \approx 1.333$	0.130 ± 0.052
$10k < I < 20k$	$8.923/8 \approx 1.115$	0.205 ± 0.046	$31.697/8 \approx 3.962$	0.213 ± 0.047
$20k < I < 30k$	$15.136/8 \approx 1.892$	0.213 ± 0.055	$9.227/8 \approx 1.153$	0.250 ± 0.052
$30k < I < 40k$	$2.706/8 \approx 0.338$	0.236 ± 0.070	$7.365/8 \approx 0.921$	0.227 ± 0.070
$40k < I < 50k$	$9.259/8 \approx 1.158$	0.145 ± 0.097	$9.321/8 \approx 1.165$	0.201 ± 0.092
$50k < I < 60k$	$9.735/8 \approx 1.217$	0.259 ± 0.160	$9.784/8 \approx 1.223$	0.280 ± 0.153
	I Corrected		I+Beam Corrected	
Intensity	$\chi^2/n.d.f$	ν	$\chi^2/n.d.f.$	ν
$I < 10k$	$3.547/8 \approx 0.443$	0.159 ± 0.051	$8.792/8 \approx 1.099$	0.132 ± 0.052
$10k < I < 20k$	$11.537/8 \approx 1.442$	0.206 ± 0.047	$34.767/8 \approx 4.346$	0.213 ± 0.047
$20k < I < 30k$	$14.365/8 \approx 1.796$	0.227 ± 0.054	$9.241/8 \approx 1.155$	0.265 ± 0.052
$30k < I < 40k$	$2.178/8 \approx 0.272$	0.254 ± 0.071	$6.697/8 \approx 0.837$	0.234 ± 0.071
$40k < I < 50k$	$7.444/8 \approx 0.930$	0.188 ± 0.097	$8.554/8 \approx 1.069$	0.252 ± 0.093
$50k < I < 60k$	$9.205/8 \approx 1.151$	0.225 ± 0.156	$9.540/8 \approx 1.193$	0.253 ± 0.149

Table 4.6: **One Dimensional Intensity Dependent Extractions of Azimuthal Moments from Collected p+D Data.** Previous extracted values for proton induced Drell-Yan are nonzero ($\nu = 0.027 \pm 0.01$) at different momentum fractions and mean q^2 [1]. Extractions for E906/SeaQuest are shown here. Extracted values are halfway between pion induced values from CERN-NA10 and E866/NuSea. Extractions also show slight intensity dependence, especially at the lower intensity bins, which remain even after the parameterized intensity correction. Plots of all extractions are shown in Figure 4.5.

Azimuthal extractions from the entire Deuterium sample integrated over inten-

$[\kappa] + [\nu\kappa] \cos 2\phi$ Extractions				
Sample Class	$\chi^2/n.d.f$	ν	$[\kappa]$	$[\nu\kappa]$
Standard	$14.355/8 \approx 1.794$	0.194 ± 0.030	417.0 ± 8.24	80.8 ± 12.4
I	$11.494/8 \approx 1.437$	0.203 ± 0.030	639.0 ± 12.7	130.0 ± 19.0
Beam	$29.649/8 \approx 3.706$	0.195 ± 0.029	417.0 ± 8.08	81.5 ± 12.0
I+Beam	$27.889/8 \approx 3.486$	0.204 ± 0.029	637.0 ± 12.4	130.0 ± 18.4
Background	$6.4192/8 \approx 0.802$	0.286 ± 0.103	38.5 ± 2.57	11.0 ± 3.89

Table 4.7: **One Dimensional Extractions of Azimuthal Moments from Collected p+D Data.** Previous extracted values for proton induced Drell-Yan are nonzero ($\nu = 0.027 \pm 0.01$) at different momentum fractions and mean q^2 [1]. Extractions for E906/SeaQuest are shown here. Integrated values with various corrections are all within one standard deviation of each other and azimuthal fits get worse with the introduction of the beam acceptance shift. Plots of each extraction are shown in Figure 4.6.

sity are shown in Figure 4.6 and Table 4.7. All extractions with different acceptance configurations, agree with each other, however the goodness-of-fit of extractions from beam shifted examples are worse than extractions with standard acceptance treatments. For the final value, the "I+Beam" sample is chosen and compared to the background sample (shown at the bototm of Figure 4.6) using a adaptation of equation 4.1:

$$\nu^{DY} = \frac{\nu^{Sa} - r\nu^{Bg}}{1 - r}, \tag{4.2}$$

where ν^{Sa} is the extracted azimuthal moment for the entire sample, r is the background percentage, and ν^{Bg} is the magnitude of azimuthal moment in the background. The azimuthal moment of background was obtained by first applying the "I+Beam" sample treatments to the EMPTY and NO TARGET combined sample after all cuts and acceptance corrections, then applying the same one dimensional fit that was used to extract from the signal sample. Using the same background concentration (39.3%) as was used for the extraction of the final polar moment, the calculated value is $\nu^{DY} = .151$.

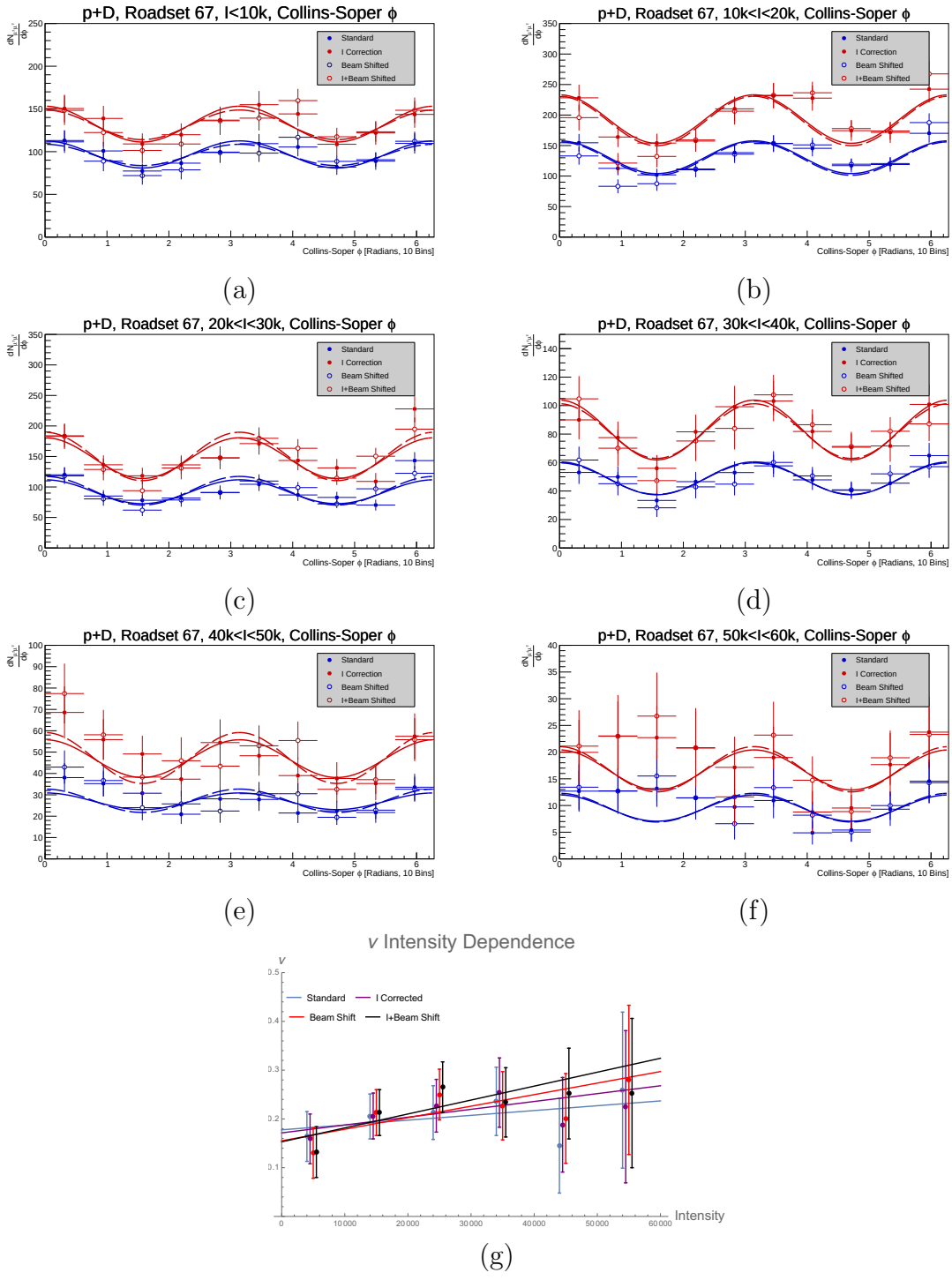

Figure 4.5: **One Dimensional Intensity Dependent Extractions of Azimuthal Moments from Collected p+D Data.** Previous extracted values for proton induced Drell-Yan are nonzero ($\nu = 0.027 \pm 0.01$) at different momentum fractions and mean q^2 [1]. Extractions are arranged alphabetically from lowest intensity to highest intensity. Fits were over a polar range of $|\cos\theta| < .589$ in order to minimize acceptance effects. Graph (g) shows explicitly how ν varies with intensity. Goodness of fit and extracted azimuthal values are shown in Table 4.6.

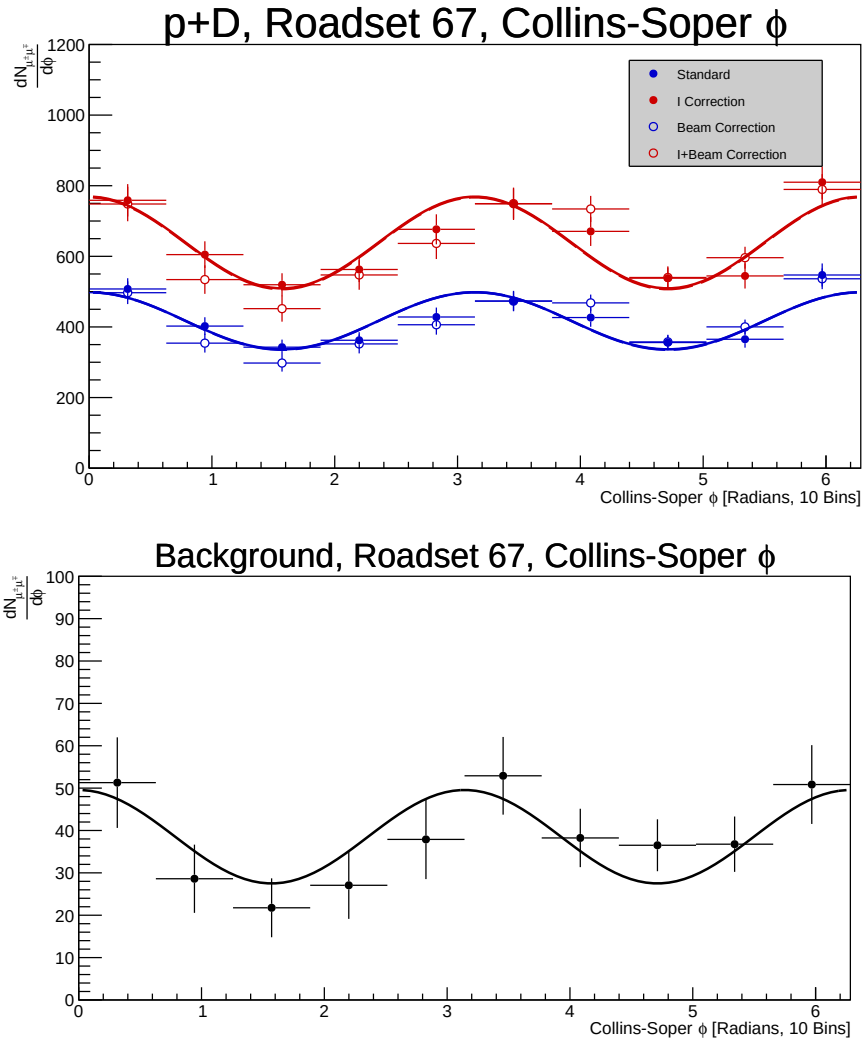

Figure 4.6: **One Dimensional Extraction of Azimuthal Moments from Collected p+D Data.** Previous extracted values for proton induced Drell-Yan are nonzero ($\nu = 0.027 \pm 0.01$) at different momentum fractions and mean q^2 [1]. Extractions for E906/SeaQuest are shown here. The top graph shows extractions of the azimuthal moment from collected Deuterium data with various corrections. The bottom graph shows extractions from a background sample with a "I+Beam" treatment. Goodness of fit and extracted azimuthal values are shown in Table 4.7.

4.3.3 Estimation of Statistical and Systematic Errors

Using equations 4.1 and 4.2 the error propagation calculation for both angular moments is:

$$\sigma_{x^{DY}} = x^{DY}\sqrt{\frac{(1-r)^2\left[(rx^{Bg})^2[(\frac{\sigma_r}{r})^2+(\frac{\sigma_{x^{Bg}}}{x^{Bg}})^2]+\sigma^2_{x^{Sa}}\right]+\sigma_r^2(x^{Sa}-rx^{Bg})}{(x^{Sa}-rx^{Bg})^2(1-r)^2}}, \quad (4.3)$$

where x is the angular magnitude parameter (λ or ν) and σ_x is the uncertainty of x. Statistical error can be calculated using the values from Tables 4.5 and 4.7. The relative statistical error on the sample calculation and background sample is 9% and 3.6%, respectively. Using these values the statistical error is calculated as $\sigma^{(stat.)}_{\lambda^{DY}} = 1.19$ and $\sigma^{(stat.)}_{\nu^{DY}} = 0.088$.

For a complete result, Equation 4.3 must also be evaluated as a function of systematic error for each angular moment, however the systematic error for each value in the equation must be discussed. The systematic error on the background concentration (σ_r) can be estimated by comparing the results of the mass spectrum fit for this analysis to those of E906/SeaQuest collaborators Jason Dove and Kenichi Nakano, which differ from this analysis by about 30% [105, 106]. Systematic errors on extracted polar moments start with an estimation of the systematic uncertainty on the extraction method for a particular extracted azimuthal moment as shown in Table 3.3. A thrown azimuthal moment of $\nu = .151$ was never tested however, it is the midway point between $\nu = .10$ and $\nu = .20$. An average of the difference from the expected value yields a method uncertainty of $\sigma^{syst.(ext.)}_{\lambda^{Sa}} = 0.445$ for polar moments and, using the same method for extractions of the azimuthal moment, $\sigma^{syst.(ext.)}_{\nu^{Sa}} = 0.01$.

Uncertainty due to intensity dependence can be estimated using the highest and lowest extraction values for the extracted moment. For the polar moment, this value can be read off from Table 4.4 and is $\sigma^{syst.(int)}_{\lambda^{Sa}} = 3.68$ while for the azimuthal moment,

the same technique using Table 4.6 yields an uncertainty of $\sigma_{\nu^{Sa}}^{syst.(int)} = 0.133$. An estimation of the systematic uncertainty due to the beam shift can be tested by comparing beam shifted data to standard data, which approximates a beam shift. For the polar moment, the average difference between extracted moments can be read off from Table 4.5 as $\sigma_{\lambda^{Sa}}^{syst.(shift)} = 0.326$ and the azimuthal uncertainty due to the beam shift as shown in Table 4.7 is $\sigma_{\nu^{Sa}}^{syst.(shift)} = 0.001$. Finally, the largest systematic uncertainty is probably the effect of the trigger, which can not be effectively estimated at this point. If the uncertainty due the trigger is assumed to be 100% of any measurement, a value can be calculated which depends on a redefinition of trigger dependence at a later date.

A combined systematic uncertainty for either angular moment can be calculated using a simple quadrature sum of the previous identified values:

$$\sigma_{x^{Sa}}^{syst.} = \sqrt{\sigma_{x^{Sa}}^{syst.(ext.)} + \sigma_{x^{Sa}}^{syst.(int.)} + \sigma_{x^{Sa}}^{syst.(shift.)}}, \tag{4.4}$$

where the uncertainty due to the trigger has been excluded. For the polar moment, this equation yields a value of $\sigma_{\lambda^{Sa}}^{syst.} = 3.72$ which when used in equation 4.3 for both the sample and background extraction uncertainty values is $\sigma_{\lambda^{DY}}^{syst} = 6.52$. When the same method is used for the azimuthal moment, equation 4.4 gives $\sigma_{\nu^{Sa}}^{syst.} = 0.133$ and equation 4.3 gives $\sigma_{\nu^{DY}}^{syst.} = 0.346$.

4.3.4 Transverse Momentum Distributions

Distributions of Drell-Yan transverse momentum gives some information about the nonperturbative versus perturbative origin of observed dynamics, and are thus valuable to examine within the context of angular moment extractions with the goal of probing nonperturbative spin-momentum correlations in the nucleon. Transverse momentum of the dimuon pair at low p_T is directly affected by the initial transverse

momentum of the quark pair and should transition from a Gaussian approximation to a power law relationship described by pQCD. In terms of TMDs, the E906/SeaQuest experiment is in a unique region to measure the transition from a TMD framework with constraint, $Q_T \ll Q$ to a Twist-3 Collinear PDF framework, which has similar terms but applies at $Q_T \sim Q$.

The mean transverse momentum of the intensity and beam corrected sample is 0.87 ± 0.50 GeV/c. For background this mean shifts upwards to 1.02 ± 0.65 GeV/c. These values should be compared to the mean mass of the sample which is 5.48 ± 0.70 GeV. The transverse momentum shape of the collected sample is shown in Figure 4.7.

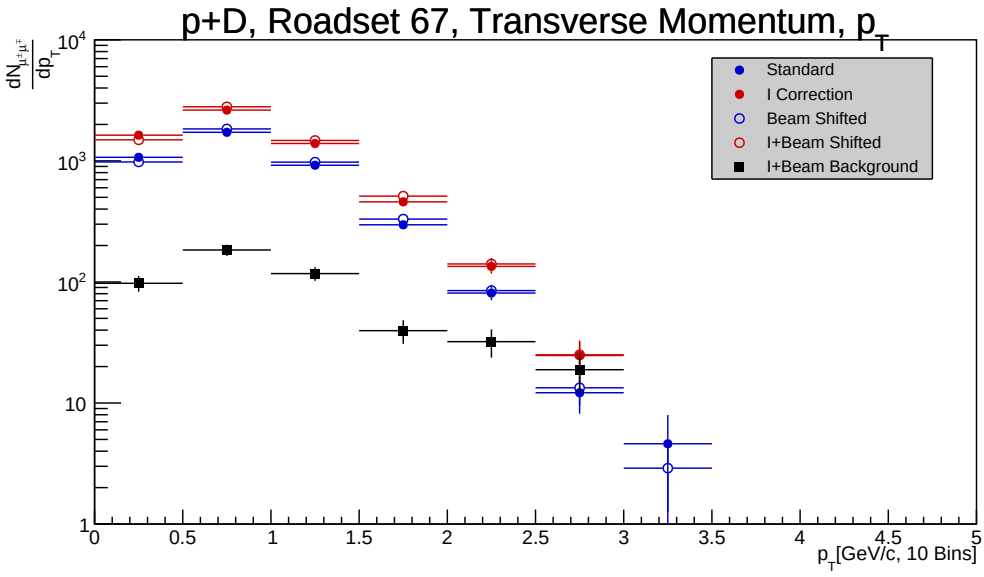

Figure 4.7: **One Dimensional Transvserse Momentum Distributions.** All transverse momentum distributions with various sample configurations are shown along with background. The background distribution has been scaled by a factor of 1.25 in order to counteract the difference in protons on target as a function of the target rotation cycle.

CHAPTER V

Discussion & Conclusion

5.1 Discussion

The extractions presented in the previous section, $\lambda = -1.13 \pm 1.19(stat.) \pm 6.52(syst.)$ and $\nu = 0.151 \pm 0.088(stat.) \pm 0.346(syst.)$ are within the expected physical range of extractions using only statistical errors, but for the polar moment, the systematic uncertainty is larger than the physical range of the parameter. For the azimuthal moment, the systematic uncertainty is on the order of the difference between pion induced and proton induced Drell-Yan observations conducted by previous experiments. These facts, along with the large dependence on collected intensity, indicate that at the very least, not all corrections have been properly calculated or applied with regard to intensity, and also suggests that accurate background estimation is absolutely necessary for proper extraction. Furthermore, it appears that accurate estimation of background is intimately linked to the quality of understanding concerning spectrometer response to different intensities. This thesis shows that as a whole, the identification of single muons as a function of intensity is not well understood and that this lack of understanding makes proper calculation of the background sample difficult for non-ratio analyses. As a result, instead of discussing the broader implications of extractions from Drell-Yan produced from proton on Deuterium interactions, a discussion of the mutiple points of failure is more appropriate.

5.1.1 Suggested Trigger Efficiency Correction

It is unclear whether the MATRIX/FPGA1 physics trigger has any remaining intensity dependent bias or not, as not enough NIM3 minimum bias data exist to select events which would have fired the physics trigger. Given the number of events which pass a physics trigger emulation, approximately 10^3 times more minimum bias data would be needed to generate a reliable direct comparison. Unfortunately, E906/SeaQuest concluded its first phase in June of 2017 and with the advent of E1039/SeaQuest, will switch from an unpolarized to polarized target configuration, significantly changing the observed cross sections. During all of phase one, E906/SeaQuest collected less than ten times the amount of data in Roadset 67, putting a direct removal of intensity dependence at the physics trigger as a function of observable out of reach for non-ratio analyses.

In lieu of a direct comparison, intensity dependence can be measured using observables in the MATRIX/FPGA4 single muon trigger with pair match emulation for comparison with the physics trigger. This path seems promising, as comparisons of the single muon trigger at different intensity levels in Figure 3.16 show that wherever acceptance is large, collected muons are accepted and reconstructed at equivalent rates regardless of intensity. Given that no intensity dependence is observed in the single muon trigger, the next step of the analysis would be to compare with the NIM3 trigger to ensure that emulated events could be reasonably reconstructed at equivalent rates. If the single muon trigger showed any bias with respect to the minimum bias trigger, an intensity dependent weighting could be devised and applied at the single muon level before kTracker pairing.

If a single muon weighting is required the quality of the comparison depends on the number of events collected with the minimum bias trigger, however not all data was collected over the same roadset or even with the same overall acceptance. Acceptance changes should be manageable, but a change in roadsets may contribute to a road

dependent selection bias based on detector dead time. In addition to acceptance, overall spectrometer alignment, which changed many times due to adjustments and repairs of various stations, would need to be partitioned and compared to each other in order to get as large a minimum bias data set as reasonably possible. Barring an exhaustive comparison at the muon trajectory observable level, weightings could be applied at the hodoscope hit level and an overall intensity dependent hit normalization scheme would need to be developed.

5.1.2 Suggested Event Reconstruction Efficiency Correction

The process of verifying the trigger as a function of observable makes some implicit assumptions about the linearity of kTracker response to changes in intensity which need verification, but the method of verification depends on the relative dependence of the minimum bias and physics trigger on intensity. If a trigger correction is needed, whatever weighting scheme is developed will need to be implemented at the track reconstruction level. Rather than normalizing two correlated weighting schemes it would be simpler to develop a combined trigger-tracker scheme. Regardless of the status of the trigger, the following should be implemented either as a stand alone scheme or as part of a trigger-tracker correction.

At the hardware level, chamber efficiency at low load is a good start but chamber efficiency as a function of intensity is really dependent on chamber occupancy, which is correlated with but not directly related to intensity. A good place to start in understanding this relationship as a function of single muon or dimuon observable is a beam intensity scan, which would parameterize how the efficacy of chamber signals varied as a function of intensity or occupancy and correlate how intensity and occupancy varied with respect to each other. From there muon reconstruction efficiency would be a function of the track reconstruction software and its ability to reliably differentiate real single muons from noise. A measure of this is already shown

in Figure 3.19 as an evaluation of minimum bias data embedded in simulation but it contains a number of assumptions not least of which being that the FPGA and NIM type triggers behave similarly. Furthermore, it is unclear how muon trajectory reconstruction varies as a function of occupancy and it does not take into account the possibility of efficiency changes due to local hit density which would emerge as a second order (and likely negligible) effect.

One independent way of estimating event reconstruction efficiency would be to utilize a modified version of the "event efficiency" idea, first proposed by Takahiro Sawada, a post doctoral researcher at the University of Michigan. This idea would use embedded spectrometer based simulation at the hit level to estimate the local noise tolerance of event reconstruction at the angular position and transverse momentum defined by a particular event. The result of the exercise would be a parameterization which described the probability of reconstructing a particular event as a function of its angular position, transverse momentum, intensity, and occupancy. An added benefit would be the simultaneous calculation of the global and local occupancy tolerance of the track reconstruction software as a function of desired physics observable.

5.1.3 Suggested Background Considerations

The presence of background is likely one of the biggest sources of uncertainty in the extraction but proper substraction of background from angular and transverse momentum distributions is very challenging. In a non-ratio analyses, an ideal calculation of background would involve the use of simulation to observe how known physics processes, like meson production and decay, varied as a function of luminosity. To first order, this information would provide either a background shape or production rate relative to real target Drell-Yan which could then be implemented in a mass spectrum fit. From there, background would be reliably subtracted from all observable distributions simultaneously.

In order to proceed with the course of action outlined above the current collaboration simulation software would need to be heavily modified for a considerable speed up or assumptions about target-dump separation could be utilized to examine sources of single muons generated in the target, however collected muons from the dump with all analysis cuts would need to be negligible and the existence of NO TARGET and EMPTY data after all analysis cuts shows that they are not. The inclusion of more experiment data may allow for harsher cuts which would eliminate NO TARGET and EMPTY data supporting the idea of high sample purity but would sacrifice a significant numbers of events. As it stands now, the use of EMPTY and NO TARGET events to estimate background shape could over represent contributions from certain sources of background indentified in Table 4.3 but the mixed event background calculated from accepted dimuon samples gives no information about sample purity and uses events which are not statistically independent from the fit model to estimate sample purity.

In lieu of a viable simulation or model, the method for constraining angular contributions from the background used in equations 4.1 and 4.2 presents a good estimation, but it is ultimately decided by the quality of the angular extraction technique. One strategy for this method is to constrain the sample until almost no background is present ($r \rightarrow 0$), reducing angular contributions from background to a negligible amount. Another involves a fitting strategy using a binned or unbinned maximum likelihood fit which could be applied to simulation of differing modulations to estimate the systematic uncertainty ($\sigma_r, \sigma_{x^{DY}}, \sigma_{x^{Bg}} \rightarrow 0$) and then applied to NO TARGET with standard sample cuts. It is likely that a combination of both methods outlined above will be used in the near future.

5.2 Summary & Conclusion

Since its inception, Quantum Chromodynamics (QCD) (and by extension pQCD) has had considerable success in describing the strong sector of the Standard Model, but particular details of nucleon structure remain a mystery. The Drell-Yan process is a versatile probe of nucleon structure, providing information about flavor structure by comparison over various nuclear species as well as hints about parton dynamics by examination of the angular distributions. Historical analysis of Drell-Yan angular distributions as the kinematical treatment of a "two-to-two", s-channel process concerns the parameterizations of angular moments by λ, μ, and ν, linear combinations of virtual photon structure functions assumed to describe strong currents in quark-quark annihilation. Since quarks are fermions, the Lam-Tung relation links virtual photon polarization to the possibility of angular momentum transfers in higher order collinear processes (like gluon radiation and readsorption), however violations of the Lam-Tung relation in previous experiments at Fermilab and CERN suggest this interpretation is incorrect. One possible explanation for the Lam-Tung violation is the existence of Transverse Momentum Dependent distributions which use a Twist-2 transverse momentum dependent analysis to infer the existence of spin-orbit and spin-spin coupling between nucleons and their constituent quarks. One TMD in particular, the Boer-Mulders distribution, describes the spin-orbit correlation between an unpolarized nucleon and a polarized quark. A convolution of two Boer-Mulders TMDs (one contribution from the quark and one from the anti-quark) is parameterized in Drell-Yan angular cross sections exactly like the ν parameter, and the existence of the TMD would appear as a violation of the Lam-Tung relation.

Continuing in the long tradition of Drell-Yan experiments at Fermilab, the E906/SeaQuest collaboration used 120 GeV proton beams from the MI to examine the angular distributions of dimuons induced in interactions with Deuterium. Time

dependent differences in proton beam intensity from the MI led to time dependence in spectrometer response which was dealt with as an intensity dependence in the physics trigger and muon trajectory reconstruction software. The first level of the physics trigger was verified to have little intensity dependence, however the comparison of the first level of the physics trigger to diagnostic triggers suggests that either the physics trigger or diagnostics trigger may have uncorrected intensity dependence. An analysis method was developed which depends on the difference in efficiency between the physics and diagnostics triggers and applied to collected data, which also was curated specifically to reduce background.

Extracted Drell-Yan angular moments of $\lambda = -1.13 \pm 1.19(stat.) \pm 6.52(syst.)$ and $\nu = 0.151 \pm 0.088(stat.) \pm 0.346(syst.)$ were consistent with the physical range of acceptable measurements but systematic uncertainties preclude any definitive statements concerning parton dynamics as currently observed by E906/SeaQuest. It is expected that a proper correction of background, a verification of trigger efficiency, and an intensity dependent correction that focuses on occupancy would improve the efficacy of these values.

BIBLIOGRAPHY

BIBLIOGRAPHY

[1] L.Y. Zhu and J.C. Peng et. al. Measurement of Angular Distributions of Drell-Yan Dimuons in p+p Interactions at 800 GeV/c. *Physical Review Letters*, 102:182001, 2009.

[2] Eugen Merzbacher. *Quantum Mechanics*. John Wiley & Sons, United States of America, 3rd edition, 1991.

[3] John David Jackson. *Classical Electrodynamics*. Wiley, New York, 3rd edition, 1998.

[4] L.D. Landau and E. M. Lifshitz. *Statistical Physics*. Pergamon Press, Maxwell House, Fairview Park, Elmsford, New York 10523, U.S.A., 3rd edition, 1980.

[5] Wolfgang Pauli. The Connection Between Spin and Statistics. *Physical Review*, 58:716, 1940.

[6] Natalie Wolchover. What no new particles means for physics. https://www.quantamagazine.org/what-no-new-particles-means-for-physics-20160809/. Accessed: 2017-12-01.

[7] Sheldon Glashow. Partial-Symmetries of Weak Interactions. *Nuclear Physics*, 22:579, 1961.

[8] Steven Weinberg. A Model of Leptons. *Physical Review Letters*, 21:1264, 1967.

[9] A. Salam and J. C. Ward. Electromagnetic and Weak Interactions. *Physics Letters*, 13:168, 1964.

[10] Julia Woithe et. al. Let's have a coffee with the Standard Model of particle physics! *Physics Education*, 52:034001, 2017.

[11] Emmy Noether. Invariant Variation Problems. *arXiv:physics/0503066v2*, 2015.

[12] Mark Srednicki. *Quantum Field Theory*. Cambridge University Press, Cambridge, UK, 1st edition, 2007.

[13] Michael Peskin and Daniel Schroeder. *An Introduction to Quantum Field Theory*. Perseus Book Publishing, 1st edition, 1995.

[14] Murray Gell-Mann. Symmetries of Baryons and Mesons. *Physical Review*, 125:1067, 1962.

[15] Mark Thomson. Particle physics, handout 8: Quantum chromodynamics. http://www.hep.phy.cam.ac.uk/ thomson/partIIIparticles/handouts/Handout_8_2011.pdf. Accessed: 2017-12-01.

[16] Murray Gell-Mann. A Schematic Model of Baryons and Mesons. *Physical Letters*, 8:3, 1964.

[17] LHCb Collaboration. Observation of the Resonant Character of the Z(4430)$^-$ State. *Physical Review Letters*, 112:222002, 2014.

[18] LHCb Collaboration. Observation of J/ψp Resonances Consistent with Pentaquark States in $\Lambda_b^0 \to J/\psi K^- p$ Decays. *Physical Review Letters*, 115:072001, 2015.

[19] LHCb Collaboration. Observation of J/$\psi\phi$ Structures Consistent with Exotic States from Amplitude Analysis of B$^+$ $\to$J/$\psi\phi K^+$ Decays. *Physical Review Letters*, 118:022003, 2017.

[20] Francis Halzen and Alan D. Martin. *Quarks and Leptons: An Introductory Course in Modern Particle Physics*. Wiley, New York, 1st edition, 1984.

[21] Alexandre Deur et. al. The QCD running coupling. *Progress in Particle and Nuclear Physics*, 90:1, 2016.

[22] Richard E. Taylor. Deep inelastic scattering: The early years. *Reviews of Modern Physics*, 63:573, 1991.

[23] Henry W. Kendall. Deep inelastic scattering: Experiments on the proton and the observation of scaling. *Reviews of Modern Physics*, 63:597, 1991.

[24] Jerome Friedman. Deep inelastic scattering: Comparisons with the quark model. *Reviews of Modern Physics*, 63:615, 1991.

[25] E. M. Lyman et. al. Scattering of 15.7-Mev Electrons by Nuclei. *Physical Review*, 84:626, 1951.

[26] A.O. Hanson et. al. Measurement of Multiple Scattering of 15.7-Mev Electrons. *Physical Review*, 84:634, 1951.

[27] G.P.S. Occhialini and C.F. Powell. Nuclear Disintegrations Produced by Slow Charged Particles of Small Mass. *Nature*, 159:186, 1947.

[28] G. D. Rochester and Butler C. C. Evidence for the existence of new unstable elementary particles. *Nature*, 160:855, 1947.

[29] R. Bjorklund et. al. High Energy Photons from Proton-Nucleon Collisions. *Physical Review*, 77:213, 1950.

[30] G. Danby et. al. Observation of High-Energy Neutrino Reactions and the Existence of Two Kinds of Neutrinos. *Physical Review Letters*, 9:36, 1962.

[31] Piet Mulders and R. D. Tangerman. Über den Bau der Atomkerne. I. *Physik*, 77:1, 1932.

[32] George Zweig. An SU(3) Model for Strong Interaction Symmetry and Its Breaking. *(unpublished) CERN LIBRARIES: CERN-TH-401*, 1964.

[33] Richard Feynman. The Behavior of Hadron Collisions at Extreme Energies. In M.E. Noz and Kim Y. S., editors, *Special Relativity and Quantum Theory*, page 289, 1969.

[34] Jerome Breidenbach et. al. Observed Behavior of Highly Inelastic Electron-Proton Scattering. *Physical Review Letters*, 23:935, 1969.

[35] E. D. Bloom et. al. High-Energy Inelastic e-p Scattering at 6° and 10°. *Physical Review Letters*, 23:930, 1969.

[36] B. J. Bjorken and E. A. Paschos. Inelastic Electron-Proton and γ-Proton Scattering and the Structure of the Nucleon. *Physical Review*, 185:1975, 1969.

[37] J.D. Bjorken. Asymptotic Sum Rules at Infinite Momentum. *Physical Review*, 179:1547, 1969.

[38] B.J. Bjorken and Glashow S. L. Elementary Particles and SU(4). *Physics Letters*, 11:253, 1964.

[39] David J. Gross and Frank Wilczek. Ultraviolet Behavior of Non-Abelian Gauge Theories. *Physical Review Letters*, 30:1343, 1973.

[40] H. David Politzer. Reliable Perturbative Results for Strong Interactions? *Physical Review Letters*, 30:1346, 1973.

[41] J. Collins. *Foundations of Perturbative QCD*, volume 1st. Cambridge University Press, 2011.

[42] Siegfried Bethke et. al. World Summary of α_s (2015). In *EPJ Web of Conferences*, volume 120, page 07005, 2016.

[43] David d'Enterria. α_s review (2016). *arXiv:1606.04772v2*, 2016.

[44] Robert Craig Group. Theses: Measurement of the inclusive jet cross section using the midpoint algorithm in run ii at the collider detector at fermilab (cdf), 2006.

[45] H1 and ZEUS Collaborations. Combination of measurements of inclusive deep inelastic $e^{\pm}p$ scattering cross sections and QCD analysis of HERA data. *The European Physical Journal C*, 75:580, 2015.

[46] K. L. Giboni et. al. Diffractive Production of the Charmed Baryon λ_c^+ at the CERN ISR. *Physics Letters B*, 85:437, 1979.

[47] S. J. Brodsky et. al. The Intrinsic Charm of the Proton. *Physics Letters B*, 93:451, 1980.

[48] S. J. Brodsky et. al. Intrinsic heavy-quark states. *Physical Review D*, 23:2745, 1981.

[49] Jen-Chieh Peng et. al. Flavor Structure of Intrinsic Nucleon Sea. *Few Body Systems*, 56:349, 2015.

[50] Kurt Gottfried. Sum Rule for High-Energy Electron-Proton Scattering. *Physical Review Letters*, 18:1174, 1967.

[51] A. L. Kataev. The Gottfried sum rule : theory vs experiment. *arXiv:hep-ph/0311091v1*, 2003.

[52] et. al. S. Stein. Electron scattering at 4° with energies of 4.5-20 GeV. *Physical Review D*, 12:1884, 1975.

[53] European Muon Collaboration. Measurements of the Nucleon Structure Functions F_2^N in Deep Inelastic Muon Scattering from Deuterium and Comparison with those from Hydrogen and Iron . *Nuclear Physics B*, 293:740, 1987.

[54] BCDMS Collaboration. A High Statistics Measurement of the Deuteron Structure Functions $F_2(x, Q^2)$ and R from Deep Inelastic Muon Scattering at High Q^2. *Physics Letters B*, 237:599, 1990.

[55] BCDMS Collaboration. A Comparison of the Structure Functions F_2 of the Proton and the Neutron from Deep Inelastic Muon Scattering at High Q^2. *Physics Letters B*, 237:599, 1990.

[56] New Muon Collaboration. Gottfried Sum from the Ratio F_2^n/F_2^p. *Physical Review Letters*, 66:2712, 1991.

[57] New Muon Collaboration. Reevaluation of the Gottfried sum. *Physics Review D*, 50:R1, 1994.

[58] J. G. Heinrich et. al. Measurement of the Ratio of Sea to Valence Quarks in the Nucleon. *Physical Review Letters*, 63:356, 1989.

[59] Sidney D. Drell and Tung-Mow Yan. Massive Lepton-Pair Production in Hadron-Hadron Collisions at High Energies. *Physical Review Letters*, 25:316, 1970.

[60] J. H. Christenson et. al. Observation of Massive Muon Pairs in Hadron Collisions. *Physical Review Letters*, 25:1523, 1970.

[61] NA51 Collaboration. Study of the isospin symmetry breaking in the light quark sea of the nucleon from the Drell-Yan process. *Physics Letters B*, 332:244, 1994.

[62] P. L. McGaughey et. al. Limit on the $\bar{d}/\bar{u}$ Asymmetry of the Nucleon Sea from Drell-Yan Production. *Physical Review Letters*, 69:1726, 1992.

[63] S. D. Ellis and W. J. Stirling. Constraints on isospin breaking in the light quark sea from the Drell-Yan process. *Physics Letters B*, 256:258, 1991.

[64] Estia J. Eichten et. al. Flavor asymmetry in the light-quark sea of the nucleon. *Physical Review D*, 45:2269, 1992.

[65] S. Kumano and J. T. Londergan. Origin of SU(2)-flavor-symmetry breaking in antiquark distribution. *Physical Review D*, 44:717, 1991.

[66] E866 Collaboration. Measurement of the Light Antiquark Flavor Asymmetry in the Nucleon Sea. *Physical Review Letters*, 80:3715, 1998.

[67] E866 Collaboration. Improved measurement of the $\bar{d}/\bar{u}$ asymmetry in the nucleon sea. *Physical Review D*, 64:052002, 2001.

[68] R. D. Field and Feynman R. D. Quark elastic scattering as a source of high-transverse-momentum mesons. *Physical Review D*, 15:2590, 1977.

[69] F. M. Steffens and Thomas A. W. Flavor asymmetry of the nucleon sea. *Physical Review C*, 55:900, 1997.

[70] S. Kumano. Flavor asymmetry of antiquark distributions in the nucleon. *Physics Reports*, 303:183, 1998.

[71] J. D. Sullivan. One-Pion Exchange and Deep-Inelastic Electron Nucleon Scattering. *Physical Review D*, 5:1732, 1972.

[72] T. P. Cheng and Ling-Fong Li. Flavor and Spin Contents of the Nucleon in the Quark Model with Chiral Symmetry. *Physical Review Letters*, 74:2872, 1995.

[73] S. W. Herb et. al. Observation of Dimuon Resonance at 9.5 GeV in 400-GeV Proton Nucleus Collisions. *Physical Review Letters*, 39:252, 1977.

[74] et. al. K. Nakamura (Particle Data Group). $J/\psi(1S)$. *Journal of Physics G*, 37:075021, 2010.

[75] et. al. K. A Olive (Particle Data Group). $\psi'(2S)$. *Chinese Physics C*, 38:090001, 2014.

[76] J. C. Webb et. al. Absolute Drell-Yan Dimuon Cross Sections in 800 GeV/c p+p and p+d Collisions. *unpublished*, 2003.

[77] C. S. Lam and Wu-Ki Tung. Systematic approach to inclusive lepton pair production in hadronic collisions. *Physical Review D*, 18:2447, 1978.

[78] C. G. Callan and David J. Gross. High-Energy Electroproduction and the Constitution of the Electric Current. *Physical Review Letters*, 22:156, 1969.

[79] C. S. Lam and Wu-Ki Tung. Parton-model relation without quantum chromodynamic modifications in lepton pair production. *Physical Review D*, 21:2712, 1980.

[80] NA10 Collaboration. Angular Distributions of Muon Pairs Produced by 194 GeV/c Negative Pions. *Zeitschrift für Physik C*, 31:513, 1986.

[81] NA10 Collaboration. Angular distributions of muon pairs produced by negative pions on deuterium and tungsten. *Zeitschrift für Physik C*, 37:545, 1988.

[82] E615 Collaboration. Experimental study of muon pairs produced by 252-GeV pions on tungsten. *Physical Review D*, 39:92, 1989.

[83] L.Y. Zhu and J.C. Peng et. al. Measurement of Angular Distributions of Drell-Yan Dimuons in p+d Interactions at 800 GeV/c. *Physical Review Letters*, 99:082301, 2007.

[84] Jen-Chieh Peng et. al. Interpretation of angular distributions of Z-boson production at colliders. *Physical Letters B*, 758:384, 2016.

[85] Stanley J. Brodsky et. al. Quantum chromodynamics and other field theories on the light cone. *Physics Reports*, 301:299, 1998.

[86] Dennis Sivers. Single-spin production asymmetries from the hard scattering of pointlike constituents. *Physical Review D*, 41:83, 1990.

[87] John Collins. Fragmentation of transversely polarized quarks probed in transverse momentum distributions. *Nuclear Physics B*, 396:161, 1993.

[88] Daniel Boer and Piet Mulders. Time-reversal odd distribution functions in leptoproduction. *Physical Review D*, 57:5780, 1998.

[89] Alesandro Bacchetta et. al. Single-spin asymmetries: The Trento conventions. *Physical Review D*, 70:117504, 2004.

[90] P.J. Mulders and R.D. Tangerman. The complete tree-level result up to order 1/Q for polarized deep-inelastic leptoproduction. *Nuclear Physics B*, 461:197, 1996.

[91] Piet Mulders and R. D. Tangerman. The complete tree-level result up to order $1/Q$ for polarized deep-inelastic leptoproduction [Nucl. Phys. B 461 (1996) 197]. *Nuclear Physics B*, 484:Erratum, 538, 1997.

[92] C. J. Bomhof et. al. Gauge link structure in quark-quark correlators in hard processes. *Physics Letters B*, 596:277, 2004.

[93] K. Goeke et. al. Parameterization of the quark-quark correlator of a spin-$\frac{1}{2}$ hadron. *Physics Letters B*, 618:90, 2005.

[94] Daniel Boer. Investigating the origins of transverse spin asymmetries at BNL RHIC. *Physical Review D*, 60:014012, 1999.

[95] European Muon Collaboration. Measurement of the Deuteron Structure Function F_2^d and a Comparison of Proton and Neutron Structure . *Physics Letters B*, 123:123, 1983.

[96] E605 Collaboration. $\pi/K/p$ Identification with a Large-Aperture Ring-Imaging Cherenkov Counter . *Nuclear Instruments and Methods*, 217:237, 1983.

[97] Yorikiyo Nagashima. *Elementary Particle Physics*. Wiley-VCH, WILEY-VCH Verlag GmbH & Co. KGaA Boschstr. 12, 69469 Weinheim, Germany, 1st edition, 2013.

[98] Roy J. Holt and Craig D. Roberts. Distribution Functions of the Nucleon and Pion in the Valence Region. *Reviews of Modern Physics*, 82:2991, 2010.

[99] R. E. Kalman. A New Approach to Linear Filtering and Predictive Problems. *Journal of Basic Engineering, Series D*, 82:35, 1960.

[100] David Kleinjan. Hodoscope Efficiency Info. *E906/SeaQuest Internal Document ID:2705-v1*, 2017.

[101] Kenichi Nakano. Quick Measurement of Chamber Efficiency. *E906/SeaQuest Internal Document ID:1822-v1*, 2017.

[102] Kenichi Nakano. Status & Plan of dbar/ubar Analysis. *E906/SeaQuest Internal Document ID:2510-v4*, 2017.

[103] PHENIX Collaboration. Double Helicity Asymmetry in Inclusive Midrapidity π^0 Production for Polarized p + p Collisions at $\sqrt{s} = 200$ GeV. *Physical Review Letters*, 93:202002, 2004.

[104] Christine Aidala. Measurement of the Transverse Single-Spin Asymmetry for Mid-rapidity Production of Neutral Pions in Polarized p+p Collisions at 200 GeV Center-of-Mass Energy. *(Unpublished) Thesis*, 2005.

[105] Kenichi Nakano. Update on Comparison between Real Data & Component Sum. *E906/SeaQuest Internal Document ID:2876-v1*, 2017.

[106] Jason Dove. Mass Fitting with FPGA4 Accidentals and Background Estimation. *E906/SeaQuest Internal Document ID:2822-v2*, 2017.